

**EXPERIMENTAL INVESTIGATION OF AIR COOLING SYSTEMS  
FOR ELECTRONIC EQUIPMENT BY USING VORTEX**

**PROMOTERS**

by

**KEVIN D. GOMES**

A thesis submitted to the

**Graduate School-New Brunswick**

**Rutgers, The State University of New Jersey**

in partial fulfillment of the requirements

for the degree of

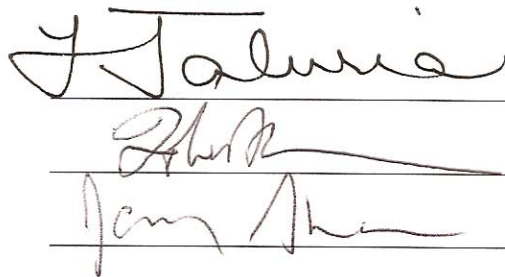
**Master of Science**

**Graduate Program in Mechanical and Aerospace Engineering**

written under the direction of

**Dr. Yogesh Jaluria**

and approved by

Three handwritten signatures are displayed, each on a horizontal line. The top signature is 'Y. Jaluria' in black ink. The middle signature is 'Zhi R' in black ink. The bottom signature is 'Jong Han' in black ink.

**New Brunswick, New Jersey**

**October 2007**

# **ABSTRACT OF THE THESIS**

## **EXPERIMENTAL INVESTIGATION OF AIR COOLING SYSTEMS FOR ELECTRONIC EQUIPMENT BY USING VORTEX PROMOTERS**

**by KEVIN D. GOMES**

**Thesis Director: Dr. Yogesh Jaluria**

Electronic systems these days are getting more powerful and processing speeds are increasing, resulting in increasing heat inputs to the systems. In order to keep up with these speeds, different cooling techniques must be considered. The present study consists of three parts. In the first part, we consider the flow due to a vortex promoter only. The periodic or chaotic behavior in the wake behind the promoter could be beneficial to the heat transfer rate. By analyzing different sizes and shapes, it can determine which vortex promoter offers the best turbulence and at which frequency it occurs. In the second part of the study, the flow over a plate with isolated heat sources only is considered. From here, a base case of just plate flow being perturbed can be achieved. By analyzing the heat transfer rate and the heat transfer coefficient, an understanding on why the larger the separation width between the two heaters, the higher the heat transfer rate can be seen. In the last part of the study, tests are done for the combination of the vortex promoter and the plate. Here, the effects on the heat transfer rate and the heat transfer coefficient are seen by placing a vortex promoter in front of the plate. Comparisons for the same sizes

and shapes used in the first part, along with different heater and plate separations are performed here. From these tests, an optimal promoter is chosen and the distance from the heat sources the promoter has to be, in order to achieve the maximum heat transfer rate and heat transfer coefficient is determined.

## **Acknowledgments**

I would like to express my deepest gratitude to my advisor Dr. Yogesh Jaluria, for his support and guidance throughout my study. His friendly advice, encouragement and experience has helped me a great deal, which allowed me to do some great things while here at Rutgers.

I am also indebted to my friends Joe VanderVeer and Bill Doig for their friendship and support in always trying to help me out and to help me reset my mind after some difficult problems. I would also like to thank Tunc Icoz for his support and guidance in the laboratory and in teaching me on how to use and work the equipment. Thanks to Vasilije Jovanovic for him teaching me on how to work the wind tunnel and all the little things involved with its operation. I would also like to thank John Petrowski for his help in figuring out some new things with the wind tunnel and its wiring. Thanks to Bill Vasiliou for his help and guidance in teaching me about the equipment in the machine shop and for helping me get things done for the labs.

Last but not least, I would like to thank my family for their endless support and encouragement throughout my years here at Rutgers. Without them this would have not been possible.

## **Dedication**

To my family and friends for their everlasting support

## Table of Contents

|   |     |
|---|-----|
| ABSTRACT OF THE THESIS .....                | ii  |
| Acknowledgments.....                        | iv  |
| Dedication .....                            | v   |
| Table of Contents.....                      | vi  |
| List of Tables .....                        | ix  |
| List of Figures .....                       | x   |
| List of Abbreviations .....                 | xiv |
| Chapter 1 .....                             | 1   |
| Literature Survey .....                     | 1   |
| 1 Introduction.....                         | 1   |
| 1.1 Electronic Packaging .....              | 1   |
| 1.2 Cooling Techniques .....                | 4   |
| 1.2.1 Air Cooling .....                     | 5   |
| 1.2.2 Liquid Cooling.....                   | 6   |
| 1.2.2.1 Direct Liquid Cooling.....          | 7   |
| 1.2.2.2 Indirect Liquid Cooling.....        | 8   |
| 1.2.3 Other Cooling Techniques .....        | 9   |
| 1.3 Objective of Study .....                | 10  |
| Chapter 2.....                              | 12  |
| Experimental Setup and Instrumentation..... | 12  |
| 2 Introduction.....                         | 12  |
| 2.1 Wind Tunnel .....                       | 13  |

|                                     |   |    |
|-------------------------------------|---|----|
| 2.1.1                               | Aero Wind Tunnel .....                            | 13 |
| 2.1.2                               | Digital Sensor Array .....                        | 15 |
| 2.1.3                               | Control Box.....                                  | 16 |
| 2.1.4                               | Servo Motor and Transverse Motion Control.....    | 18 |
| 2.1.5                               | Velocity Profiles .....                           | 21 |
| 2.2                                 | Experimental System .....                         | 22 |
| 2.2.1                               | General Setup.....                                | 23 |
| 2.2.2                               | Heat Source Arrangement.....                      | 26 |
| 2.2.3                               | Thermocouple Unit .....                           | 27 |
| 2.3                                 | Hot-Wire Anemometry .....                         | 30 |
| 2.3.1                               | Frame and CTA Module .....                        | 30 |
| 2.3.2                               | Hot-Wire and Support.....                         | 32 |
| 2.3.3                               | Streamware Software .....                         | 34 |
| 2.4                                 | Data Acquisition Setup .....                      | 35 |
| 2.4.1                               | Hardware.....                                     | 35 |
| 2.4.2                               | Data Acquisition Software – Labview Program ..... | 38 |
| 2.5                                 | Experimental Procedure.....                       | 43 |
| Chapter 3                           | .....   | 46 |
| Validation and Uncertainty Analysis | .....   | 46 |
| 3                                   | Introduction.....                                 | 46 |
| 3.1                                 | Introduction of Vortex Promoters .....            | 46 |
| 3.2                                 | Validation.....                                   | 49 |
| 3.3                                 | Uncertainty Analysis.....                         | 51 |

|                               |   |     |
|-------------------------------|---|-----|
| 3.3.1                         | Heat Transfer Rate Measurement .....                | 52  |
| 3.3.2                         | Pressure Measurement .....                          | 53  |
| 3.3.3                         | Air Velocity Measurement.....                       | 54  |
| Chapter 4.....                |   | 56  |
| Results and Discussion .....  |   | 56  |
| 4                             | Introduction.....                                   | 56  |
| 4.1                           | Results for Vortex Promoters Only in the Flow ..... | 56  |
| 4.2                           | Results for Plate Flow Only.....                    | 65  |
| 4.3                           | Combination of Vortex Promoter and Plate.....       | 73  |
| 4.4                           | Flow Visualizations .....                           | 93  |
| Chapter 5.....                |   | 97  |
| Conclusion & Future Work..... |   | 97  |
| 5                             | Introduction.....                                   | 97  |
| 5.1                           | Conclusions.....                                    | 97  |
| 5.2                           | Future Work.....                                    | 100 |
| Chapter 6.....                |   | 101 |
| Appendix.....                 |   | 101 |
| 6                             | Introduction.....                                   | 101 |
| 6.1                           | Calibration Data.....                               | 101 |
| 6.2                           | Additional Results.....                             | 104 |
| References.....               |   | 108 |



## **List of Tables**

|   |   |
|---|---|
| Table 1.1: Ranges of $h$ for different fluids for Forced Convection [21]..... | 6 |
|---|---|

## List of Figures

|   |    |
|---|----|
| Figure 1.1: Basic Configuration of an electronic system [1] .....               | 2  |
| Figure 1.2: Number of devices per chip [2] .....                                | 3  |
| Figure 1.3: Increasing heat loads [3].....                                      | 4  |
| Figure 1.4: Vertical, Inclined or Horizontal boards in Natural Convection ..... | 5  |
| Figure 1.5: Cray - 2 direct liquid cooling system .....                         | 8  |
| Figure 1.6: An indirect liquid cooling arrangement.....                         | 9  |
| Figure 1.7: Heat Pipe apparatus .....   | 10 |
| Figure 2.1: Aero wind tunnel .....  | 13 |
| Figure 2.2: Siemens Midimaster Eco variable frequency drive.....                | 15 |
| Figure 2.3: Digital Sensor Array.....   | 16 |
| Figure 2.4: Control box.....  | 17 |
| Figure 2.5: Motion controller.....  | 19 |
| Figure 2.6: Step motor driver.....  | 20 |
| Figure 2.7: Transverse mechanism with motor.....                                | 21 |
| Figure 2.8: Velocity Profile in Wind Tunnel with $U = 20$ m/s .....             | 22 |
| Figure 2.9: Test plate .....  | 23 |
| Figure 2.10: Conduction Thermocouple Placement .....                            | 24 |
| Figure 2.11: Top View of Experimental System .....                              | 24 |
| Figure 2.12: Experimental System inside Wind Tunnel.....                        | 25 |
| Figure 2.13: Heat Source Arrangement .....                                      | 26 |
| Figure 2.14: Variable Transformer .....   | 27 |
| Figure 2.15: The Hot Spot Thermocouple Welder .....                             | 29 |

|  |    |
|--|----|
| Figure 2.16: Thermocouple Weld .....   | 29 |
| Figure 2.17: Streamline system Frame and CTA Module .....  | 31 |
| Figure 2.18: Schematic description of hot-wire [28] .....  | 32 |
| Figure 2.19: Hot-Wire Probe-Support Holding System .....   | 33 |
| Figure 2.20: Hardware Setup Screen .....   | 34 |
| Figure 2.21: Schematic of SCXI System .....  | 37 |
| Figure 2.22: Wind Tunnel Program control panels for (a) wind tunnel operation, (b) high speed data logging, (c) block diagram of VI.....           | 41 |
| Figure 2.23: Heat Transfer Program control panels for (a) configuration, (b) instantaneous temperature and heat flux, (c) block diagram of VI..... | 42 |
| Figure 3.1: Relationship between Frequency and Power from FFT .....  | 50 |
| Figure 3.2 : Repeatability and consistency of experiments without a promoter.....  | 55 |
| Figure 4.1: Vertical Positioning of hotwire .....  | 57 |
| Figure 4.2: Horizontal Positioning of hotwire .....  | 58 |
| Figure 4.3: Different positions from 15 mm promoter for (a) RMS of Velocity, (b) RMS / Mean .....  | 59 |
| Figure 4.4: Large Promoter Frequency at $x/h_p = 2$ and $x/h_p = 7.5$ .....  | 60 |
| Figure 4.5: Large Promoter Strouhal number at $x/h_p = 2$ and $x/h_p = 7.5$ .....  | 60 |
| Figure 4.6: RMS of Velocity at $x/h_p = 2$ .....   | 61 |
| Figure 4.7: RMS of Velocity at $x/h_p = 7.5$ .....   | 62 |
| Figure 4.8: Large Promoter Frequency for different separation distances .....  | 63 |
| Figure 4.9: Strouhal number for large promoters for different separation distances.....  | 63 |
| Figure 4.10: Comparison between estimated and recorded velocity by Pitot tube.....   | 64 |

|   |    |
|---|----|
| Figure 4.11: RMS of disturbance by Pitot tube .....   | 65 |
| Figure 4.12: Boundary Layer Profile .....   | 66 |
| Figure 4.13: Heat Transfer rate for the first heater .....  | 67 |
| Figure 4.14: Heat Transfer Rate for the second heater .....   | 68 |
| Figure 4.15: Heat Transfer Coefficient for first heater .....   | 69 |
| Figure 4.16: Heat Transfer Coefficient for second heater .....  | 69 |
| Figure 4.17: Nusselt number for first heater .....  | 70 |
| Figure 4.18: Nusselt number for second heater .....   | 71 |
| Figure 4.19: Comparison of $Q_1$ and $Q_2$ at 16 m/s .....  | 72 |
| Figure 4.20: Comparison of $Nu_1$ and $Nu_2$ for 16 m/s .....   | 72 |
| Figure 4.21: Temperature profiles .....   | 73 |
| Figure 4.22: Temperature profiles on top of first and second heaters .....  | 74 |
| Figure 4.23: Heat transfer rates for 15 mm promoter (a) $Q_1$ , $d/w = 1$ , (b) $Q_2$ , $d/w = 1$ , (c) $Q_2$ , $d/w = 2$ .....                 | 76 |
| Figure 4.24: Heat transfer coefficients for 15 mm promoter (a) $h_1$ , $d/w = 1$ , (b) $h_2$ , $d/w = 1$ , (c) $h_2$ , $d/w = 2$ .....          | 78 |
| Figure 4.25: Nusselt number for 15 mm promoter (a) $Nu_1$ , $d/w = 1$ , (b) $Nu_2$ , $d/w = 1$ , (c) $Nu_2$ , $d/w = 2$ .....                   | 80 |
| Figure 4.26: Heat transfer rates for the first heat source for different plate separations (a) $D/w = 0$ , (b) $D/w = 3$ , (c) $D/w = 5$ .....  | 82 |
| Figure 4.27: Heat transfer rates for the second heat source for different plate separations (a) $D/w = 0$ , (b) $D/w = 3$ , (c) $D/w = 5$ ..... | 84 |

|  |     |
|--|-----|
| Figure 4.28: Heat transfer coefficients for the first heat source at different separations (a) $D/w = 0$ , (b) $D/w = 3$ , (c) $D/w = 5$ ..... | 86  |
| Figure 4.29: Heat transfer coefficient for the second heat source at different separations (a) $D/w = 0$ , (b) $D/w = 3$ , (c) $D/w = 5$ ..... | 88  |
| Figure 4.30: $Q_1$ and $Q_2$ for square and circle promoters (a) 12 m/s, (b) 14 m/s, (c) 16 m/s .....  | 90  |
| Figure 4.31: $h_1$ and $h_2$ for square and circle promoters (a) 12 m/s, (b) 14 m/s, (c) 16 m/s .....  | 92  |
| Figure 4.32: Visualization for plate flow .....  | 94  |
| Figure 4.33: Visualization for 15 mm promoter .....  | 94  |
| Figure 4.34: Visualization for 25.4 mm hexagon promoter .....  | 95  |
| Figure 4.35: Visualization for 25.4 mm square promoter .....   | 95  |
| Figure 4.36: Visualization for 25.4 mm circular promoter .....   | 96  |
| Figure 6.1: Wind Tunnel Calibration between blower speed and Instantaneous and Control Velocity .....  | 102 |
| Figure 6.2: Thermocouple calibration .....   | 103 |
| Figure 6.3: Hotwire calibration .....  | 103 |
| Figure 6.4: $Q_2$ for 15 mm promoter at separation widths (a) $d/w = 3$ , (b) $d/w = 4$ .....  | 105 |
| Figure 6.5: $h_2$ for 15 mm promoter at separation widths (a) $d/w = 3$ , (b) $d/w = 4$ .....  | 106 |
| Figure 6.6: $Nu_2$ for the 15 mm promoter at separation widths (a) $d/w = 3$ , (b) $d/w = 4$ .....   | 107 |

## List of Abbreviations

|                 |  |
|-----------------|--|
| D               | separation width between promoter and edge of plate (mm)                 |
| d               | separation between heat source 1 and heat source 2 (mm)                  |
| e               | uncertainty  |
| f               | frequency (Hz)   |
| H               | wind tunnel height (mm)  |
| h               | heat transfer coefficient ( $\text{W}/\text{m}^2\cdot\text{K}$ )         |
| $h_{\text{av}}$ | average heat transfer coefficient ( $\text{W}/\text{m}^2\cdot\text{K}$ ) |
| $h_p$           | height of promoter (mm)  |
| k               | thermal conductivity of the fluid ( $\text{W}/\text{m}\cdot\text{K}$ )   |
| L               | length of plate (mm)   |
| $\ell$          | distance from edge of plate to first heat source (mm)                    |
| $\text{Nu}_s$   | Nusselt number based on source width                                     |
| Nu              | Nusselt number   |
| Q               | heat transfer rate (W/m)   |
| q               | heat flux ( $\text{W}/\text{m}^2$ )                                      |
| $\text{Re}_L$   | Reynolds number based on plate length                                    |
| $\text{Re}_p$   | Reynolds number based on promoter height                                 |

|       |  |
|-------|--|
| St    | Strouhal number, $St = f h_p / U$              |
| T     | temperature ( $^{\circ}\text{C}$ )             |
| $T_s$ | heat source temperature ( $^{\circ}\text{C}$ ) |
| U     | main stream velocity (m/s)                     |
| u     | local velocity (m/s)                           |
| w     | heat source width (mm)                         |
| x     | local length (mm)                              |
| y     | boundary layer height (mm)                     |
| z     | local height (mm)                              |

### **Greek Symbols**

|          |  |
|----------|--|
| $\delta$ | boundary layer thickness                                   |
| $\theta$ | dimensionless temperature                                  |
| $\rho$   | density of fluid ( $\text{kg/m}^3$ )                       |
| $\nu$    | kinematic viscosity of the fluid ( $\text{m}^2/\text{s}$ ) |

### **Subscripts**

|          |                             |
|----------|-----------------------------|
| $\infty$ | steady-state                |
| 1        | 1 <sup>st</sup> heat source |
| 2        | 2 <sup>nd</sup> heat source |

## Chapter 1

### Literature Survey

#### **1 Introduction**

In this chapter, most of the techniques currently being used for cooling of electronic devices will be discussed. First, our discussion will begin with the electronic package and how it has evolved over the years and how this evolution has kept the operating temperature at an acceptable level. From here, the current cooling techniques available which are air cooling and liquid cooling will be discussed. Then other cooling techniques, mainly focusing on heat pipes and how they work will be presented.

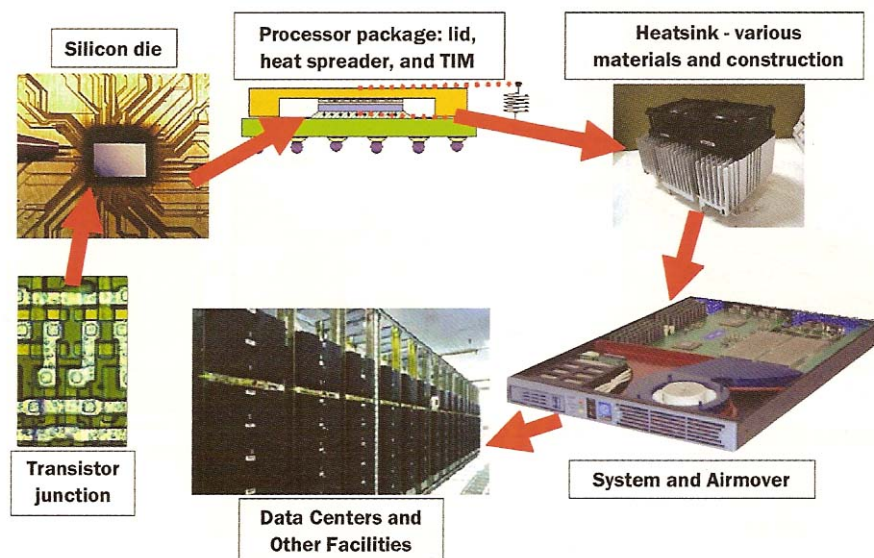
#### **1.1 Electronic Packaging**

For well over 60 years, thermal management and design have been the major obstacles in designing new and advanced electronic systems. When we consider certain applications that use electronic systems, like the military, healthcare and the aerospace industry, control over temperature becomes even more critical. When improvements in



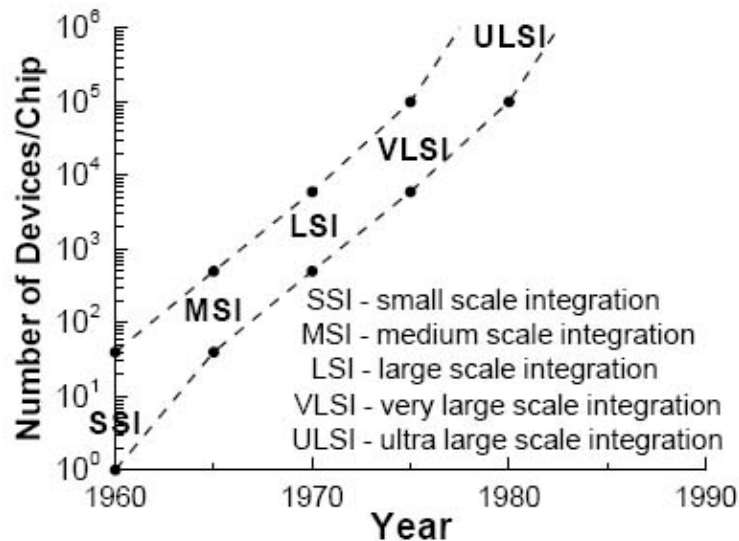
thermal analysis and design become better, faster and more reliable, devices can then be made smaller and more compact.

Figure 1.1 displays the way a computer is assembled. The first step is starting off with the transistors. These transistors are usually made with either copper or aluminum. Moving on to next is the silicon chip. On this chip, there are upwards of a million transistors, based on current technology. From there, the chip is then put into a package. In this package, the chip is held in place between a thermal interface material or epoxy and a substrate. On top of the thermal interface material, the heat spreader is attached. Then the heat is distributed to the heat sink, where air flows take away the heat. From here, depending on the application, a chip and its heat sink are placed in the system with other components, including a fan or pump. Then multiple systems are assembled and used in data centers or other facilities [1].



**Figure 1.1: Basic Configuration of an electronic system [1]**

The concept of the initial integrated circuit first came about in the late 1940's and the early 1950's. Chips during this time were made out of copper oxide and germanium, but starting in the mid to late 1950's, chips were being made out of silicon. In figure 1.2, the scale shows the number of devices per chip versus the time frame at which they were produced [2]. During the 1960's and the 1970's, all of these integrated circuits were being bought and used in military and space systems. Then in the late 1970's and early 1980's, new technologies allowed more chips to be made at a fraction of the initial cost. This brought us to where we are today with number of transistors in the millions and chips measuring on the nanometer scale.



**Figure 1.2: Number of devices per chip [2]**

Chip packages have started to have a lot more transistors on them, thus causing the heat load on them to increase significantly. This leads us to figure 1.3, where heat load per product footprint is shown versus years [3].

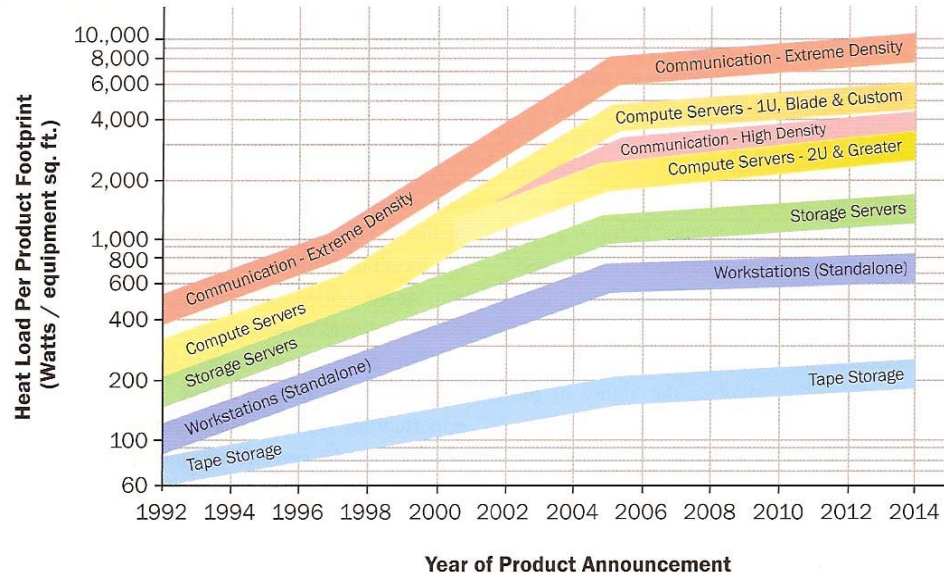


**Figure 1.3: Increasing heat loads [3]**

As products are announced in the upcoming years, new ways will have to be made to combat these rising heat loads to avoid system failures.

## 1.2 Cooling Techniques

With today's electronics, there are many modes of cooling, but the two main types are air and liquid cooling [5, 6]. Air cooling is the most widely accepted solution for cooling because it is relatively inexpensive and has high reliability. It is available in ample amounts and has relatively small maintenance. Out of the 3 main types of heat transfer, convection is the most widely used in cooling processes, but conduction and radiation heat transfer must also be considered as well. First we will consider air cooling techniques and then move on to liquid cooling techniques.

### 1.2.1 Air Cooling

Natural convection air cooling is widely used for systems that have either low power requirements or low package densities. Heat removal rates are much smaller when compared to other methods because natural convection works with buoyancy-induced flows, conduction in the plates and radiation. Most electronic configurations that use natural convection for their cooling use either vertically, inclined or horizontally oriented plates [7, 8], with the working fluid (air) moving from one end of the circuit boards to the other end, as shown in figure 1.4. For high heat removal, either the vertical or inclined positions are preferred [11], but due to size constraints for small scale computers, e.g. Laptop, printed circuit boards are oriented horizontally [9].

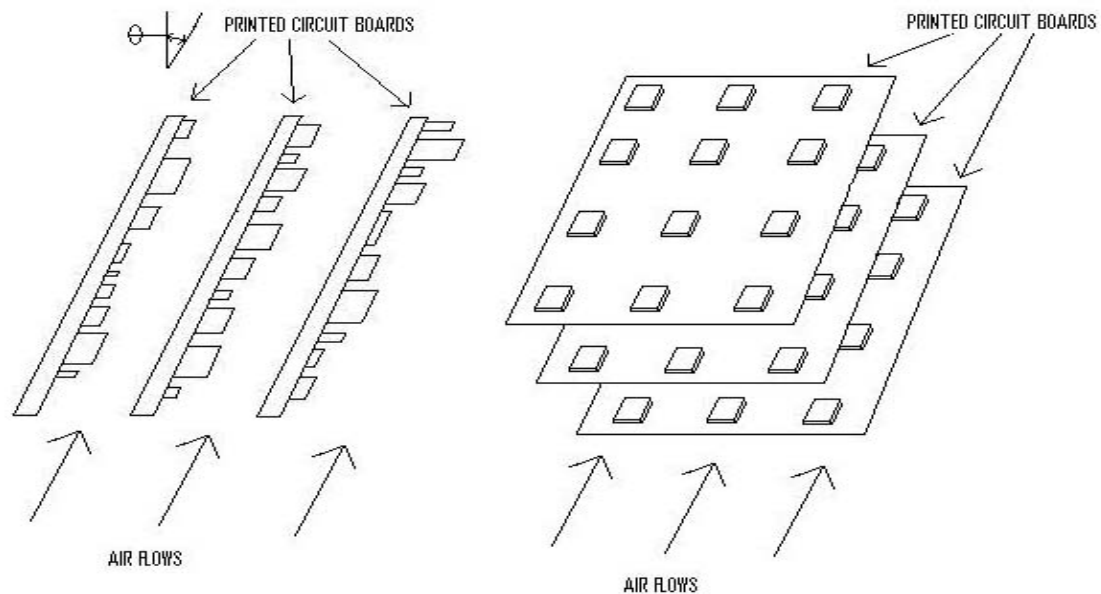


**Figure 1.4: Vertical, Inclined or Horizontal boards in Natural Convection**

Forced Convection is the most popular method for cooling electronic systems. It has higher heat transfer rates when compared to natural convection because the air is being forced around the circuit boards instead of being buoyancy-induced. Studies have

been conducted to show forced convection for the printed circuit boards [12] or for flows over protruding sources [15], which are just enlarged views of printed circuit boards. From this, a better view as to what happens at the printed circuit board level can be seen and be able to understand it better. Now the two other modes of heat transfer, mainly conduction and radiation, must be considered. Conduction plays an important role in heat removal rate with the substrate. The amount that is not being removed by convection is being removed by conduction through the substrate. Radiation heat transfer becomes important only at elevated temperatures.

### 1.2.2 Liquid Cooling

Liquid cooling was developed in the mid 1960's, when current cooling processes were not removing the heat from the system well enough. From the 1960's to the mid 1990's, liquid cooling was the best way to keep the processor and the computer in the operating range.. Then from the mid 1990's, conversion from liquid cooling to air cooling took place because of its cost effectiveness [3]. In general, liquid cooling has higher cooling properties than air cooling does, but does not necessarily make it better. The significant difference can be seen in table 1.1.

| Cooling Properties | $h$ (W/m <sup>2</sup> K) |
|--------------------|--------------------------|
| Air                | 20 - 200                 |
| Oils               | 200 - 2,000              |
| Fluorinerts        | 250 - 2,500              |
| Water              | 1,000 - 10,000           |

**Table 1.1: Ranges of  $h$  for different fluids for Forced Convection [21]**

Table 1.1 shows that the heat transfer coefficient,  $h$ , is much higher for liquid cooling than it is for air cooling. Not only does liquid cooling have the better heat transfer coefficient, but it also has higher specific heats, which allow more heat to be absorbed before the temperature of the fluid would rise. Liquid cooling also has higher thermal conductivity and higher Prandtl numbers which allows more heat to be carried away by convection [21]. Liquid cooling can be broken down into two main parts, direct and indirect.

#### **1.2.2.1 Direct Liquid Cooling**

In direct liquid cooling, the electric components are in direct physical contact with the coolant. For this to work the coolant must have a very large dielectric strength and good chemical compatibility with the printed circuit boards [20], otherwise, damage would be done to the system. Typical characteristic for these types of coolants are low boiling points. The applications that would use direct cooling are pool or forced convection boiling or by single-phase convection, which includes natural, mixed and forced. An example of a direct liquid cooling system can be found in figure 1.5 [21].

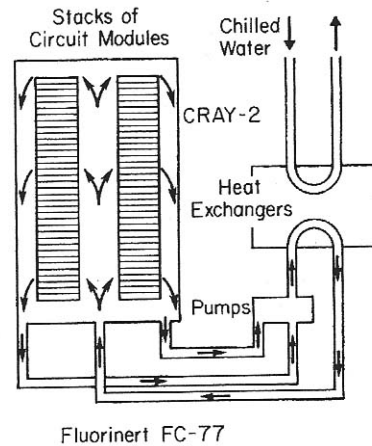


**Figure 1.5: Cray - 2 direct liquid cooling system**

### 1.2.2.2 Indirect Liquid Cooling

Indirect liquid cooling was conceived to avoid the problems associated with direct liquid cooling and to exceed the thermal performance of air cooling. The difference between direct and indirect liquid cooling is that for indirect liquid cooling, the liquid does not come in contact with the multi-chip modules. Heat is usually transferred by means of conduction through an intermediate structure, which is attached to a cold plate. The plate is being kept cold by the coolant being pumped over it. An example of an indirect liquid cooling system can be found in figure 1.6 [21].

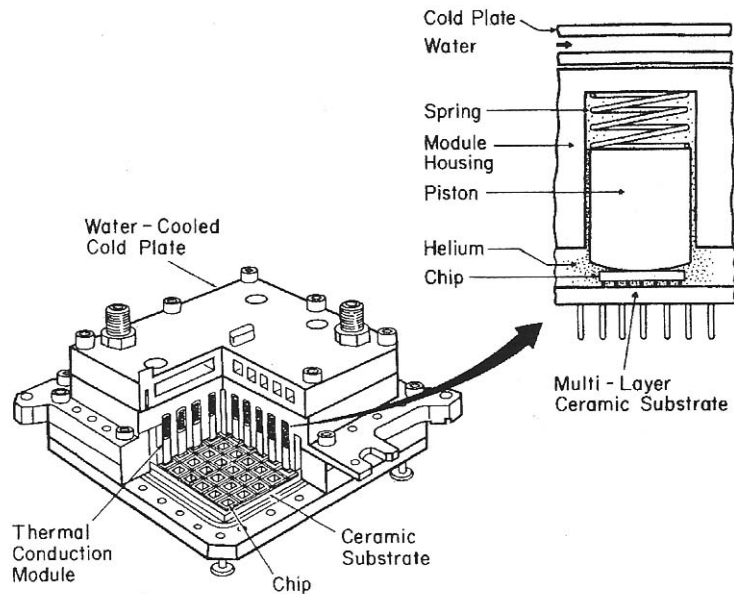


**Figure 1.6: An indirect liquid cooling arrangement**

### 1.2.3 Other Cooling Techniques

The cooling methods described so far are of single-phase convection. There are other types of heat transfer that include phase change. They are nucleate boiling, thermosyphon loops and heat pipes. These systems have a much higher heat transfer rate than the single-phase flows. With the many two-phase cooling techniques out there, heat pipes seem to be the most widely used. Heat pipes became popular in the mid to late 1960's. Heat pipes are a sealed hollow tube, which is made out of a thermoconductive metal, either copper or aluminum and have no moving parts, which require no maintenance. The problems that might occur with heat pipes are: they are tuned to particular cooling conditions. The material, size and the type of coolant all has an effect on where the heat pipes work. The heat pipe is shown in figure 1.7.



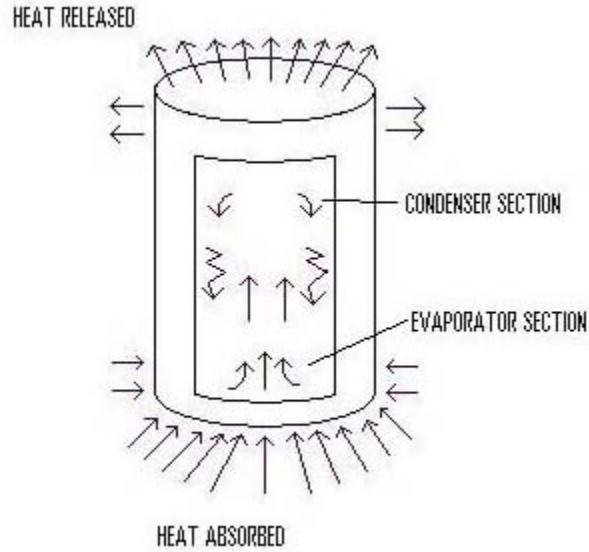


**Figure 1.7: Heat Pipe apparatus**

A heat pipe is made up of 4 parts: heat absorb, evaporator section, condenser section and heat release. When heat first comes into the system, it enters the evaporator section. Here, the liquid is heated up and becomes a vapor. As the vapor rises inside the hollow tube due to higher temperature and pressure, it starts to condense. The condensed vapor starts to fall back down to the evaporator section, because it has given up its latent heat of vaporization and the heat is released to the environment. If the pipe is heated above its working conditions, all the condensed liquid will vaporize, thus causing condensation not to occur and making the heat pipe completely ineffective [22].

### 1.3 Objective of Study

This study is composed of two main parts. For the first part, we look at analyzing the flow behind a vortex promoter. From there we can tell, based on the size and shape of the promoter, what gives us a better oscillatory flow. By using a hotwire anemometer to

study the changing velocity after the promoter (for different initial speeds) we can analyze it to get the power spectra for that particular promoter.

In the second part, we will incorporate the vortex promoter and add a plate that has flush mounted heat sources on it. By picking the appropriate promoter, we then can attach the plate to the setup and record the temperature of the source along its length, the heat flux going into the flow and the change in temperature in the plate itself. We will then use these things to calculate the Reynolds number, the heat transfer to the flow and the Nusselt number for this particular flow. We will then compare these values against each other for different separation distances and for different initial flow rates to find out which setting gives us the best results for a given condition.

## Chapter 2

### Experimental Setup and Instrumentation

#### **2 Introduction**

In this chapter, we will be discussing the main parts of the experiment along with the instruments that are used to get the results. The main component of the experiment is the subsonic wind tunnel. The other components involved in this experiment are the digital process meters, digital sensor, transverse arrangement and heater strips. The temperatures of the heating elements and heat dissipation rates are measured by thermocouples and heat flux sensors, respectively. Data is collected by means of a Data Acquisition system, (DAQ), which includes a Personal Computer Interface (PCI) card that is installed in a computer, a multiplexer and a terminal block. We will then end this chapter with the experimental procedure, which includes the important steps to run an experiment successfully.

## 2.1 Wind Tunnel

In this section we will be discussing the components that help to run the wind tunnel. The instruments used besides the wind tunnel, are a Scanivalve digital sensor array, model number 3017, Ashcroft and Jenco digital process meters, model numbers 2269 and 791 respectively, servo motor and transverse. Then we will give the measured velocity profile of the test section to show that we are working with a uniform flow in the test section.

### 2.1.1 Aero Wind Tunnel

As seen in figure 2.1, this wind tunnel is an Eiffel type or open circuit wind tunnel that was built by Aerolab in 2002. The wind tunnel pulls the air down the test section by a fan at the end of the tunnel. It has a maximum velocity of 71.5 m/s in a clean test section.



**Figure 2.1: Aero wind tunnel**

The wind tunnel is made up of 5 different parts: the inlet, A, the contraction section, B, the test section, C, the diffuser, D, and the exhaust/fan section.

The inlet section, as measured by A, has about a 102 mm deep aluminum honeycomb with 6.4 mm cells which helps to make the flow uniform coming in. Then just after the honeycomb are two 20 x 20 mesh stainless steel anti-turbulence screens. Then the flow moves on to part B, which is the contraction section. This wind tunnel has a contraction ratio of over 10:1, which allows it to take more air over a larger area instead of just in a concentrated area. The contraction is formed by 4 sides of similar curvature, which provide equal pressure and also prevent corner vortices from forming. The static pressure taps, located in the contraction section, allow for the high and low pressure to be measured, so the velocity can be determined using Bernoulli's equation.

The test section, which is part C, is detachable from the upstream and downstream portions of the tunnel. It is 1219 mm long, 711 mm wide and 508 mm tall. It also has two 19 mm thick pieces of acrylic on both sides of the wind tunnel. These panels are located on spring hinges which allow for easy access. As we leave the test section, we now move into the diffuser section, part D. The diffuser is fabricated in 2 sections, which are then bolted and welded together at a flange joint. This process insures that the pressure will not back up into the test section. The last section of the wind tunnel is the exhaust/fan section. Before anything reaches the fan blades, a stainless steel screen mesh of about 13 mm thickness is installed to protect the fan blades. The type of fan used by this wind tunnel is a Joy Size 4 direct drive Axivane Fan. This fan is powered by a 50 hp electric motor and the speed is governed by a Siemens Midimaster Eco variable frequency drive, which is shown in figure 2.2.



**Figure 2.2: Siemens Midimaster Eco variable frequency drive**

### **2.1.2 Digital Sensor Array**

The Digital Sensor Array (DSA) is a stand-alone temperature-compensated, electronic pressure scanner, which can accept up to 16 different pressure inputs or 8 true differential pressure inputs, as shown in figure 2.3. This Digital Sensor Array also contains a piezoresistive pressure sensor with an A/D converter and a microprocessor. This allows it to make an intelligent scan, thus making the measurement more accurate. It has a full range scale from  $\pm 2.5$  kPa to  $\pm 5250$  kPa, with accuracies of  $\pm 0.2\%$  to  $\pm 0.08\%$ , respectively. All this is then powered by a nominal  $+28$  V dc. Also since it is a self-contained pressure scanning system, it requires minimal interfacing by a user [24].



Figure 2.3: Digital Sensor Array

### 2.1.3 Control Box

Since this box is made up of two different process meters, as shown in figure 2.4, the Ashcroft meters and the Jenco meter will be discussed first and then the controls. The Ashcroft digital process meter is an industrial grade micro-processor. This meter accepts all standard process signals and utilizes single button scaling, which allows the meter to be completely programmed by just using one button.



**Figure 2.4: Control box**

The other type of digital meter shown in the control box is the Jenco meter. This type of meter is a Temperature transmitter. It displays the temperature in degrees Fahrenheit, which is based on the signal that is coming in from the thermocouple. The other two controls found on the control box, beside the on/off switch, is the switch between the computer running the wind tunnel (PC) and it being manually run (POT). If the switch is flipped down to the POT setting, then to adjust the speed of the wind tunnel, the silver knob must be adjusted to the correct speed desired.



#### **2.1.4 Servo Motor and Transverse Motion Control**

The Transverse Motion Control unit will be discussed first and then the Servo Motor. The first item is the PCI-7334 motion control card. This card is similar to the PCI cards that will be discussed later in the Data Acquisition section, but this card is designed to only work with stepper motors. The PCI-7334 can provide motion control for up to 4 independent or coordinated axis of motion. Each axis has motion I/O for trigger inputs and encoder feedback rates up to 20 MHz. It also has a trajectory generator, a stepper control block and at least one stepper pulse generator output. All these functions are available because of advanced dual-processor architecture. This card also supports the Real-Time System Integration (RTSI) bus, which provides high speed connectivity between National Instruments Products. This PCI card is then connected to the UMI-7764 motion control interface, which controls the signals to the stepper motor and transverse mechanism. The motion control interface, as shown in figure 2.5, can support up to 4 axis of simultaneous or independent control and each axis has a motion I/O terminal block. The terminal block has 4 groupings called: Amplifier/driver connections, Encoder connections, Switch connections and Distributed power connections [25].

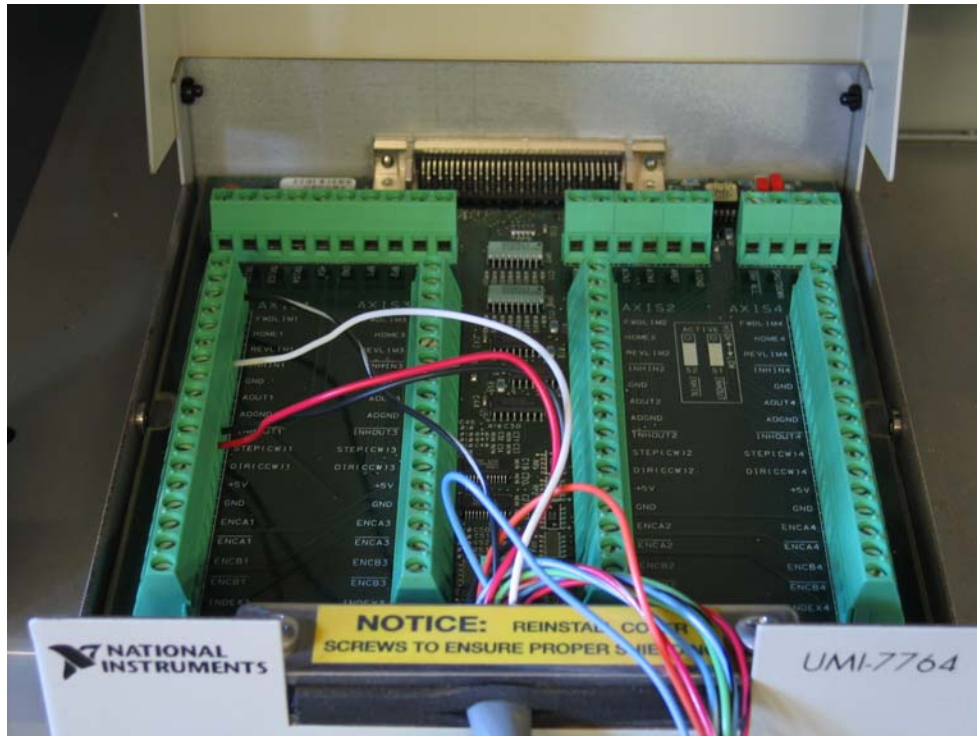


**Figure 2.5: Motion controller**

Since the motion controllers have already been discussed, the stepper motor and the transverse mechanism is presented. The motor that is used for the motion is a PDO 3540 Packaged Pulse and Direction Step Motor Drive, as shown in figure 2.6. This step motor has 4 modes of operation: Self Test, Pulse and Direction, joystick and oscillator. For what we need, the Pulse and Direction option is chosen. This option can make between 200 and 50,800 steps per revolution and allows the drive to receive step pulses from an external controller. This makes the PDO 3540 a powerful, precise and efficient driver.

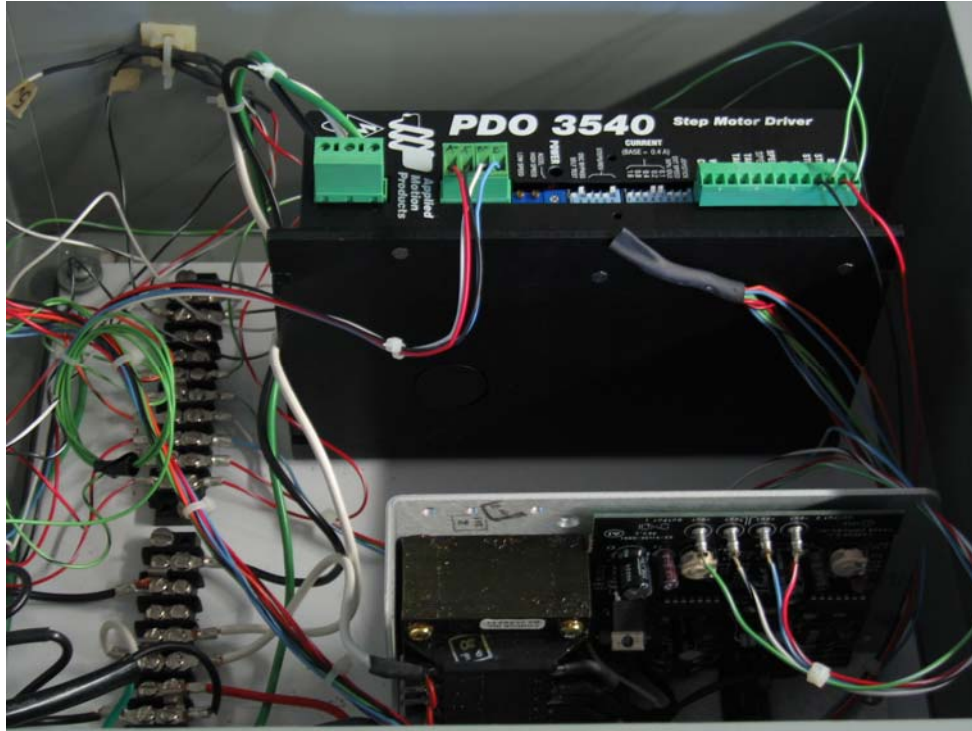


**Figure 2.6: Step motor driver**

In figure 2.7, the transverse mechanism, made by Servo Systems Corporation, has a 127 mm travel length with an anti-backlash lead screw assembly. The lead-screw has an efficiency of 81% and has a straightness of 0.051 mm over a 102 mm travel distance. Sensors on the side rails of transverse can be adjusted along the travel length to set the home and limit positions. These sensors are then activated by the use of a trigger located on the side of the carriage.



**Figure 2.7: Transverse mechanism with motor**

### **2.1.5 Velocity Profiles**

The velocity profile in the test section of the wind tunnel is described here. The measurement of the profile was taken at 546 mm from the inlet of the test section and the velocity was measured for the entire height ( $H = 508$  mm) of the test section. The measuring device used to attain the velocity profile was the Pitot tube. The Pitot tube

collected 1 sample per second at each point and each point is the average speed. In order to change its position, the transverse mechanism, as describe earlier, was used. The results from this test, as shown in figure 2.8, verifies our assumption of uniform flow inside the main part of the wind tunnel. The maximum amount of variation that occurred in the experiment was  $\pm 0.6\%$ . This variation is without any effects from the walls.

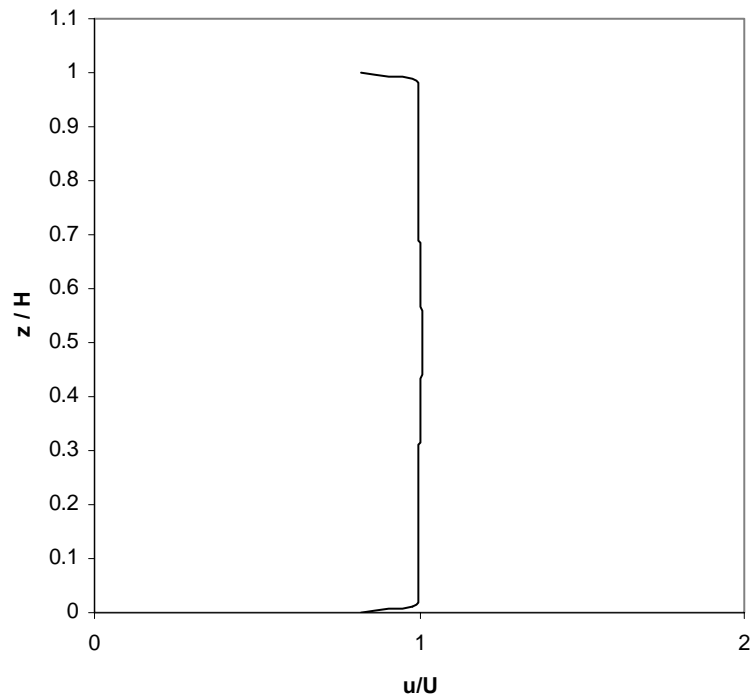


**Figure 2.8: Velocity Profile in Wind Tunnel with  $U = 20$  m/s**

## 2.2 Experimental System

In this section, we will be discussing all the parts that constitute the experimental system that goes inside the test section of the wind tunnel. This part is broken up into 3 main parts: the general setup, the heat source arrangement and the thermocouple unit.

### 2.2.1 General Setup

The general setup of the experiment is made up of many components. Materials that have been used to make this structure are aluminum, cast acrylic and teflon. The first component that will be discussed is the test plate, where the heat sources are placed. In figure 2.9, we see the test plate that is used in this experiment. The test plate is made of mechanical grade PTFE (Teflon) that is 263.5 mm wide and is 305 mm long. This plate also has 2 grooves in the plate, 5.7 mm wide, for the heat sources to slide for different separation distances.

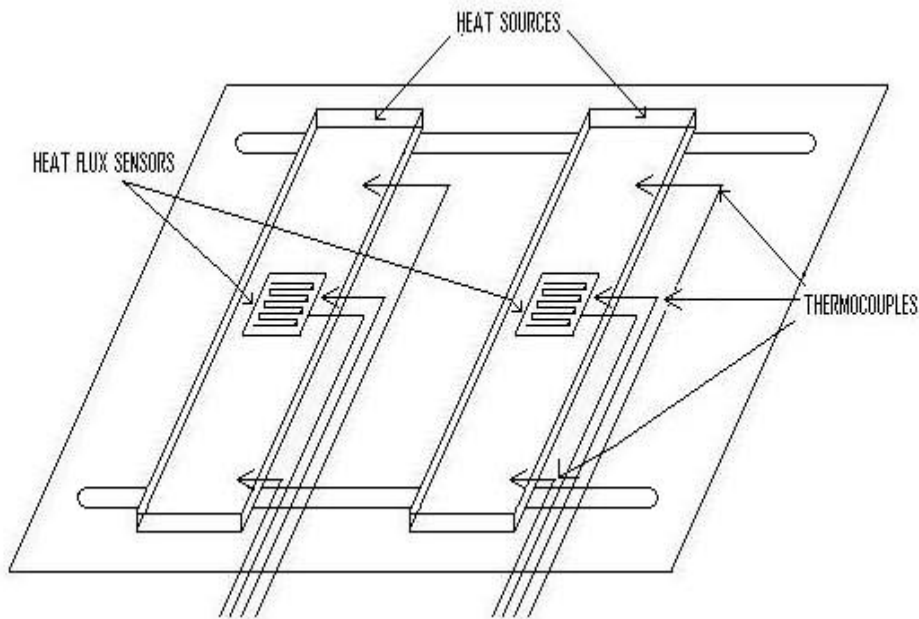


**Figure 2.9: Test plate**

As shown in figure 2.10, eight holes have been drilled into the bottom of the plate in order to measure the temperature change as it passes through the plate. There is a total of four holes drilled to just about the surface and the other four holes are slightly drilled,

about one to two millimeters into the teflon, to allow the temperature change from the top surface to the bottom surface to be recorded.

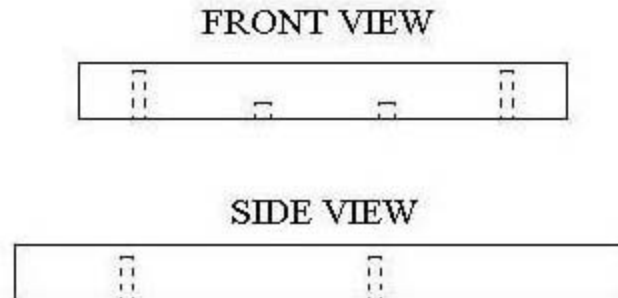


**Figure 2.10: Conduction Thermocouple Placement**

The next part of the experimental structure is the main part. Here we will be discussing the bottom aluminum plate and the parts that are attached to it. In figure 2.11, the top view of the experimental system is shown. The T-design was chosen to reduce the cost and the amount of material that was needed and to be able to secure it to the plate in the wind tunnel. The entire length of the aluminum is about 686 mm and at the back end is 514.5 mm across and at the front is 260.5 mm across.

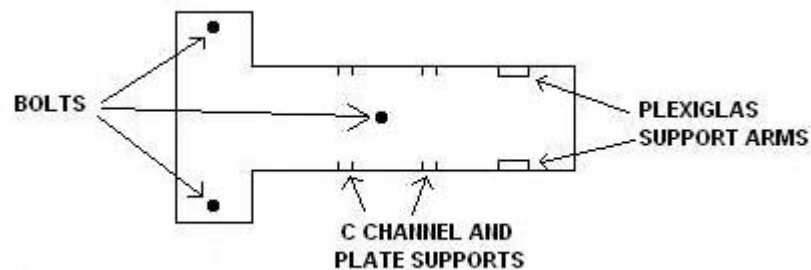


**Figure 2.11: Top View of Experimental System**

In figure 2.12, the side view of the experiment is shown. Starting from the left, two bolts are used to help secure the back end of the structure to the wind tunnel. Then moving towards the right, four support arms for the test plate are seen. These support arms are C Channel design, made with aluminum and are attached to the aluminum plate by angle bar and two screws each. The C Channel arms are 254 mm tall and then attached to them at the top are the supports that the plate sits on. These supports were made out of cast acrylic and have two screw holes in them. One screw is to secure it to the C Channel and the other is to secure the plate to the arms. Finally as we reach the front of the experiment, two cast acrylic promoter arms are seen. These arms support the different vortex promoters/generators used in the experiments. These arms are about 330 mm tall and about 20 mm thick.

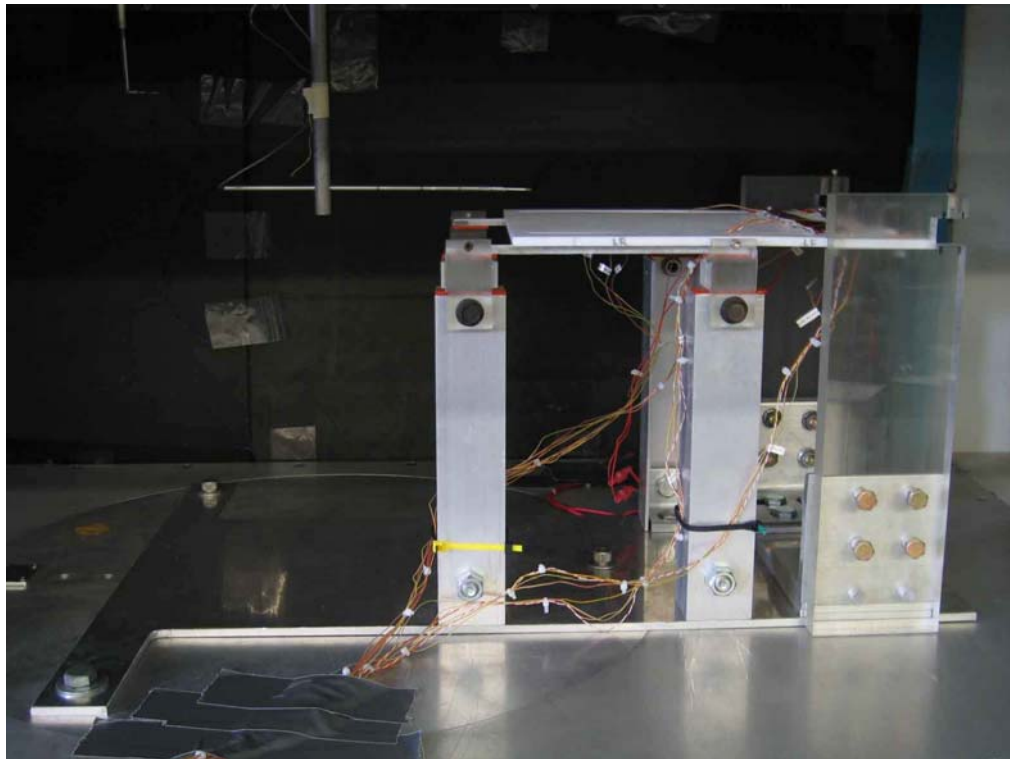


**Figure 2.12: Experimental System inside Wind Tunnel**



### 2.2.2 Heat Source Arrangement

The heat sources, as previously shown in figure 2.9, are described in more detail and how they are arranged to simulate a computer chip. Figure 2.13 shows the side view of the heat source arrangement. The arrangement starts off at the bottom with a thin copper plate. Copper is used because of its high thermal conductivity. Placed on top of the copper plate is a thin layer of Omegatherm Epoxy Silicone Paste. The Omegatherm Epoxy Silicon Paste is a putty-like paste that stays soft up to 200°C. This paste has a thermal conductivity of 2.308 W/(m\*°C). Next the heat flux sensor and thermocouple wires are placed on the Epoxy paste. The heat flux sensor is a thin film sensor that functions as a self-generating thermopile transducer and is designed for precise measurement of heat loss/gain on any surface but is only rated up to 150°C. Then another layer of Epoxy paste is applied to ensure that the heaters and the heat flux sensors and thermocouples are not directly touching. Then the heater strip is placed on top. The heater strips are Kapton insulated flexible heaters. They are made up of an etched foil element sandwiched between two layers of Kapton. The maximum thickness of the heaters is 0.25 mm and is rated up to 200°C [26].

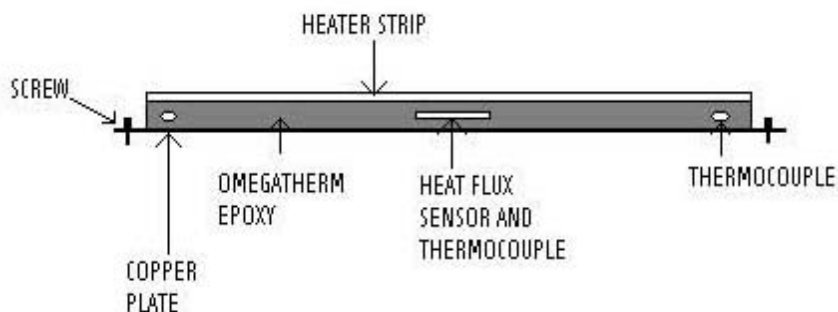


Figure 2.13: Heat Source Arrangement

The heater strips, as described above, are then plugged into the variable transformers. These transformers allow the amount of power sent to the heater strips to be varied, so we can set the heaters to operating at partial capacity instead of just fully on at 120 V or fully off. One of the variable transformers used in the experiment can be seen in figure 2.14.



**Figure 2.14: Variable Transformer**

### **2.2.3 Thermocouple Unit**

Thermocouples made in the lab, are made by a Hot Spot Welder. The type of thermocouple wire used in the lab is a K-type thermocouple wire. This type of wire, which is made by Omega Engineering, has special limits of error, which has an accuracy

of 0.4% above 0 °C or 1.1 °C. The thermocouples are made up of Chromega (Ni-Cr) and Alomega (Ni-Al). The gauge of the wire is 30 AWG and is about 0.5 mm in diameter. According to the color codes for a K-type thermocouple, the yellow wire, Chromega, is positive and the red wire, Alomega, is negative [26]. These two wires are then welded together using a Hot Spot Welder. Special care is taken when making the thermocouple, to make sure that the wires only touch at the tips.

The Hot Spot Capacitive Discharge Welder, as shown in figure 2.15, generates an electric arc for fusing standard couple elements into freestanding beads. The system is powered by 115 VAC, by means of a step-down transformer. When the unit is turned on, by adjusting the power control knob, different levels can be set as to how much of a charge is stored. The Hot Spot is rated from 5 to 50 watt seconds. For these experiments, a level of 20 watt seconds is ideal. Then before the charge can be discharged, the wires that are to be welded must be held together by the pair of pliers and the two tips must be in contact with the carbon block. Once all is set, the black button may be pressed and the charge is sent to the wire, which releases a burst of heat that locally melts the wire with the carbon block, thus forming a spherical weld.

When the spherical bead is formed between the two wires, a strong weld which have shorter wires, can withstand the tests. Then there are weak welds which have long wires and break when touched. As shown in figure 2.16, the two thermocouples show the difference between a strong weld and a weak weld. On the left, is the strong weld, because of the shortness of exposed wire and a more spherical bead. The weak weld, as shown on the right, has too much wire exposed, which could lead to false temperature readings.



**Figure 2.15: The Hot Spot Thermocouple Welder**



**Figure 2.16: Thermocouple Weld**

Thermocouples were then calibrated at 4 different temperatures: melting ice, 21°C, 55°C, and 76°C. The thermocouples are then placed into the water, which is then put into an oven. The temperature of the water is measured by a thermometer to get the temperature to the desired level. When the temperature has reached a steady-state, data are then recorded. The calibration of the thermocouples can be found in appendix A.

## **2.3 Hot-Wire Anemometry**

In this section, all the parts of the Streamline system by Dantec Dynamics will be discussed. This system is an integrated measuring system based on the high performance Constant Temperature Anemometer (CTA) and a personal computer (PC). In the sections to come there will be three main parts: the frame and CTA module, hot-wire and support, and the Streamware software. The first part to be discussed is the frame and CTA module.

### **2.3.1 Frame and CTA Module**

The first thing that we will be discussing is the frame. The frame, as seen in figure 2.17, can hold up to 6 CTA modules (1 shown) and has the input for an ambient temperature probe. The frame, which consists of two main components, is the controller, which is the gateway from the PC to the Streamline system and the ambient temperature probe. The controller serves three main purposes: first, it transfers and stores the setup parameters for the modules. Next it is a transient recorder for sampling of CTA square

wave responses. Lastly, uses a DC voltmeter to measure data from the probe resistance, the CTA bridge top voltage during balance and from the ambient temperature transducer connected to the frame. The ambient temperature probe is a thermistor based thermometer that is used to measure the ambient fluid temperature in connection with CTA probe.



**Figure 2.17: Streamline system Frame and CTA Module**

The CTA module contains two main parts, the Constant Temperature Anemometer and the signal conditioner. The Anemometer works according to the CTA principle when a probe forms a part of the wheatstone bridge. The Anemometer has two bridge configurations: 1:20 and 1:1. The 1:20 bridge configuration is the most widely used. It incorporates internal high precision decade setting, which determines the operating temperature of the probe. The 1:1 bridge configuration is only used in special situations, mainly when the probe is at a far distance from the CTA module. Then an external overheat resistor, matched to the specific probe is required [27]. The probe is prevented from burning out by a protection circuit that switches off the current when the

probe is disconnected unintentionally when in operate mode. The signal conditioner is used to match the CTA bridge output voltage to the input range of the A/D converter board in a PC and it also filters the signal. In order for the output from the signal conditioner to maintain max stability, an internal offset compensation is implemented.

### 2.3.2 Hot-Wire and Support

The hot-wire anemometer provides an output signal continuously which is related to the instantaneous velocity acting on a heated sensor, normally a thin wire placed into the flow. The wire, as shown in figure 2.18, is a 5  $\mu\text{m}$  diameter wire, made of tungsten and is 1.25 mm long. This wire is then connected to two needle-shaped prongs which are planted in a ceramic tube and has gold connectors at the end. The probe has a range of a few cm/s to supersonic speeds and has the ability to have up to a 150°C ambient temperature. A single sensor miniature wire probe, model 55P11, is used in all experiments. This probe has a cold sensor resistance of 3.1  $\Omega$  and can withstand frequencies up to 150 kHz [27].

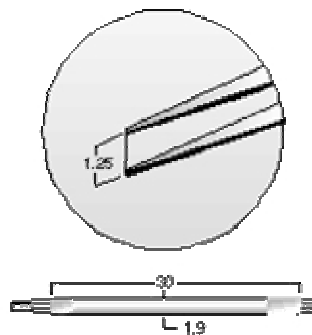


**Figure 2.18: Schematic description of hot-wire [28]**

In order for the wire probe's signal to reach the anemometer, it must be connected to a support. The support, as seen in figure 2.19, the support connects the probe to the CTA module, while at the same time gives support to the probe mechanically. For the experiments, model 55H21, straight support is used. In order to get the straight support to stay at a certain height, a connecting rod, which is attached to the transverse mechanism, allows the hotwire probe and support to be moved up and down in the flow. Then to hold the probe in place, a set screw is tightened at the bottom of the rod.

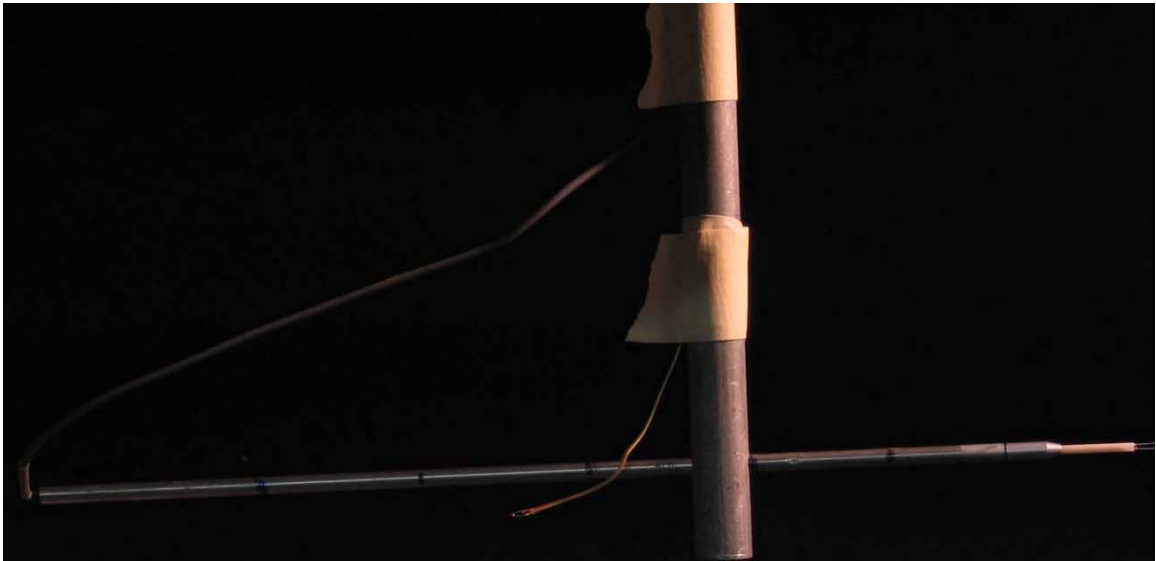


**Figure 2.19: Hot-Wire Probe-Support Holding System**

The hot-wire output is calibrated by using a Pitot tube. The Pitot tube is attached to the connecting rod and is placed 3 cm above the hotwire support in the center of the channel. The calibration data, as shown in Appendix A, is used to convert the analog signal given by the anemometer to air velocity.



### 2.3.3 Streamware Software

The Streamware Application Software offers a complete user interface, inside a Microsoft Windows environment, for controlling the Streamline Hardware system and for acquiring, processing and presenting data. It allows you to make and adjust the hardware configuration setup for each individual module (overheat ratio, square wave tests), calibration of probes and to allow collection and reduction of data.

The PC communicates with the frame by means of a serial comport. Upwards of 3 frames can be combined to run from the same PC, thus allowing up to 18 separate channels [27]. Figure 2.20 shows the hardware setup screen in the Streamware program. From the hardware setup, different types of probes can be selected along with the type of supports. Once the probe and support are connected to the module, the overheat ratio can be set and the probe can be set to operating mode to acquire data.

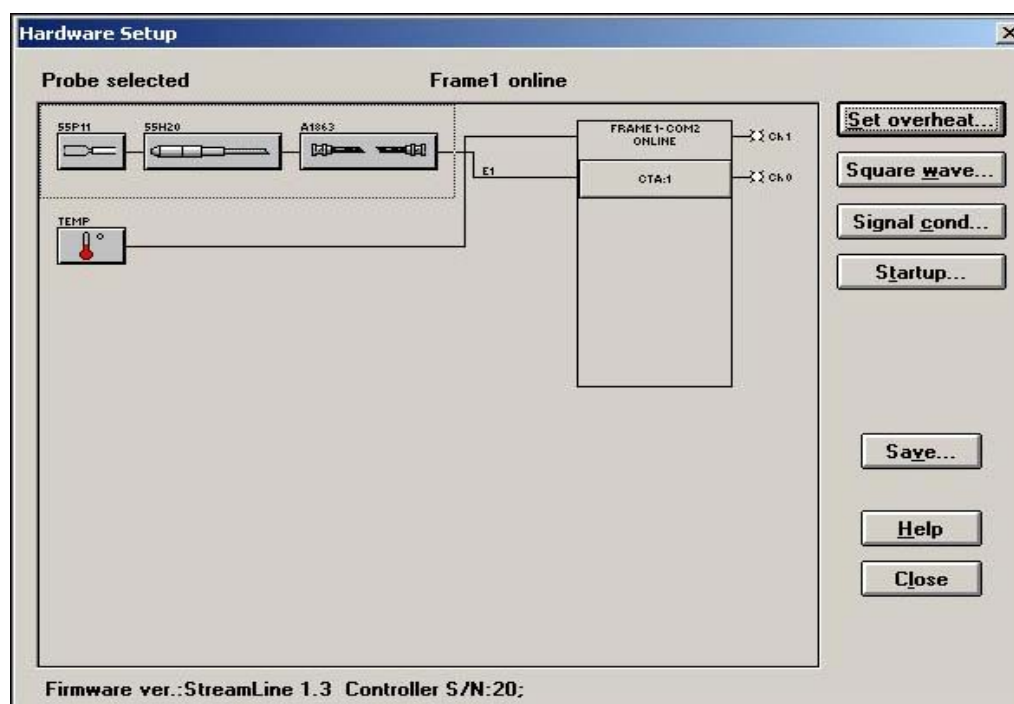


Figure 2.20: Hardware Setup Screen

## **2.4 Data Acquisition Setup**

In this section, we will be discussing all the components that are used to acquire data. In this first section, we will be discussing the hardware setup, which starts with the data acquisition cards and then moves on to the Signal Conditioning Extension for Instrumentation (SCXI) system and the bayonet Neill-Concelman (BNC) connector. The last section talks about the software used for the data acquisition system. Here we will be discussing the program Labview and the programs that have been written for this thesis. Now we will start to talk about the hardware setup.

### **2.4.1 Hardware**

The two DAQ cards that are used in this experiment are both National Instruments® PCI-6040E model E series multifunction DAQ cards. One card is used to acquire the heat flux and temperature and the other card is used to get the air velocity by means of the hot-wire anemometry and collects the ambient temperature for the wind tunnel. This card can support up to 16 single ended or 8 differential analog inputs. The resolution of the card is 12-bits for the analog input. The max sampling rate for a single channel is 500 kHz, but for multiple channels, the sampling rate is reduced down to only 250 kHz. The maximum working voltage for this card is +/- 11 Volts from ground. So if we keep the analog input between 0 to 10 volts and the analog output between -10 volts to 10 volts, we should then be able to prevent damage to the circuit. This card also features digital triggering capability, as well as two 24-bit, 20 MHz counter/timers. The measurement devices that are connected to the first PCI-6040E DAQ card by means of

the SCXI system, which consists of a chassis, module and a terminal block. The connections to the other PCI-6040E DAQ card are made by using a BNC Connector.

The SCXI system is used to connect the measurement devices to the data acquisition card. The system allows multiplexing, filtering and amplify the signal of the measuring devices. These features will increase the number of channels, but will also make the readings of the sensors and the thermocouples more accurate. The main components of this SCXI system are the SCXI-1000 chassis, SCXI-1100 multiplexer module and the SCXI-1300 terminal block. The setup of the SCXI system is shown in figure 2.2

The SCXI-1000 is a four slot chassis and can hold up to four SCXI modules. The chassis contains an analog bus, a digital bus, and a chassis controller that regulates the bus operation. The analog bus transfers the analog signals from the resident module to the DAQ device, using a connection formed between the module and the DAQ card. The digital lines of the DAQ device talk with the SCXI chassis controller and help to manipulate the digital bus, which also controls the operation of the chassis. No more than 10 signals are being processed at the same time. For these experiments only 1 module is being used.

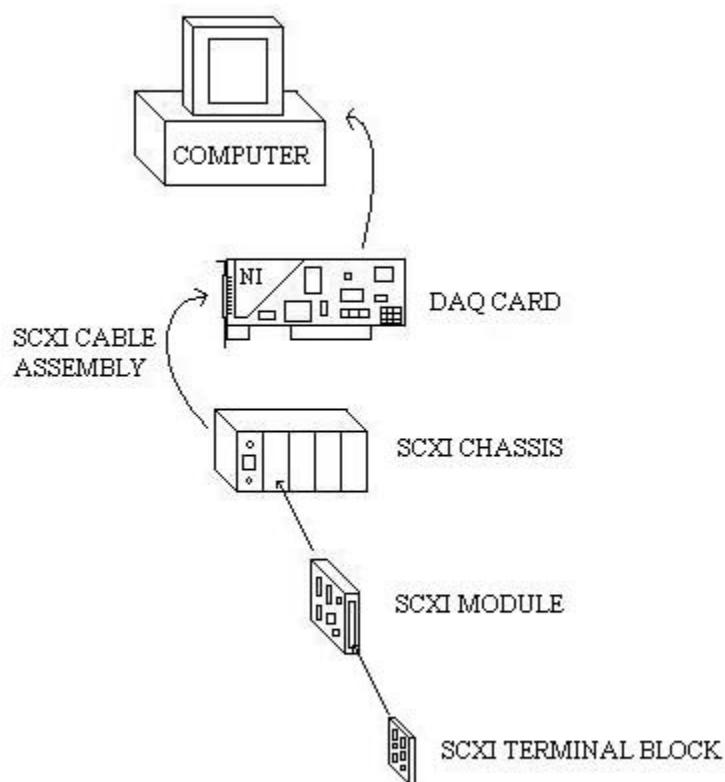


**Figure 2.21: Schematic of SCXI System**

The SCXI-1100 operates as a fast 32 channel differential multiplexer/Amplifier. It is designed for low-cost signal conditioning of thermocouples and for high accuracy thermocouple measurements, which is good for heat transfer experiments because they require a large amount of thermocouples. It can acquire millivolt, volt and 0-20mA current sources. Each one of the input channels has an instrumentation amplifier and a 2 Hz low pass filter, which eliminates the noise from 50 or 60 Hz power sources. It then multiplexes the 32 input channels into 1 channel of data for the DAQ card after the signal conditioning.

Thermocouples measurements also require cold junction compensation. The SCXI-1100 module can read the cold junction compensation from any of the compatible terminal blocks. An example of one of these blocks is the SCXI-1300.

The SCXI-1300 terminal block is a 32 channel isothermal block that is a shielded board with terminal screws on it and is able to connect to the SCXI-1100 module. Located inside the casing, is an isothermal copper plane. This plane allows temperature gradients to be minimized across the screw terminals when using the thermocouples. The terminal block also has 72 screw terminals for easy connection. Thirty-two pairs of screw terminals connect to the 32 differential inputs of the SCXI module. One pair of terminals is connected to the module's chassis grounding pins.

The BNC-2120 terminal has shielded connector blocks with BNC connectors for easy connectivity between the analog input and analog output signals to the DAQ card. It also provides a function generator, quadrature encoder, thermocouple connector and a temperature reference. The BNC-2120 has 8 analog input channels, 2 analog output channels and 8 digital input-output channels. The signal generator that is built-in can send triangle, sine and square waves with a frequency range of 100 Hz to 1 MHz. This BNC terminal block is being used for connecting the analog signal from the hot-wire anemometry to the DAQ card, measures the ambient temperature for the wind tunnel and allows the temperature, pressure and PC control from the Ascroft and Jenco Box to be placed into the Labview program.

#### **2.4.2 Data Acquisition Software – Labview Program**

The Labview Programming language allows programmers to develop an application with a great amount of functionality. They can either use the data acquisition


and instrument control to run the program or they can do without it. Labview uses a file called a VI (Virtual Instrumentation) as its source code. It has two separate levels of codes: high level and low level. High level codes are what the programmers create. Low level codes are what Labview compiles the VI's into, which is not viewable by the user.


Labview is programmed in two separate windows. The first window is the Front Panel and the other window is the Diagram Panel. Programming is composed of wires and icons. The Front Panel has the user interface, where all visual tools are shown, such as text boxes, gages, graphs, etc. The Diagram Panel has all the wiring of the components and has control of the program.

Figure 2.22 and Figure 2.23 show the control panels and the wiring diagrams of the Labview program developed for these experiments. The wind tunnel program, as shown in figure 2.22 has two control panels and a wiring diagram. The first control panel runs the wind tunnel operation, while the second panel runs the high speed data logging for oscillatory flow. In figure 2.23, the heat transfer program is shown. This also has two control panels and a wiring diagram. The first control panel is for configuring the channel, devices and text files. The second control panel is used for monitoring instantaneous temperatures and the heat fluxes.

main instantaneous

if scan button is ON, High Speed  
Logger Runs  
if scan button is OFF, Wind Tunnel  
Runs

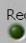
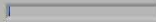
scan 

 **Rutgers University**  
Mechanical and Aerospace Engineering

p\_inf [Pa] **104200** T\_inf [C] **18.00**

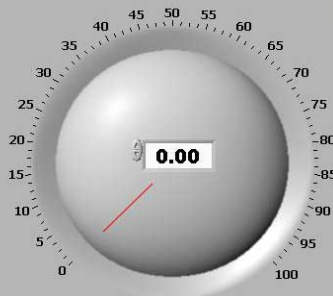
instantaneous freestream  
velocity [m/s] **0.00**

average freestream  
velocity [m/s] **0.00**

# of samples **1** Record Data  scanning progress 

File name  File Header Text  
Blower Speed:  
promoter type:  
position:

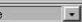
seconds to wait **1.00** Output File Reading Labels  
Avg. Instant. Velocity

blower speed [m/s] 

created by vasilje j. jovanovic  
modified by Kevin Gomes

(a)

main instantaneous

channels (0)  

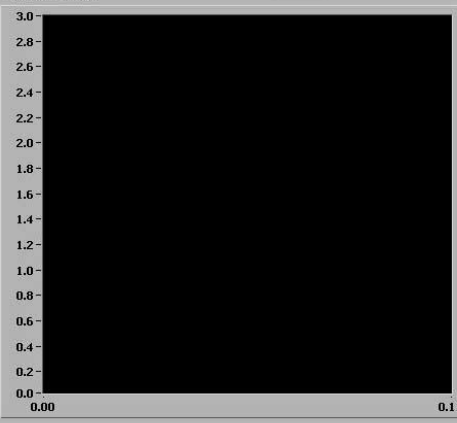
scan rate

device (1)

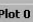
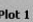
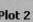
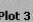
Total No. of Data  Buffer size

Number of scans to write  
at a time

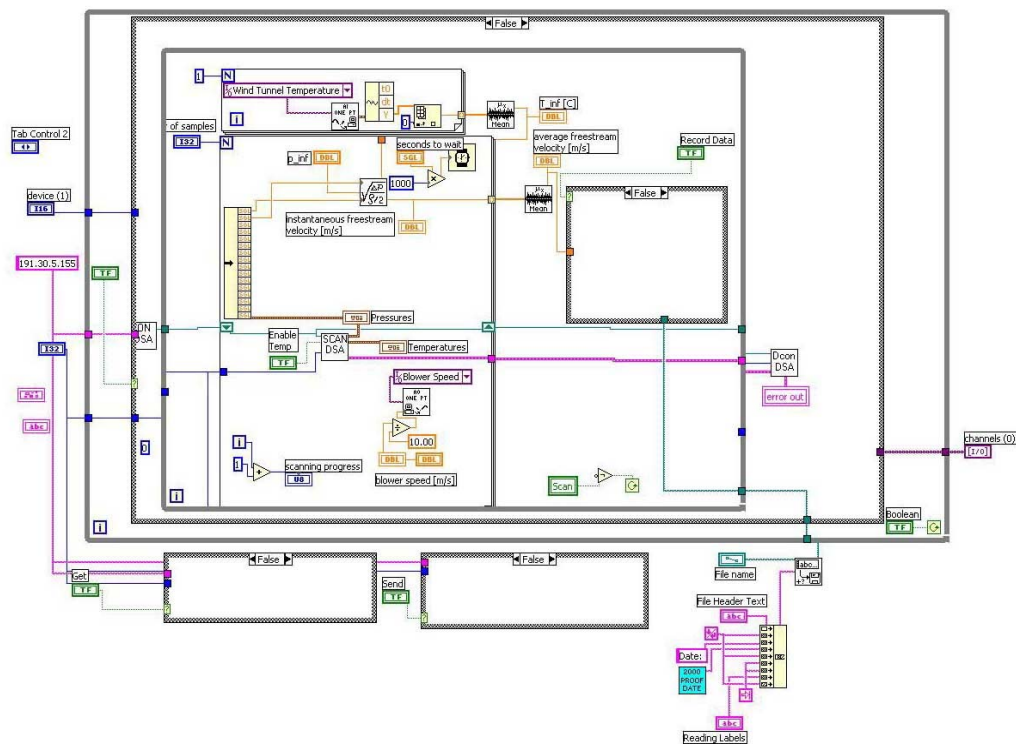
No of Data Written so far

waveform chart 

Numeric 2

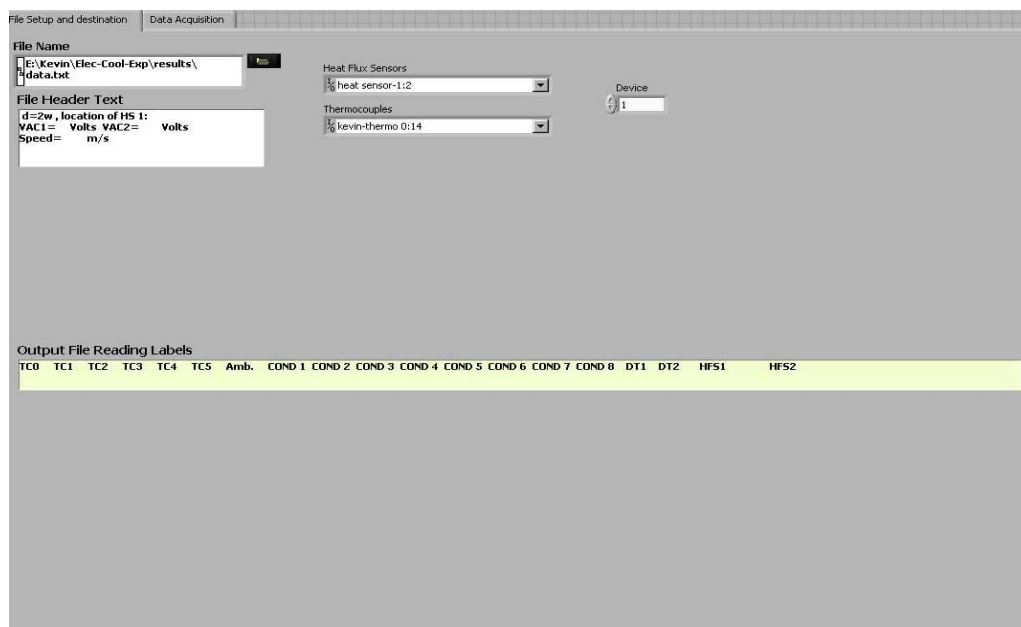
Plot 0   
Plot 1   
Plot 2   
Plot 3 

(b)



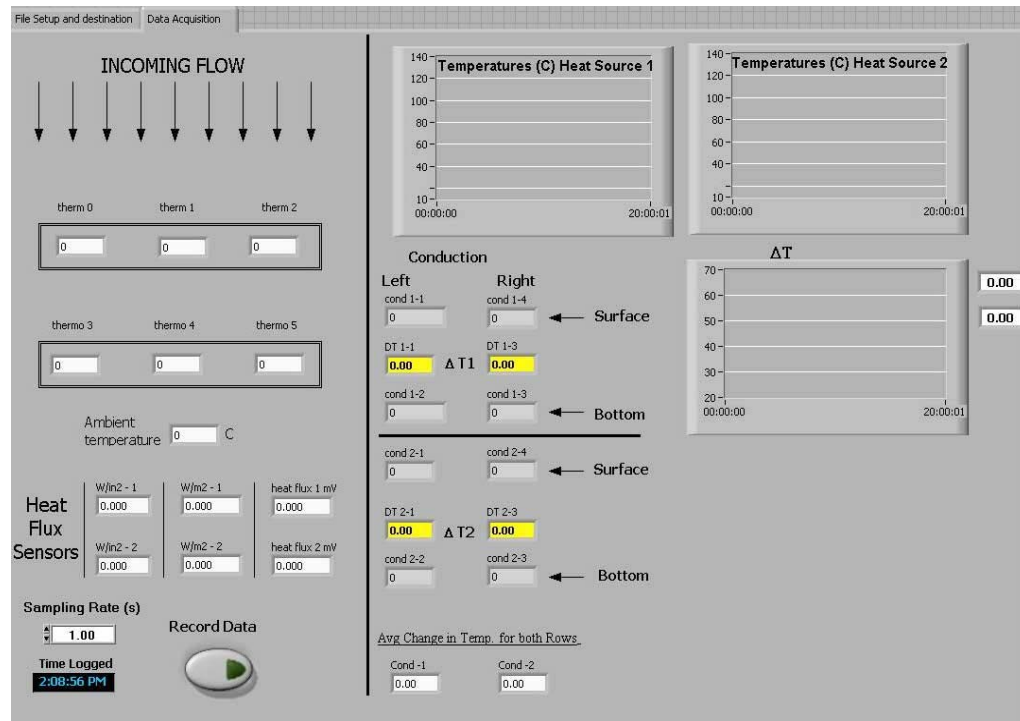
(c)

**Figure 2.22: Wind Tunnel Program control panels for (a) wind tunnel operation, (b) high speed data logging, (c) block diagram of VI**

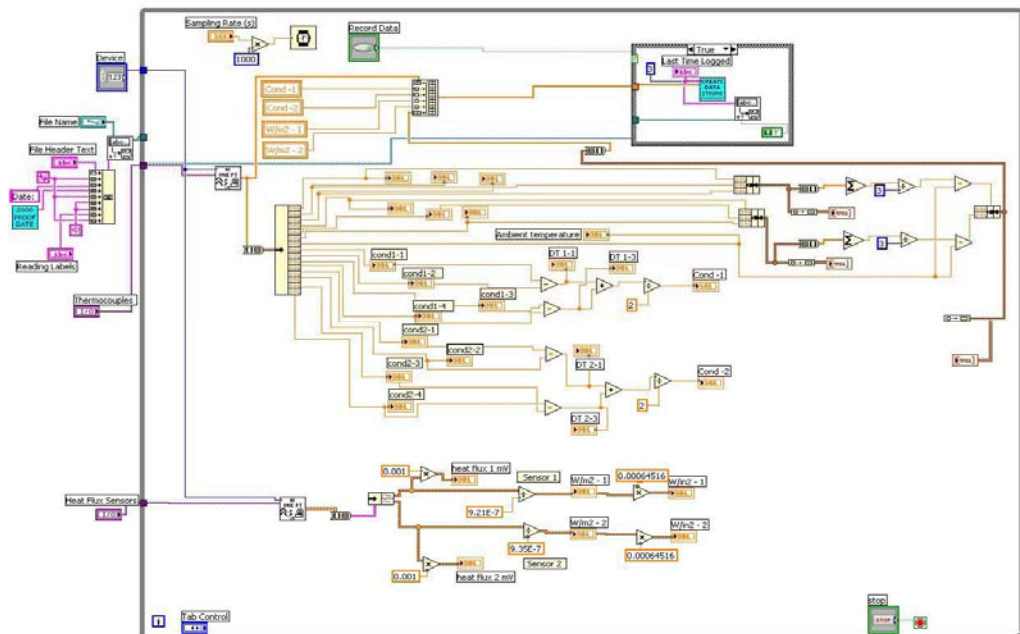


(a)





(b)



(c)

Figure 2.23: Heat Transfer Program control panels for (a) configuration, (b) instantaneous temperature and heat flux, (c) block diagram of VI

## 2.5 Experimental Procedure

This section describes a step-by-step procedure in order to perform the experiment:

1. Turn on computers.
2. Make sure no foreign objects are inside the wind tunnel.
3. Check to see that the test section is securely closed.
4. Walk around wind tunnel and open gate to outside. Pull out pin that is holding the chain in place to raise the gate. Once open, secure gate in place by putting the pin back through the chain.
5. Lift power switch to wind tunnel.
6. Turn on Ascroft & Jenco Control Box and set switch to PC.
7. Push the emergency stop button in and pull it back out.
8. Open up Streamline software and turn on Streamline box to setup the hot-wire probe. Also turn on the SCXI system.
9. Open Labview software and inspect to make sure everything is operating properly.
10. Check pressure on barometer and input the value, in Pascals, into the Labview program.
11. Switch over to the other computer and load the other Labview program.
12. Start both Labview programs.
13. Turn on the heaters by means of the variable transformers.

14. Increase wind tunnel speed to the desired amount.
15. Adjust heaters to the correct percentage.
16. Wait and adjust heaters until  $T_s - T_\infty$  is  $60^\circ\text{C} \pm 0.38^\circ\text{C}$ .
17. Once steady-state has been reached, start data logger and record voltages.
18. Record data for 60 seconds. Then switch over to other Labview program.
19. Run high-speed data logger for hot-wire system to get the velocity fluctuations.
20. Once all data logging is complete you can:
  - a. Change the velocity to desired speed and continue back on to step 15.
  - b. If hardware change is needed, first change text file name and turn off variable transformers. Wait till the temperature has dropped below  $30^\circ\text{C}$  and then set the wind tunnel speed to zero in the wind tunnel program. Then perform the necessary fixes and then return to step 12.
  - c. If all experiments for the day are completed, please continue on in the procedure.
21. Change file name to make sure you do not overwrite your data. Also check files to make sure there was enough data acquired.
22. Turn off the variable transformers and allow the temperature to drop below  $30^\circ\text{C}$  before turning off the air flow.
23. Once the temperatures of the heaters have reached below  $30^\circ\text{C}$ , the wind tunnel velocity can be set to zero.
24. Now both Labview programs can be stopped.

25. The Streamline program can be stopped and closed. Once the program has been closed, the Streamline box can be switched off. Also the SCXI system can be switched off.
26. Turn off the Ascroft & Jenco Control Box.
27. Turn off wind tunnel power box (flip the switch to off).
28. Close the gate to the outside and then secure the pin back through the chain.

## Chapter 3

### Validation and Uncertainty Analysis

#### **3 Introduction**

This chapter begins with an introduction to vortex promoters and will help to clarify some of the different types of tests being performed. Then validating the experiment will be presented. The results shown here will be compared with the results that have been published in the literature. Then finally this chapter will close with a discussion on uncertainty analysis and the results from the uncertainty tests will be presented for both the velocity and heat transfer rate measurements.

#### **3.1 Introduction of Vortex Promoters**

Advancements in technology and increase in demand for faster and more reliable systems have caused higher power densities and smaller packaging of electronics. However, proper thermal management is still one of the major obstacles that we must get around. In order for us to satisfy the increasing demands for high speed systems and data acquisition, inexpensive and compact thermal management solutions must be made. One

such solution would be to insert a solid body into the flow, thus changing the flow characteristics. Using a vortex promoter is considered to be one of the passive enhancement techniques, which helps to increase the heat removal rate from the various components. Vortex shedding from a cylinder has been investigated by many researchers [29]-[33]. Lo et al. [29] investigated detached-eddy simulation over square and circular cylinders for Reynolds numbers between  $1.4 \times 10^5$  and  $3.6 \times 10^6$ . A numerical study performed by Davis et al. [30] on vortex shedding from rectangular cylinders showed the two-dimensional time dependant flow around the cylinder. Laminar and turbulent flows were numerically simulated around rectangular cylinders. It showed interactions between the wake and the separation bubbles and some discrepancy between the turbulence model and the experiment [31]. Two-dimensional and three-dimensional models of transitional flow past a square cylinder were numerically investigated. RMS values for the two-dimensional flow were higher than the one for the three-dimensional flow, even though the mean flow remained unchanged [32]. Kelkar et al. [33] used a two-dimensional flow around a square cylinder to numerically predict the vortex shedding and to determine where the onset of unsteadiness occurred.

Igarashi et al. [34] investigated the fluid flow and heat transfer from rectangular cylinders. The cylinders were heated under a constant heat flux. P. Teertstra et al. [35] proposed a new technique for investigating conjugate heat transfer for air-cooled electronics. This new technique provides direct measurement of heat flow rates for two different paths: convection at the package cap and conduction into the board. Fins were used to enhance the heat transfer rate from the substrates.

Launder and Kato [36] investigated flow-induced oscillations in turbulent flow around a square cylinder are modeled using the finite volume method. The modeling was done to see how the flow would behave if it was flowing around a vertical support column for a suspension bridge. Nomura et al. [37] experimentally investigated the aerodynamic forces on a square cylinder in an oscillating flow with non-zero mean velocity.

Nakamura et al. [38] experimentally investigated the effects of turbulence on the mean flow past two-dimensional rectangular cylinders. They found that small scale turbulence increases the growth of separated shear layers and that large scale turbulence weakens regular vortex shedding. Transition and chaos in a two-dimensional flow past a square cylinder has been numerically investigated [39]. Large-Eddy Simulation (LES) was used to help reproduce the flow past a two-dimensional rectangular cylinder in a homogeneous turbulent flow [40]. Huot et al. [43] experimentally analyzed the pressure field that is induced on a square cylinder by a turbulent flow. They studied the mean and fluctuating pressure field that developed on the surface of the square cylinder in a homogeneous flow under different intensities.

The flow past a square cylinder has been experimentally investigated at high Reynolds number in order to map the near wake of the cylinder and compare with numerical results. Biswas et al, also measured the two-components of velocity in the wake using a hot-wire system [41]. Okajima [42] simulated the flow around a rectangular cylinder numerically. For low Reynolds numbers, the Finite-Difference Method (FDM) was used and for high Reynolds numbers, the Discrete Vortex Method (DVM) was used.

These two methods were used in order to find out what the characteristics of the flow were. Now we will be moving on to the next section, where the experimental results will be validated by comparing the results from Okajima's paper [44] and the results collected from the experiment.

### 3.2 Validation

In this section, the results presented in [44] with the results taken from the experimental setup are considered. This will help to verify the accuracy of the current experimental setup. For validation, only the square cylinder is present in the flow. Taking the results found by Okajima, the Reynolds number,  $Re$ , is  $2.0 \times 10^4$  and the Strouhal number,  $St$ , is 0.13.

By collecting the final information needed to verify, the results collected from the present experiment and the results in the paper are compared. In order to get close to the proper Strouhal number, most of the conditions had to remain the same, mainly the Reynolds number. By using the hot-wire anemometer, we were able to get the fluctuation in the velocity recorded behind the vortex promoter. Then by doing a Fast Fourier Transform (FFT) to the fluctuating velocities, we were then able to get the dominant frequency of the flow. Figure 3.1 shows the plot of the frequency versus the power. From this graph we were able to get the frequency for maximum power and use it to compute the Strouhal number, which is based on the frequency multiplied by the height of the promoter and divided by the free-stream velocity.



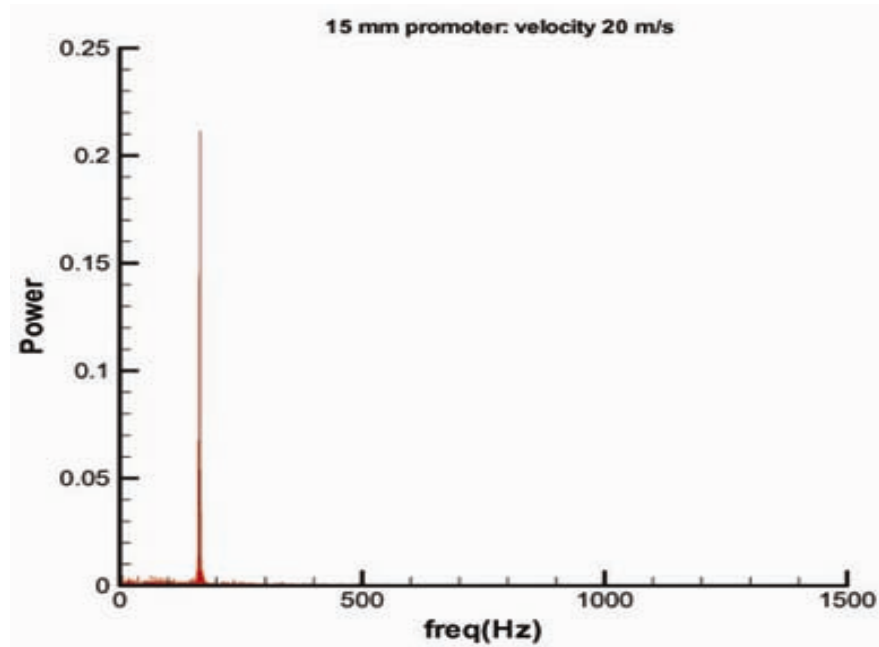


**Figure 3.1: Relationship between Frequency and Power from FFT**

From the graph we were able to conclude that the frequency for this flow and promoter is 165 Hz. Now that the frequency and the height of the promoter,  $h_p=15$  mm, are known, the Strouhal number for a free-stream velocity of 20 m/s can be calculated. After doing the computation, the Strouhal number for the experiment came out to be  $St = 0.124$  for a Reynolds number  $Re = 2.0 \times 10^4$ .

Comparing the Strouhal number from Okajima's paper,  $St = 0.13$  and the Strouhal number from the present experiment,  $St = 0.124$ , the two numbers are relatively close. Then by computing the percent error, based on these two numbers, it was determined that the results from the experiment were less than 5 % from the published results. From these

results it can conclude that the experimental setup is good and that the results are among the values obtained earlier.

### 3.3 Uncertainty Analysis

In order for an experiment to be accepted, it must be able to be repeated. With repeatability comes uncertainty which is based on the measurements. No experiment is considered to be complete without some kind of uncertainty or error analysis to prove that the results are accurate. The source of error in the measurements is broken down into three separate categories [45]:

1. Calibration error ( $e_1$ )
2. Data acquisition error ( $e_2$ )
3. Data reduction error ( $e_3$ )

Calibration errors cannot be eliminated totally, but they can be reduced down to acceptable values. Data acquisition errors arise during the actual act of measuring. These help to contribute to the accuracy and the resolution of the instrument. Data reduction errors are associated with the statistical analysis of the data, mainly dealing with curve fits and correlations. An estimate of the total uncertainty in the measurement of the parameter,  $u_x$ , can be calculated by using the three sources of error listed above and by using the root-sum squares method [45]:

$$u_x = \sqrt{e_1^2 + e_2^2 + e_3^2} \quad (3.1)$$

If there are multiple elements (sources of error) affecting the three major categories of error, the total uncertainty for that particular source of error can also be calculated by the root-sum squares method. That is, if there are  $m$  elements contributing to one of the three types of error,  $e_i$ , can be approximated by:

$$e_i = \sqrt{e_{i1}^2 + e_{i2}^2 + e_{i3}^2 + \dots + e_{im}^2} \quad (3.2)$$

Once all the total uncertainties for the measured data are calculated, we can now compute the propagation of error to the results. Then  $f(x_1, x_2, \dots, x_m)$  can be calculated by using the following equation:

$$\pm \Delta f = \sqrt{\left(\frac{\partial f}{\partial x_1} \Delta x_1\right)^2 + \left(\frac{\partial f}{\partial x_2} \Delta x_2\right)^2 + \dots + \left(\frac{\partial f}{\partial x_m} \Delta x_m\right)^2} \quad (3.3)$$

where  $\Delta x_m$  is the uncertainty that related to the variable  $x_m$ .

### 3.3.1 Heat Transfer Rate Measurement

The heat transfer rate is measured by the use of a heat flux sensor placed below the heating strip as described in section 2.2.2. The operating range for the sensor is taken to be  $12,500 \text{ W/m}^2$ . The specifications, taken from the manufacturer, reveal a sensitivity of  $\pm 10\%$ . This contributes to the calibration or instrumental error,  $e_1$ , which we have found to be  $\pm 1,250 \text{ W/m}^2$ .

$$e_1 = \frac{10}{100} \times 12,500 \Rightarrow e_1 = \pm 1,250 \frac{\text{W}}{\text{m}^2} \quad (3.4)$$

The heat flux data from the sensors are collected for 60 seconds, which gives us a sampling frequency of 1 Hz. These 60 values are then averaged and accepted as the final value. The uncertainty, because of averaging these numbers, is shown as  $e_2$ , which can be calculated by using the 95% confidence limit times the standard deviation of the data collected. For 60 samples, the confidence limit,  $t_v$ , is given as 2.0 [45]. The maximum standard deviation of the heat flux data is observed to be  $72.63 \text{ W/m}^2$ , thus  $e_2$  is found to be  $145.26 \text{ W/m}^2$ .

$$e_2 = \pm t_v S_{\text{dev}} = \pm 2.0 \times 72.63 \frac{\text{W}}{\text{m}^2} = \pm 145.26 \frac{\text{W}}{\text{m}^2} \quad (3.5)$$

The last source of error,  $e_3$ , is due to the steady-state assumption, when the temperature difference is  $60 \pm 0.38^\circ\text{C}$ . The uncertainty in the heat transfer rate caused by making this assumption is found to be  $\pm 283.5 \text{ W/m}^2$ . The total uncertainty of the heat transfer rate measurement can then be calculated as:

$$e_{\text{tot}} = \sqrt{e_1^2 + e_2^2 + e_3^2} = \sqrt{1250^2 + 145.26^2 + 283.5^2} = \pm 1,289.95 \frac{\text{W}}{\text{m}^2} \quad (3.6)$$

Thus, the uncertainty of the heat transfer per unit length is calculated to be  $\pm 32.8 \text{ W/m}$ .

### 3.3.2 Pressure Measurement

The pressure transducer accuracy is specified by the manufacturer to be  $\pm 0.2\%$  full scale of 10 inches of water. The instrumental error,  $e_1$ , is found to be  $\pm 4.98 \text{ Pa}$ .

$$e_1 = \frac{0.2}{100} \times 10'' H_2O = 0.02'' H_2O = \pm 4.98 \text{ Pa} \quad (3.7)$$

The pressure data are collected over 60 seconds with a sampling frequency of 1 Hz. The data are then averaged to find the nominal value of the pressure. The standard deviation of the pressure data was found to be 2.03 Pa for all conditions. Thus the uncertainty due to data reduction,  $e_2$  is:

$$e_2 = t_v S_{\text{dev}} = 2 \times 2.03 = 4.06 \text{ Pa} \quad (3.8)$$

Then, the total uncertainty of the pressure measurement is computed as:

$$e_{\Delta P} = \sqrt{4.98^2 + 4.06^2} = \pm 6.43 \text{ Pa} \quad (3.9)$$

### 3.3.3 Air Velocity Measurement

The main sources found in the air velocity uncertainty are the pressure measurements, compressibility effects, Pitot tube installation and data reduction. The air velocity can be computed based on this relation:

$$U = \sqrt{\frac{2\Delta P}{\rho}} \quad (3.10)$$

The uncertainty in the air velocity measurement can then be computed by:

$$\pm \Delta U = \sqrt{\left[ \frac{\partial U}{\partial \Delta P} \Delta(\Delta P) \right]^2 + \left[ \frac{\partial U}{\partial \rho} \Delta \rho \right]^2} \quad (3.11)$$

The total uncertainty in the pressure measurement is calculated to be  $\pm 6.43$  Pa from equation 3.9. The use of the incompressible flow equations causes an error,  $e_1$ , to be between 0.3% and 0.4%. The Pitot tube misalignment contributes an error,  $e_2$ , of about 1% in pressure difference used for velocity calculation [46]. For a nominal air velocity of

16 m/s, the pressure drop,  $\Delta P$ , is 154 Pa. From this nominal value,  $e_1$  and  $e_2$  can be found as  $\pm 0.539$  Pa and  $\pm 1.54$  Pa, respectively. Thus the total uncertainty from the pressure difference is:

$$\Delta P = \sqrt{0.539^2 + 1.54^2 + 6.43^2} = \pm 6.63 \text{ Pa} \quad (3.12)$$

The uncertainty interval of the air density around a nominal value of  $1.2 \text{ kg/m}^3$  can be assumed as  $\pm 0.06 \text{ kg/m}^3$ . The total uncertainty of the air velocity measurement using equation 3.11 is calculated to be  $\pm 0.53 \text{ m/s}$ .

The consistency and repeatability of the experiments are tested by running the experiment three times at the same operating conditions. The heat transfer results, as shown in figure 3.2, reveal that the maximum difference in the heat transfer rate is less than 10%.

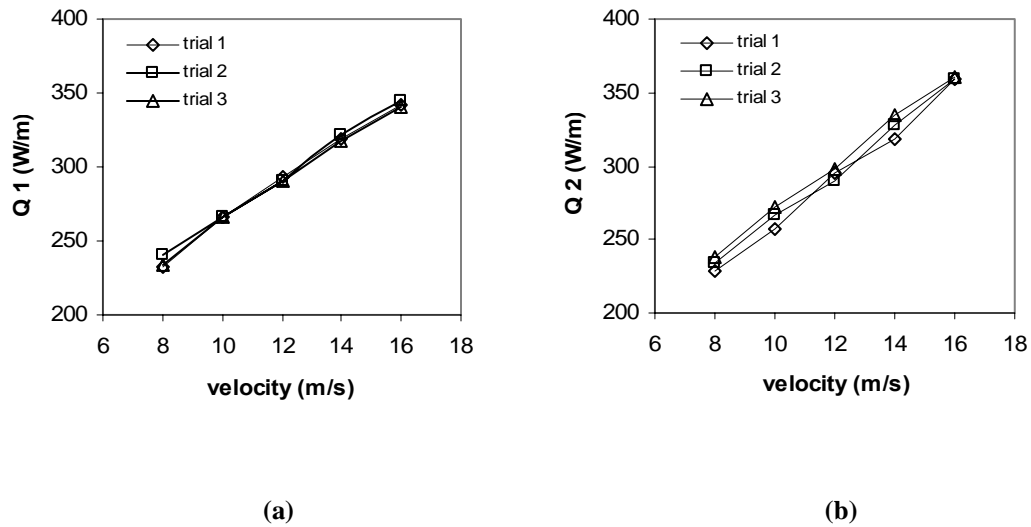


**Figure 3.2 : Repeatability and consistency of experiments without a promoter**

## Chapter 4

### Results and Discussion

#### **4 Introduction**

In this chapter, the results will be divided into four different sections. In the first section, only the vortex promoter is considered. Next only the plate is discussed. In the third part, the vortex promoter and the plate are combined to see the effects the vortex promoter has on the plate. Then in the final section, pictures of the visualization of the flow, by using a smoke generator, are presented to show how each promoter affects the flow.

#### **4.1 Results for Vortex Promoters Only in the Flow**

This section will show the effects that just the promoter has on the flow. In figure 4.1, we show the vertical positions of a hotwire. The promoter that is used here is the large promoter, which has a height,  $h_p$ , equal to 25.4 mm and is taken at a downstream position of  $x/h_p = 2$ . This graph compares the frequency at different Reynolds numbers,

which is based on the height of the promoter. Each position, as described as upper, center and lower, means that the upper and lower positions were 25.4 mm above and below the centerline of the promoter. From the graph, we can see that the frequency does not change if the hotwire is at any of the three positions. This shows that the frequency does not vary based on the vertical position of the hotwire.

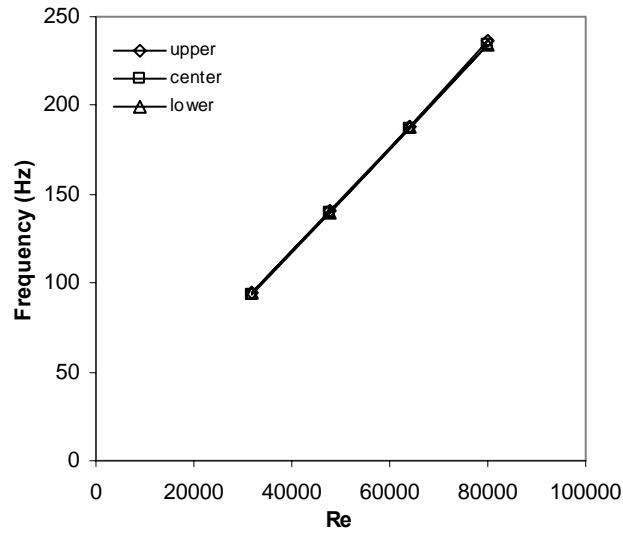


**Figure 4.1: Vertical Positioning of hotwire**

Now that the frequency does not change in the vertical position, tests in the horizontal direction have to be made to see if there are any changes. In figure 4.2, the left, right and center positions of the hotwire along the vortex promoter are considered. The vortex promoter used in this test, has a height,  $h_p$  equal to 15 mm and data is taken from the hotwire probe downstream at  $x/h_p = 2$ . By looking at the graph, the frequency does not change for each of the horizontal positions. From this it can be concluded that the oscillations coming off the promoter are the same across the vortex promoter.



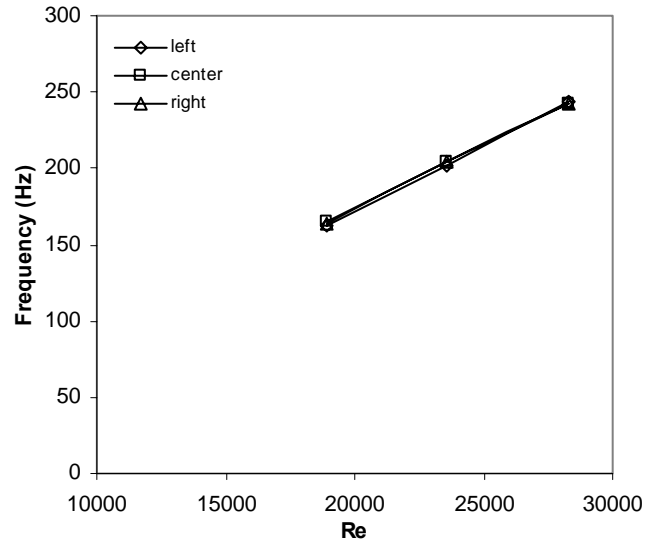
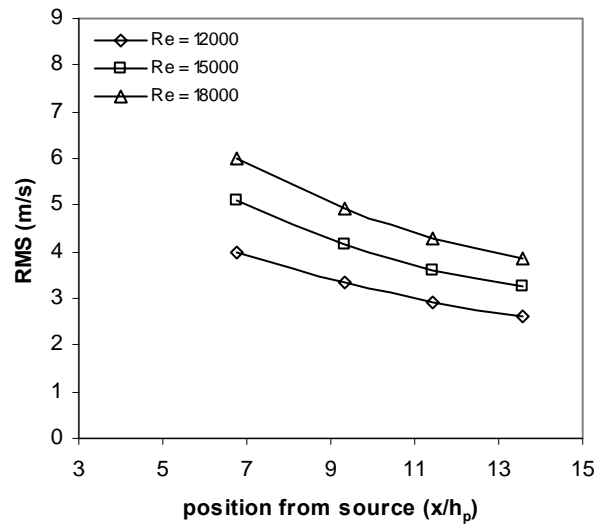


**Figure 4.2: Horizontal Positioning of hotwire**

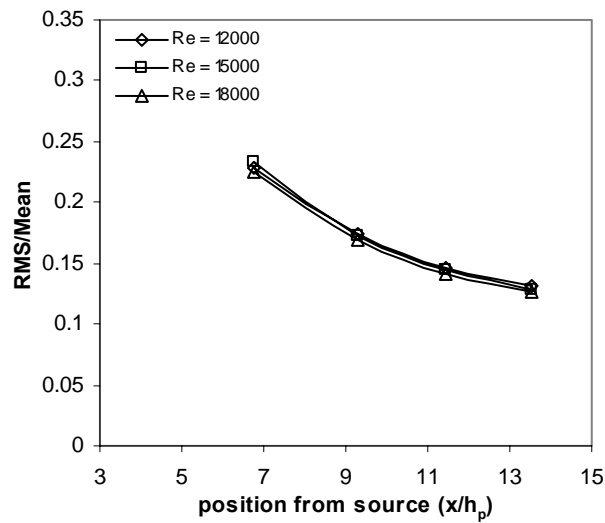
Since now it is known that the oscillations or frequency will not change with vertical or horizontal positions, the Root-Mean-Square or RMS of the velocity can be discussed. As seen in figure 4.3a, the separation distance causes some changes in the RMS value. As the separation distance between the vortex promoter and the hotwire increases, the RMS of the velocity decreases. In figure 4.3b, the non-dimensional velocity is shown. This also shows that at some given speed, the disturbance decreases the farther it moves away from the promoter.

The next couple graphs will focus on using the large promoter, ( $h_p = 25.4$  mm) and will show the effects on the frequency and Strouhal number at different positions away from the vortex promoter. Figure 4.4 shows how the frequency is affected at a separation distance of 2 and 7.5 for different Reynolds numbers. These two separation distances are shown together because of there being no change in the frequency at each velocity. The result is as expected, because as the Reynolds increases, so does the

frequency. Figure 4.5 is at the same separation distance, but shows the affect of the Strouhal number at different Reynolds number. The Strouhal number, for the most part, stays constant, because the frequency and velocity are increasing at the same rate.



(a)



(b)

Figure 4.3: Different positions from 15 mm promoter for (a) RMS of Velocity, (b) RMS / Mean

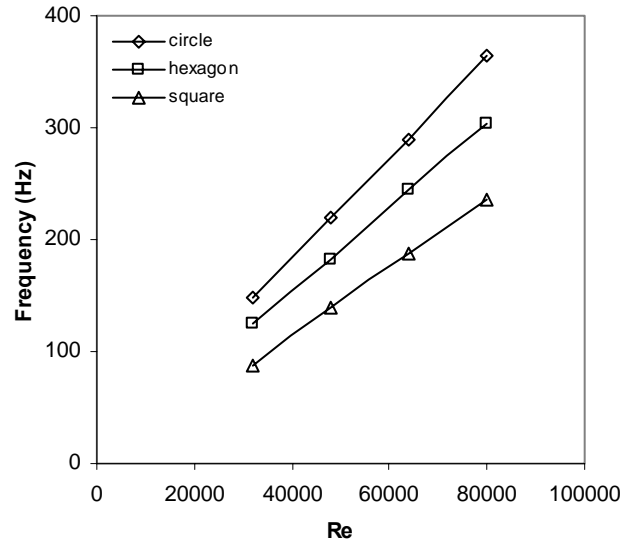


**Figure 4.4: Large Promoter Frequency at  $x/h_p = 2$  and  $x/h_p = 7.5$**

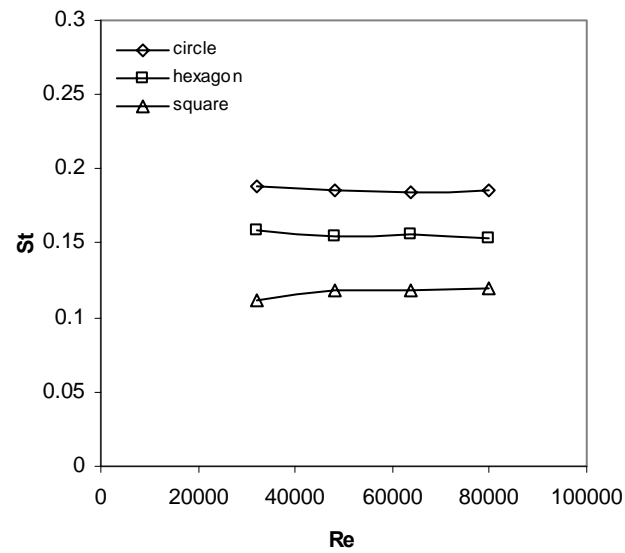


**Figure 4.5: Large Promoter Strouhal number at  $x/h_p = 2$  and  $x/h_p = 7.5$**

The values for the frequency and Strouhal number do not change as you move farther away from the vortex promoter, but the RMS of the disturbance values do. In figure 4.6,

the difference between the RMS values do not change much. The values are in a close packed bunch. This is because at such a close distance, the promoter is acting more as a blocker than an enhancer. Figure 4.7, shows basically the same thing as figure 4.6, but it is at a different separation distance. Since it is farther away from the vortex promoter, there will be a smaller amount of oscillations coming from the promoter than there would be at  $x/h_p = 2$ . These two plots, basically confirm what we had found for the 15 mm vortex promoter. As the hotwire moves away from the vortex promoter, the less the amount of oscillations there will be in the flow. From what is seen here, the square and hexagon size promoter seems to give a somewhat larger disturbance than circle promoter because the sharp corners provide stronger and longer lasting vortices. We will see later as to how that will affect the heat transfer.

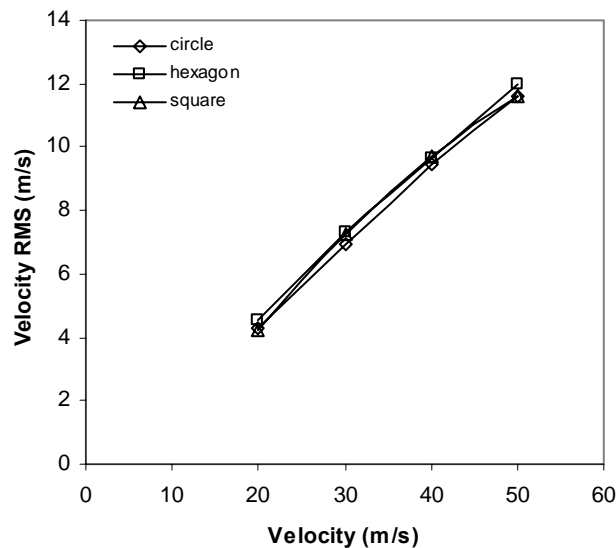


**Figure 4.6: RMS of Velocity at  $x/h_p = 2$**

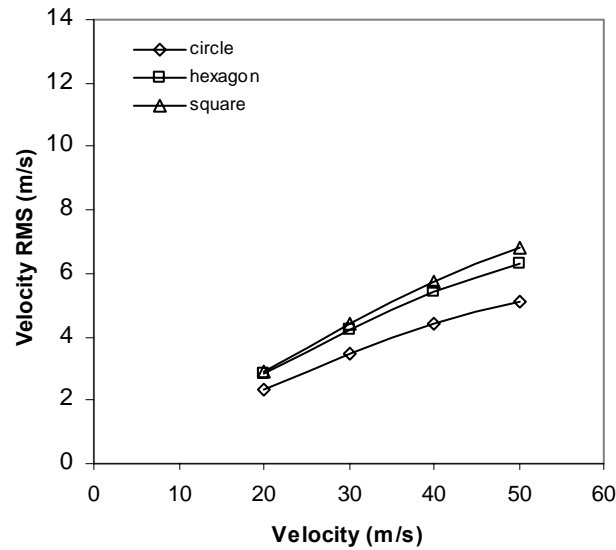


**Figure 4.7: RMS of Velocity at  $x/h_p = 7.5$**

Now how the frequency and Strouhal numbers change with increasing separation between the hotwire probe and the vortex promoter will be presented. As seen in figure 4.8, the plot shows how the frequency changes with separation distance. None of the frequencies change drastically with separation distance, which is to be expected. Figure 4.9, basically has the same pattern as figure 4.8, but is dealing with the Strouhal number. However, if you compare figures 4.5 and 4.9, you will see that the Strouhal numbers are very close to one another. This relation helps to prove that if the Strouhal number is staying constant for the most part, this would indicate that the frequency and the free stream velocity are changing at the same rate. This would then allow the Strouhal number to stay constant.

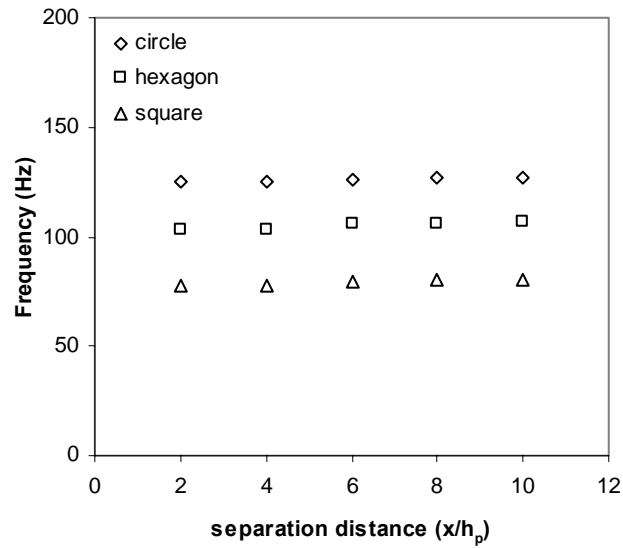


**Figure 4.8: Large Promoter Frequency for different separation distances**

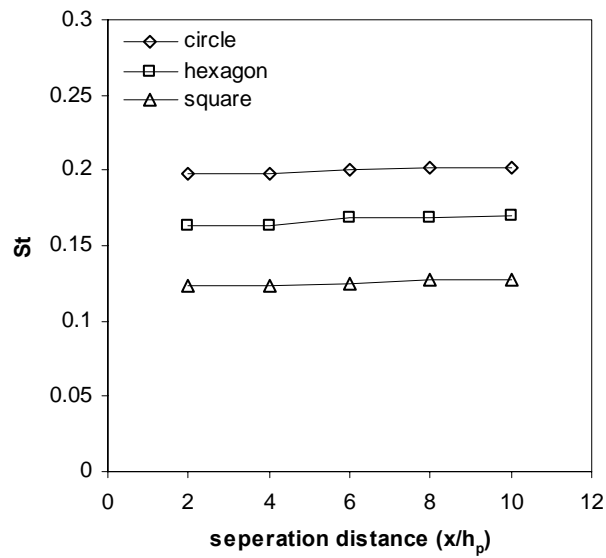


**Figure 4.9: Strouhal number for large promoters for different separation distances**

The next two graphs, which will be based on results obtained by using the Pitot tube instead of the hotwire system. In the first graph, figure 4.10, we will be looking at is the relation between the velocity recorded and what the velocity should be. The Pitot tube

is placed in the center of the promoter at a distance of  $x/h_p = 2$ . We can see that when there was no promoter placed in front of the Pitot tube, it shows an almost linear relationship. Then as we start using the promoters, the velocity goes down slightly compared to the hexagon and the square. The square seems to be causing more of a blocking effect for the flow than being used to enhance the flow or by making it more chaotic. The next graph, shown in figure 4.11, describes the RMS of the disturbance that the Pitot tube senses for the different promoters. Based on the results shown, the hexagon promoter seems to cause the greatest amount of disturbance and then followed by the square promoter. By looking at the graph, it seems that the square and hexagon promoter act the same way because they both jump at the same spot. The circle however, does not show that much of a disturbance, as compared to the other two. Next we will be moving on to how only the plate can affect the flow and how the heat is taken away without a vortex promoter in front.

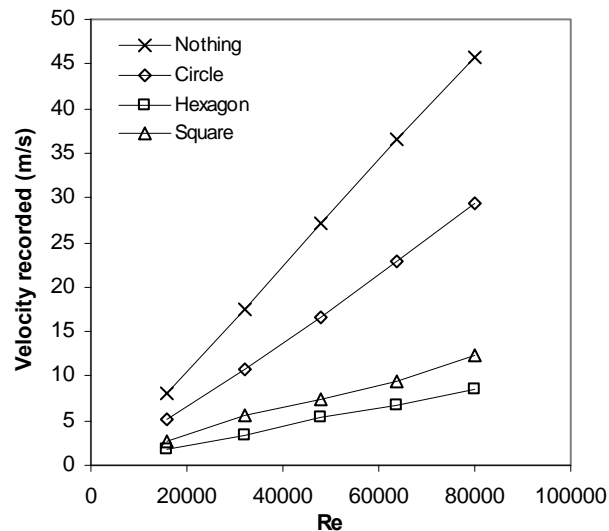


**Figure 4.10: Comparison between estimated and recorded velocity by Pitot tube**

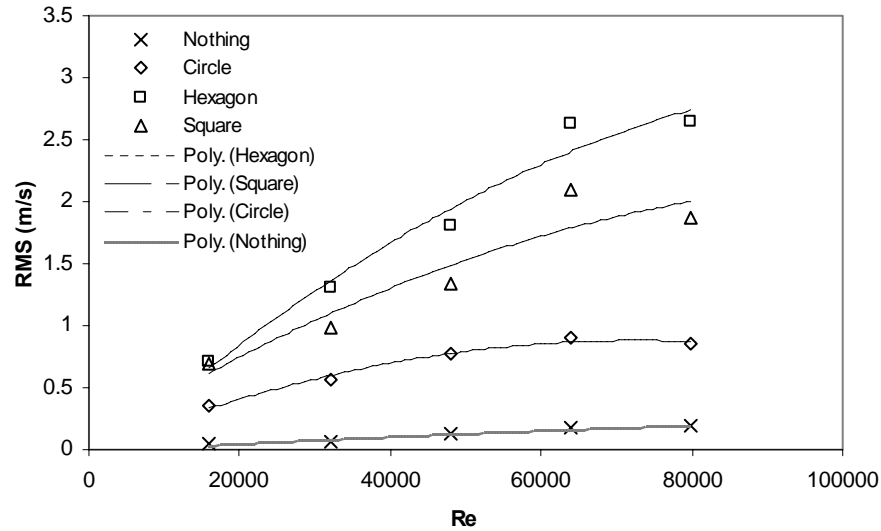
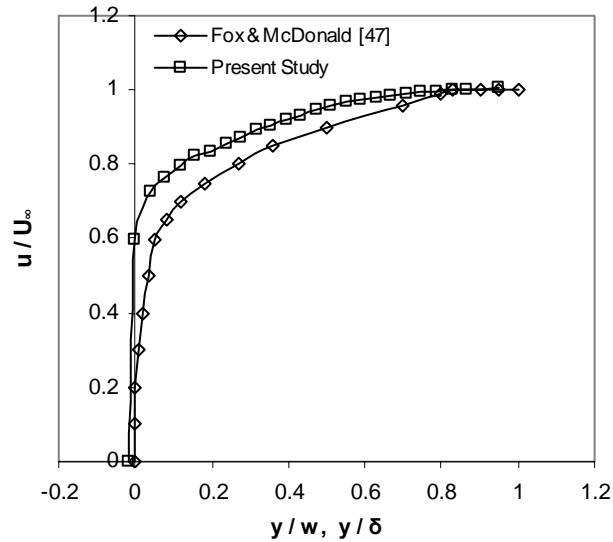


Figure 4.11: RMS of disturbance by Pitot tube

## 4.2 Results for Plate Flow Only

In this section, the focus will be on the results from just the plate flow. From this we will be able to get base cases for just the flow over the plate and the heat transfer analysis without a vortex promoter. The first thing that will be discussed in this section is the boundary layer graph and its profile. The boundary layer curve is shown in figure 4.12. The free stream velocity was measured to be 10.2 m/s and the theoretical result was taken from a fluid mechanics textbook **Error! Reference source not found.** From looking at the plot, the experimental boundary layer matches up well with the published result. This plot confirms that the boundary layer flow occurs in the turbulent region.





**Figure 4.12: Boundary Layer Profile**

The heat transfer analysis for the plate will now be discussed. The heat transfer analysis found in the remainder of the thesis is based the difference between what the heaters are producing and the output felt by the heat flux sensor. This amount that is left is the heat that is transferred into the ambient air. The first group of graphs that will be discussed are the heat transfer rate plots. Figure 4.13 describes how  $Q_1$  behaves with the changing velocity. As we can see from the graph, the changing positions do not really affect  $Q_1$  at all because the separation distance,  $d$ , is based on the distance between the first and second heat source. The only way the heat transfer rates do not seem to match up perfectly with each other is because of the slight change in velocity from the wind tunnel. In figure 4.14, the graph shows how the second heat source,  $Q_2$  behaves for different separation distance,  $d$ , and the different velocities. By looking at the graph, we can see that the farther away from the first heat source, the better the heat transfer rate is. This is because of the first heat source,  $Q_1$ , is putting a lot of heat and energy in to the air. This

causes the air temperature to rise locally. As the velocity is increased, the increased air temperature moves farther down the plate. This cuts back on the amount of heat that is transferred to the air by the second heat source,  $Q_2$ . So by separating the heaters by at least two widths of the heater, we can increase the amount of heat transferred to the air by the second heat source.

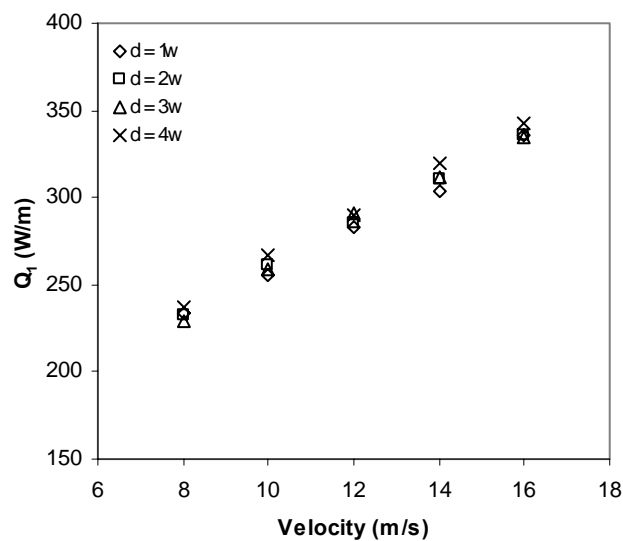


**Figure 4.13: Heat Transfer rate for the first heater**

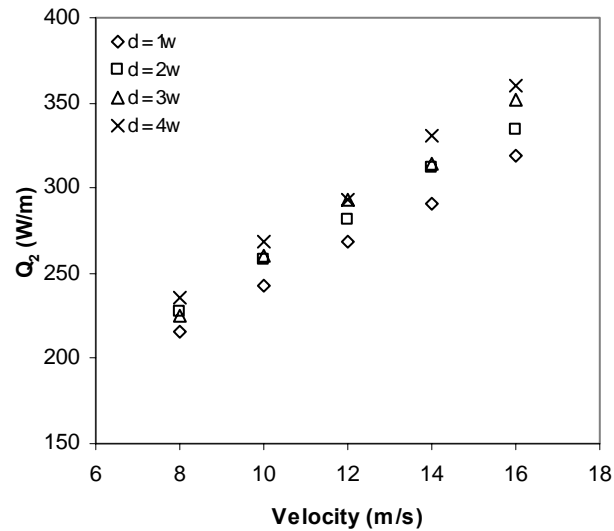


**Figure 4.14: Heat Transfer Rate for the second heater**

The next group of graphs that will be discussed are the heat transfer coefficient and how it is affected by the flow. Figures 4.15 and 4.16, describe the effects the flow and the separation distance,  $d$ , has on the heat transfer coefficient. By looking at the first graph, 4.15, we see that the separation distance does not have an effect on the heat transfer coefficient. This is expected, because as described before, the first heater does not move. Only the second heat source moves the separation distances away from the first heat source. Figure 4.16, however shows a little more vertical separation between the distances as you increase velocity as compared to the second heat transfer rate. This plot also confirms that the farther away the separation between the heaters, the better heat transfer you will have.

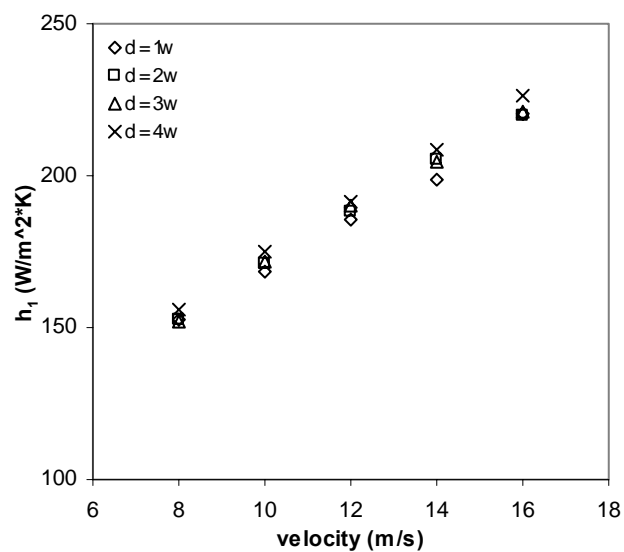


Figure 4.15: Heat Transfer Coefficient for first heater

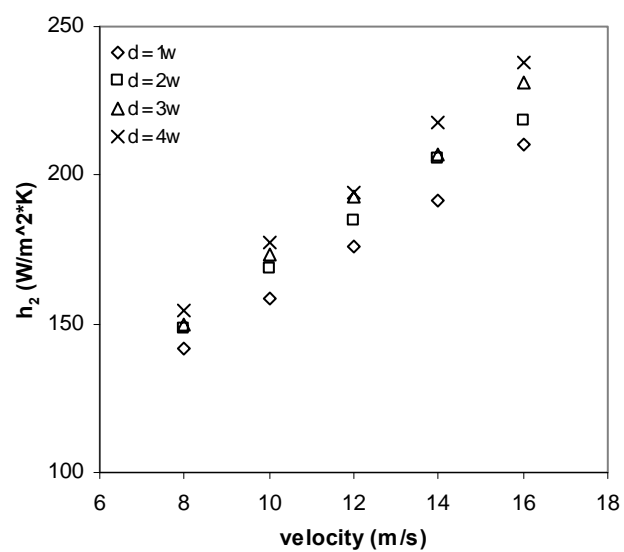
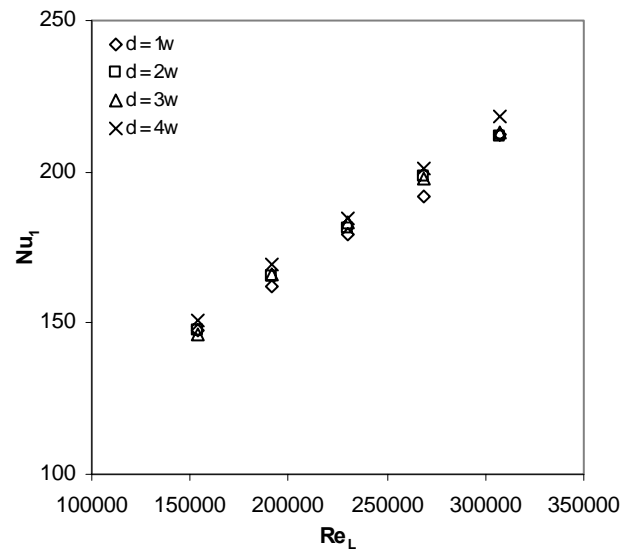
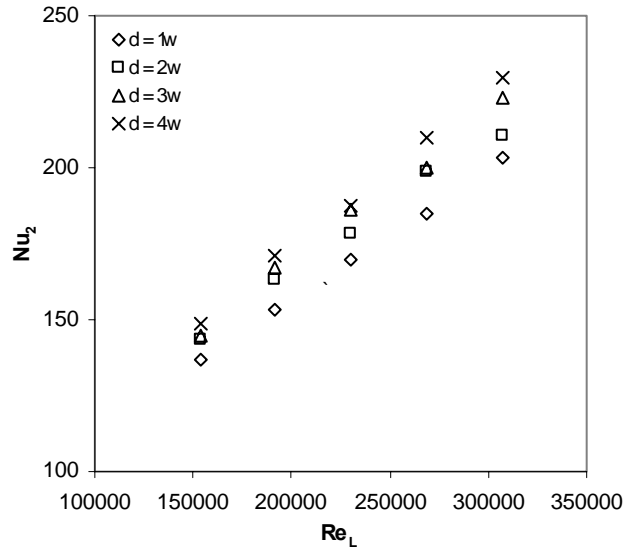


Figure 4.16: Heat Transfer Coefficient for second heater

We have shown the results for the heat transfer rate and the heat transfer coefficient, so now we will convert the heat transfer coefficient into the Nusselt number and present it in terms of the Reynolds number based on the plate length. The general outline of these next two graphs, figure 4.17 and 4.18, will be the same as the previous two, just that the magnitudes will be slightly less. They also follow the same reasoning as before, just that the second heater moves while the first one stays fixed. By showing these graphs, we now have a good idea as to how the heat transfer reacts for just the plate being in the flow.



**Figure 4.17: Nusselt number for first heater**



**Figure 4.18: Nusselt number for second heater**

The last part that will be discussed in this section is the comparison of  $Q_1$ ,  $Q_2$  and  $Nu_1$ ,  $Nu_2$ . We will be doing this to see the changes in the heat transfer rate as well the changes in the Nusselt numbers. Both of these plots had the wind tunnel running at 16 m/s. In figure 4.19, the comparison between  $Q_1$  and  $Q_2$  is shown. From the figure, we can see that  $Q_1$  changes slightly with the non-dimensional separation distance, but  $Q_2$  seems to increase with increasing non-dimensional separation distance. In figure 4.20, the same can be said for the  $Nu_1$  and the  $Nu_2$  plots. They seem to behave the same way that  $Q_1$  and  $Q_2$  do. These two plots seem to confirm what was already shown, that as the separation distance increases, the heat transfer rate also increases. This means that when the sources are close together, the air temperature is raised and thus causes the heat transfer to be less, because the air is warmer than it was before.

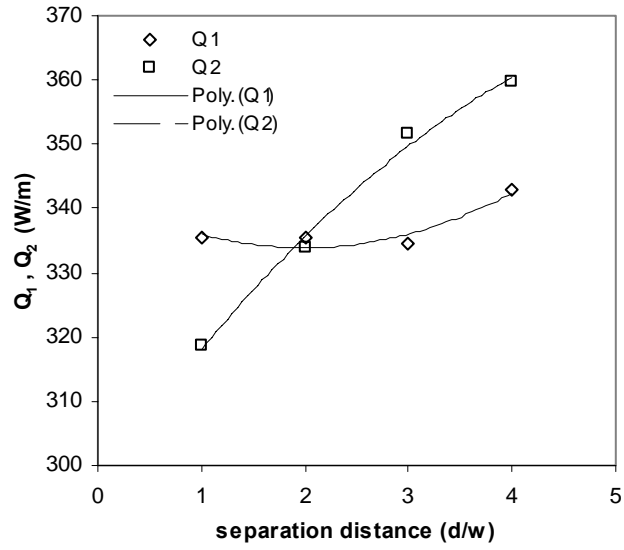


Figure 4.19: Comparison of  $Q_1$  and  $Q_2$  at  $16\text{ m/s}$

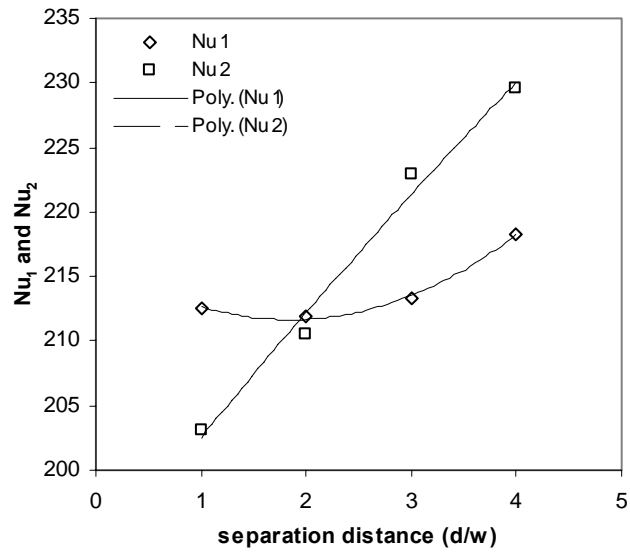


Figure 4.20: Comparison of  $Nu_1$  and  $Nu_2$  for  $16\text{ m/s}$

### 4.3 Combination of Vortex Promoter and Plate

In this section we will be combining the previous two cases and seeing what kind of effects will arise. The first thing that we will be discussing in this section is the temperature profile. The temperature profile is taken without a vortex promoter in the flow and with a vortex promoter in the flow. The temperature profile is broken up into two parts. The first part, as shown in figure 4.21, displays the effects of placing the probe in between the first and second heater and after the second heater. From this graph, we can see that after the second heater, there is a higher temperature than compared with the ones in between the first and the second heater. The graph also shows that for these cases, the promoter acted more as a blocking tool than enhancing the flow.

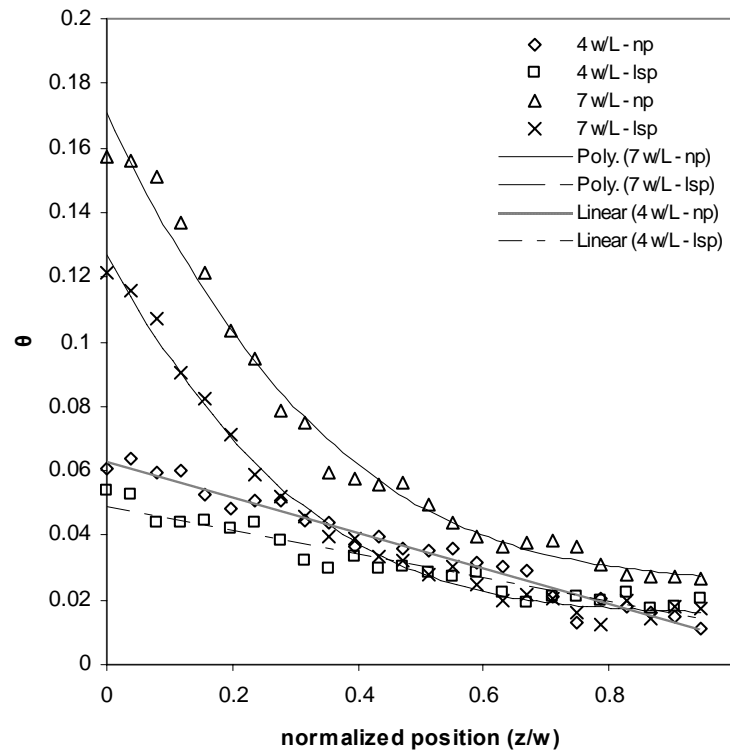
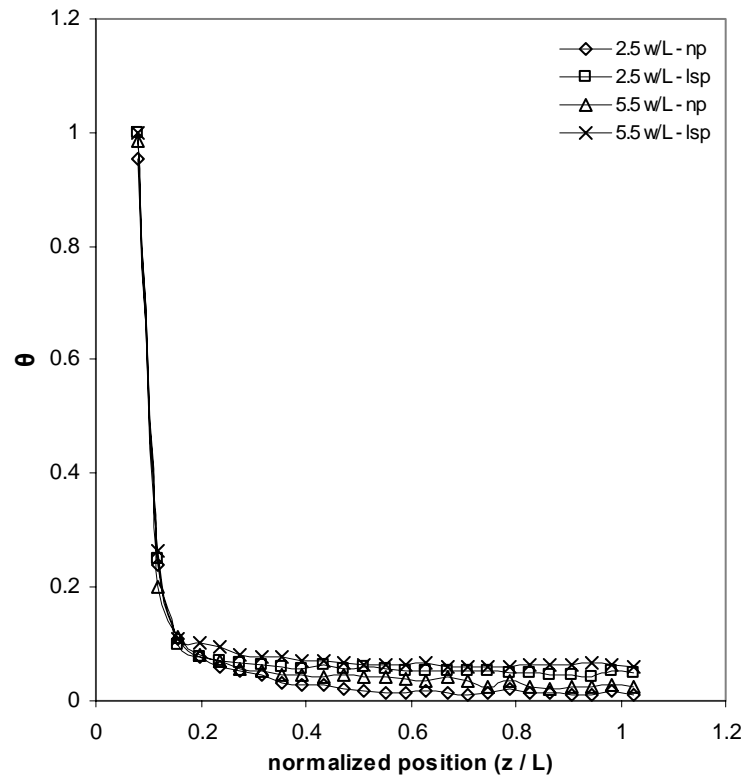


Figure 4.21: Temperature profiles

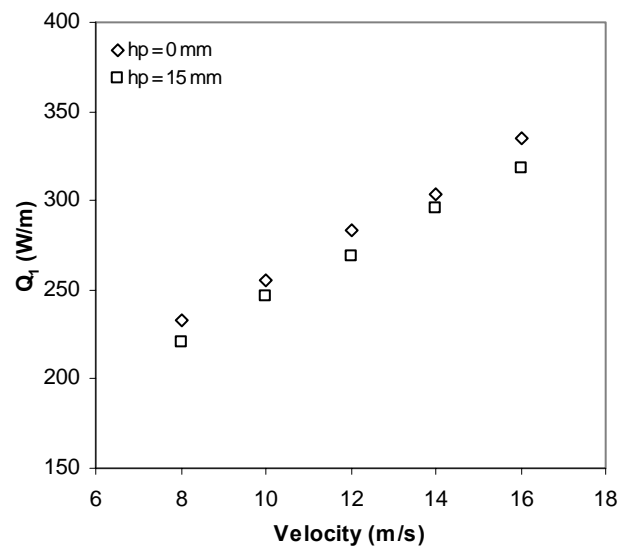


In the second part of the temperature profile, we look at the profile located on top of the first and second heaters, as shown in figure 4.22. From the plot, we can see that as the probe moved up and away from the heaters, the temperature continued to drop until it reached the ambient temperature. It also seems that when the promoter was in place, the heaters were able to reach a slightly higher temperature, as compared to the readings from no promoter.

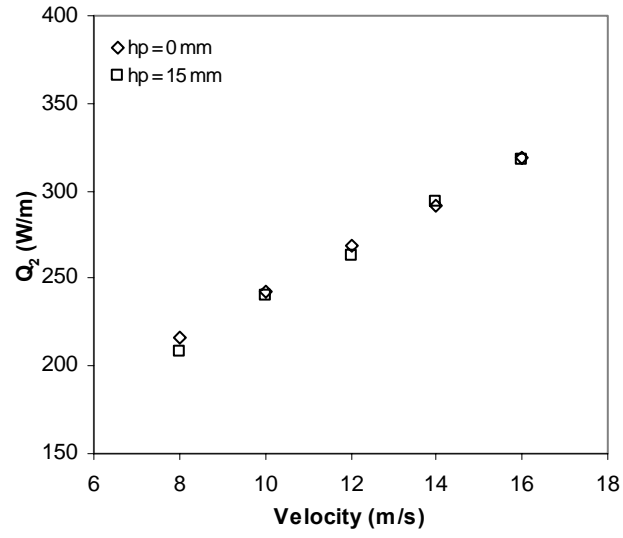


**Figure 4.22: Temperature profiles on top of first and second heaters**

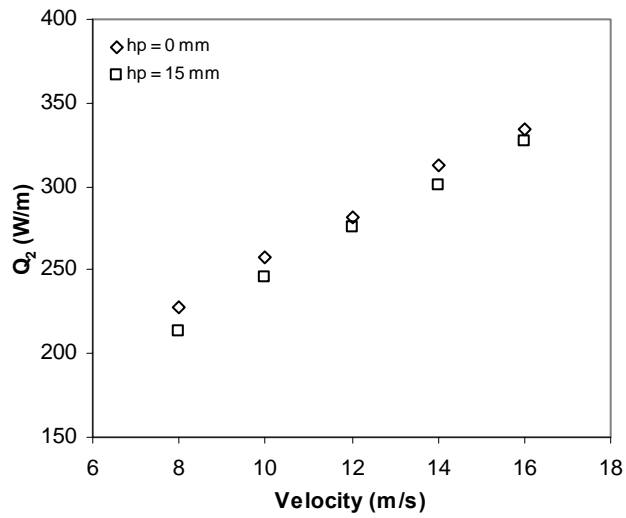
The first set of results that we will be discussing, are the results from the 15 mm promoter. We will only be showing the results of the 15 mm promoter for separation distances of  $1w$  and  $2w$ . The other two separation distances will be shown in the appendix. In figure 4.23, the three graphs are showing the heat transfer rates for the first and second heaters at a separation distance of  $1w$  and  $2w$ . From looking at the graphs, we can see that the 15 mm promoter caused more of a blocking effect than an enhancement effect. Both the heat transfer rates for the first heater and the second heater are less for the vortex promoter than if there was nothing there. The only time that most of the values of the heat transfer rate are close together is when the separation distance is  $1w$ . For the rest of the heat transfer rates, there is a distinct difference between having a vortex promoter in the flow and having nothing in the flow.



(a)



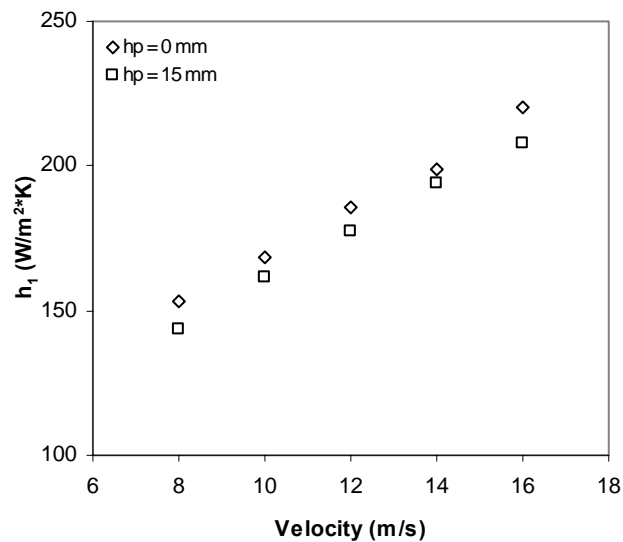
(b)



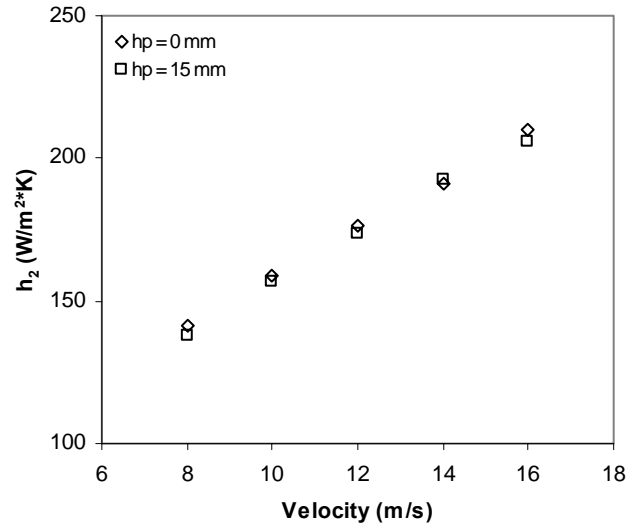
(c)

Figure 4.23: Heat transfer rates for 15 mm promoter (a)  $Q_1$ ,  $d/w = 1$ , (b)  $Q_2$ ,  $d/w = 1$ , (c)  $Q_2$ ,  $d/w = 2$

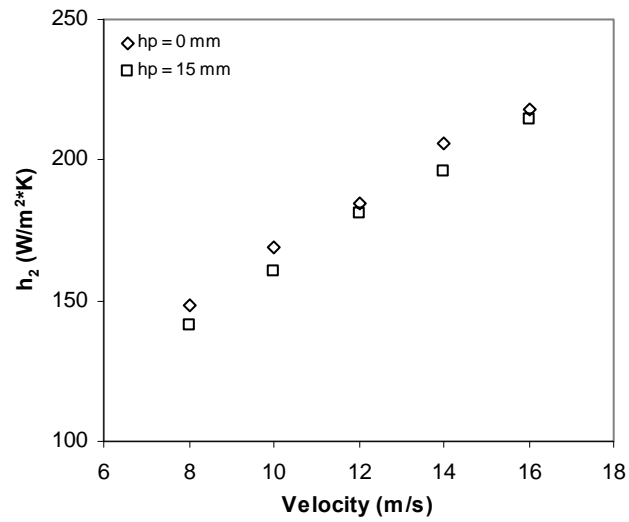
The heat transfer coefficient for the 15 mm promoter will now be discussed and how it compares to nothing being in the flow. From looking at figure 4.24, we can see that the heat transfer coefficient acts in just about the same way as the heat transfer rate does. The magnitudes would be slightly smaller, but overall follow the same pattern. The pattern is that for a separation distance of  $1w$ , we see that the values for both cases are on top of each other or close to it. Then as the second heater is moved away from the first heater, the distance between the two cases gets larger. This is happening because the first heat source is adding a little heat to the air and is not raising the temperature of the air that much, which is helping the second heat source. Then as the second heat source is moved farther and farther away from the first heat source, the less of an impact the first heat source has on the second heat source and the first heat source has the time to heat up the air a lot more. So the second heat source does not output as much heat as it would because the air is warmer than before.



(a)



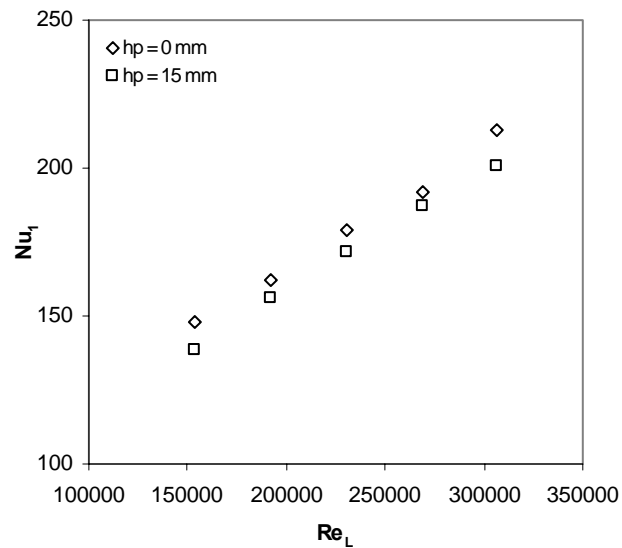
(b)



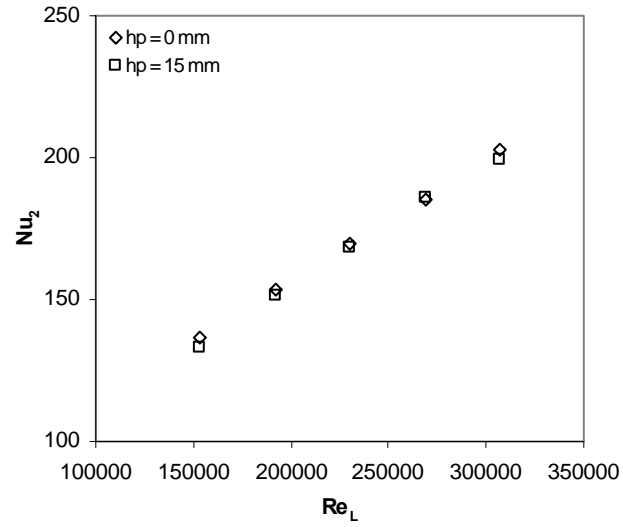
(c)

**Figure 4.24: Heat transfer coefficients for 15 mm promoter (a)  $h_1$ ,  $d/w = 1$ , (b)  $h_2$ ,  $d/w = 1$ , (c)  $h_2$ ,  $d/w = 2$**

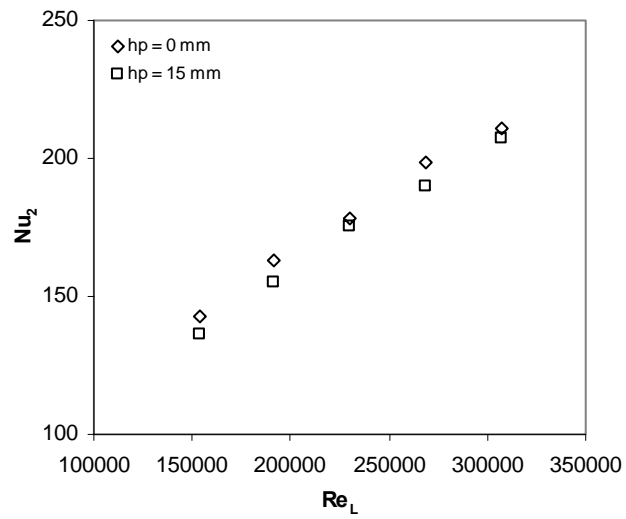
The last part has to deal with the 15 mm promoter. This part discusses how the Nusselt number is affected when there is a vortex promoter in the flow and when there is nothing in the flow. By looking at figure 4.25, we can see how the Nusselt number is affected by there being a vortex promoter in the flow and if there is nothing there. The values for the Nusselt number also follow the same pattern as the heat transfer coefficient, which is what we expected. From these plots we see that for the first separation distance,  $1w$ , that most of the values overlap, just like the heat transfer coefficient did. Then the farther the second heat source was moved away from the first heat source, the larger the difference between the two cases seemed to become more noticeable. This result follows with what we had got from the heat transfer coefficient.



(a)



(b)



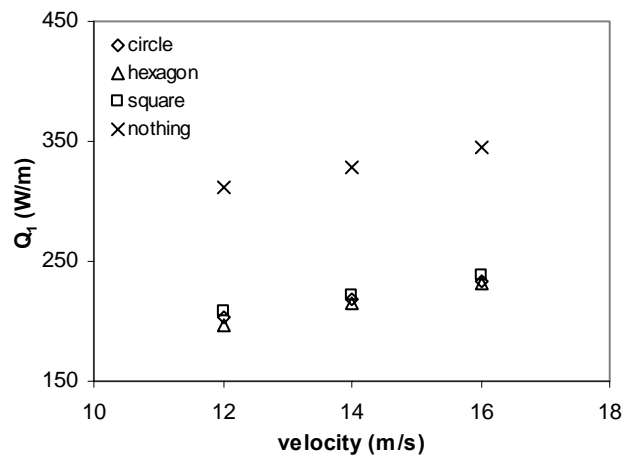
(c)

Figure 4.25: Nusselt number for 15 mm promoter (a)  $Nu_1$ ,  $d/w = 1$ , (b)  $Nu_2$ ,  $d/w = 1$ , (c)  $Nu_2$ ,  $d/w = 2$

Now we will move on our discussion to the larger promoters of  $h_p = 25.4$  mm.

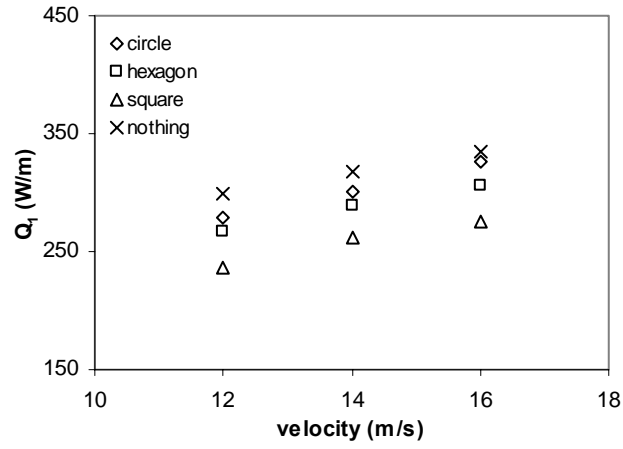
The intent of this part is to see how the heat transfer rate is affected by changing the plate separation distance,  $D$ , from the vortex promoter. This part is broken down into 4 parts.

The first and second parts will deal with the heat transfer rates of the first heat source and the second heat source respectively. The third and fourth parts will deal with the heat transfer coefficient for the first heat source and the second heat source respectively. In the first part, shown in figure 4.26, when comparing  $Q_1$  for the 3 promoters and also for nothing there, we can see how it is affected. From these 3 graphs, we can see that for all plate separation distances, nothing there seems to provide a higher heat transfer rate. This result is what we had expected to see happen. For all the promoters, they caused a blocking effect and did not allow the air flow to come back down on top of the heaters. Instead, it forced the air back up and did not start to come back down till the tail end of the plate.

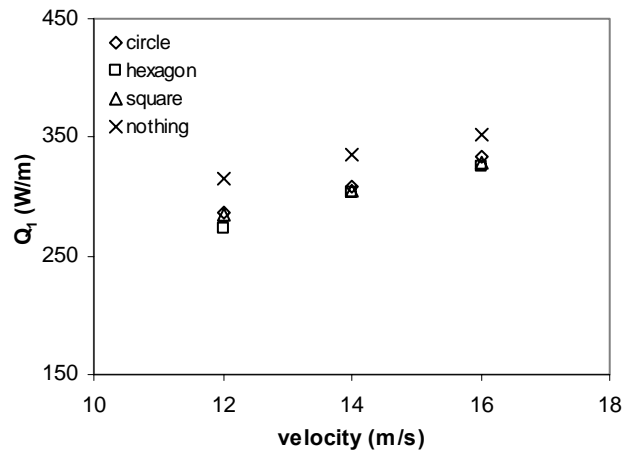


(a)





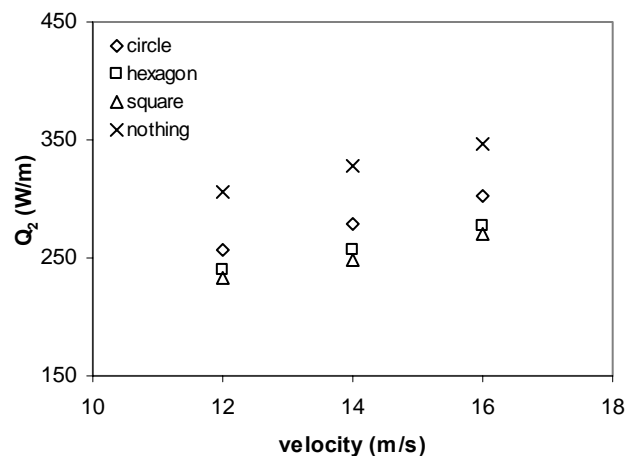
(b)



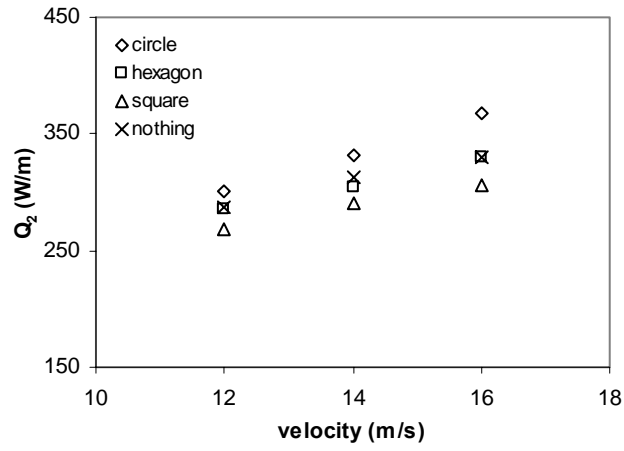
(c)

Figure 4.26: Heat transfer rates for the first heat source for different plate separations (a)  $D/w = 0$ , (b)  $D/w = 3$ , (c)  $D/w = 5$

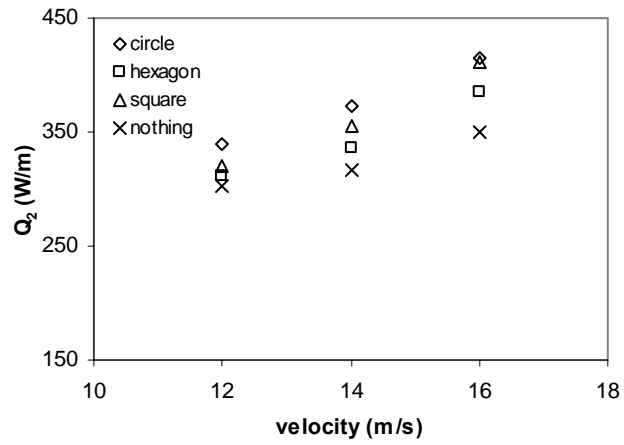
Moving on to the second part, we will see how the second heat source is affected and how the heat transfer rate behaves. By looking at figure 4.27, we can see how the plate separation distance has an effect on the heat transfer rate. It seems that the circle promoter out performs the other two promoters, but as we move the plate farther away from the vortex promoter, the higher the heat transfer rates get. When we started at a plate separation distance of  $0w$ , the values were close together, then as we moved the plate farther back, the separation in the values started to increase. Then at the final position of  $5w$ , all three promoters have higher heat transfer rates than when there is nothing there. This is because we are at the farthest place away and flow has been allowed to become chaotic, thus making the heat transfer rates higher than if there was nothing there. From looking at the comparison of  $Q_1$  and  $Q_2$ , we see that the farther away from the vortex promoter helps to increase the heat transfer rate. Next, we will be discussing how the heat transfer coefficients are affected by the promoters for both the first heat source and the second heat source.



(a)



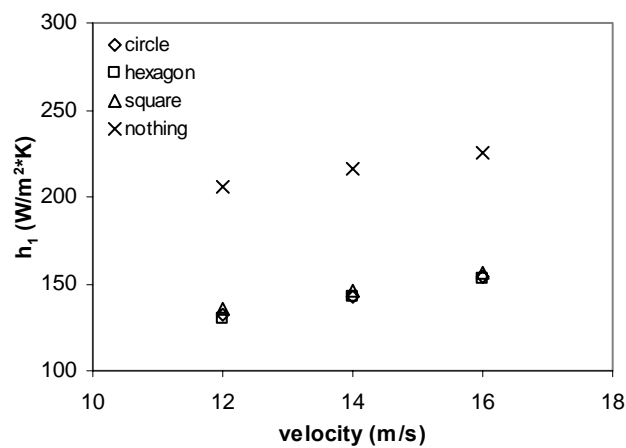
(b)



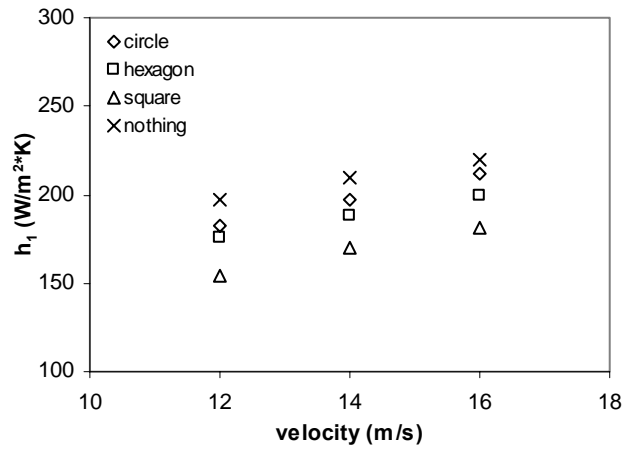
(c)

**Figure 4.27: Heat transfer rates for the second heat source for different plate separations (a)  $D/w = 0$ , (b)  $D/w = 3$ , (c)  $D/w = 5$**

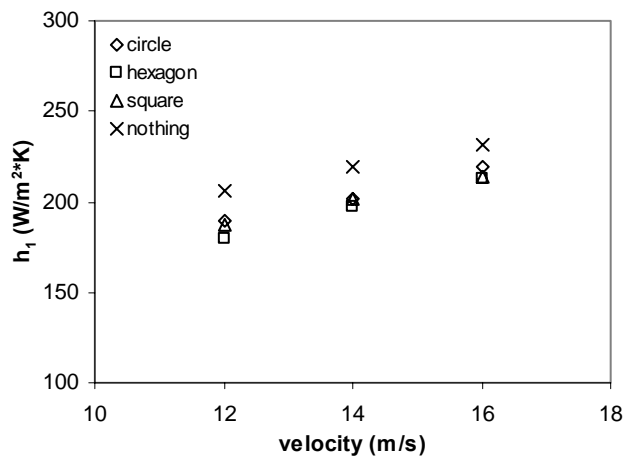
Now we will be moving on to the third and fourth part, which will concentrate on the heat transfer coefficient. In figure 4.28, the relationship between the heat transfer coefficient and velocity is shown for the first heat source. From these three graphs, when there was nothing, the heat transfer coefficients were higher than if there were promoters. This happens because the promoters are blocking the flow and prevents it from moving over the heaters. It pushes the air up and does not have the ability to come back to the heaters, thus allowing warmer air to concentrate near the heater and not be forced up into the ambient. The order of the highest values still stay the same as before, the circle promoter out performs the other two and the hexagon produces a slightly better result than the square promoter. Next we will be discussing how the heat transfer coefficient is affected by the second heat source.



(a)



(b)

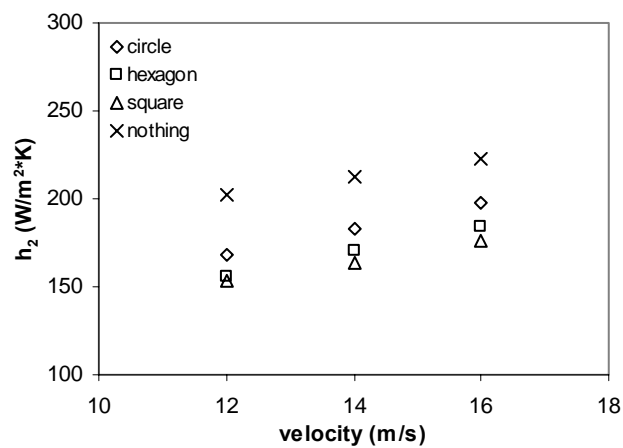


(c)

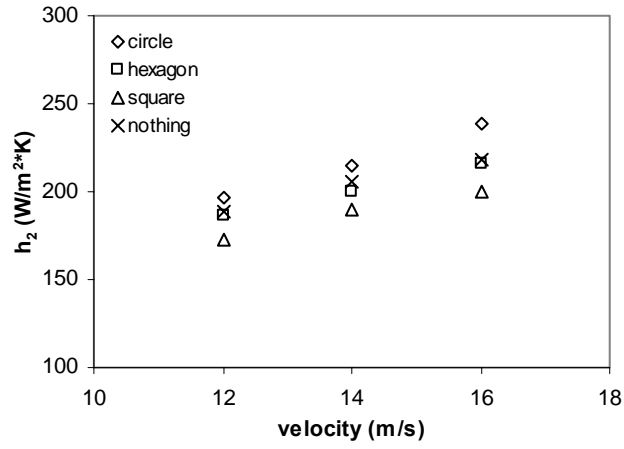
**Figure 4.28: Heat transfer coefficients for the first heat source at different separations (a)  $D/w = 0$ , (b)  $D/w = 3$ , (c)  $D/w = 5$**

From looking at figure 4.29, we can see how the second heat source does with increasing velocity in helping to promote a higher heat transfer coefficient. For these three plots we see the affects the separation distance has on the heat transfer coefficients. When the plate separation distance is  $D/w = 0$ , all the promoters cause a blocking effect,

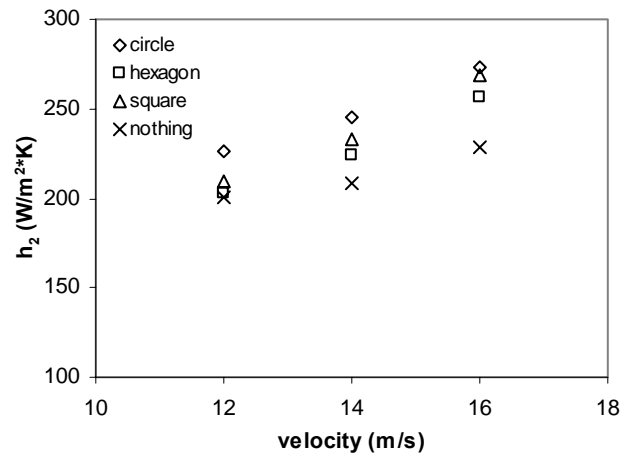
which prevents the air from touching the heat source. Then as we move the plate back away from the vortex promoter the heat transfer coefficients start to increase. At  $D/w = 3$ , the circle promoter has a 8.1% and 15.5% higher heat transfer coefficient than the hexagon and square promoters, respectively. Then once we reach the final and farthest position away from the vortex promoter we see that the heat transfer coefficient for the circle is still higher than the hexagon and square. The circle has 9.1% and 4.8% higher heat transfer coefficient than the hexagon and square. From these results, we can see that as the plate separation increases, the percentage for the circle and hexagon promoter increases, while the percentage for the circle and square promoter decreases. At the farthest away position, the heat transfer rate and the heat transfer coefficient were both at their maximum. While at the closest point to the vortex promoter,  $D/w = 0$ , the heat transfer coefficient and heat transfer rate were at a minimum.



(a)



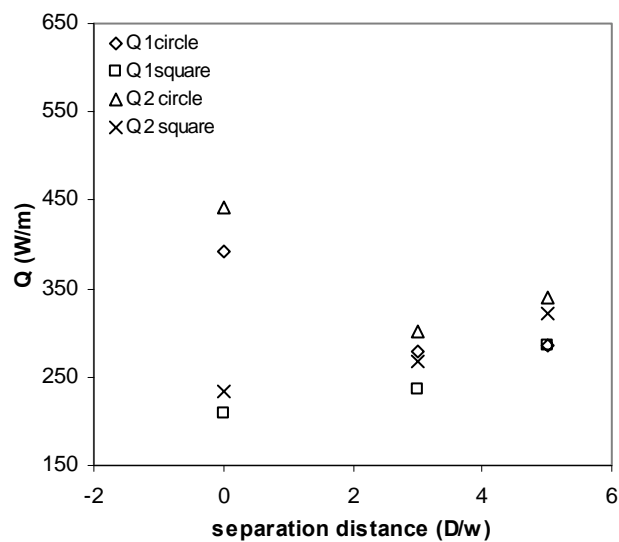
(b)



(c)

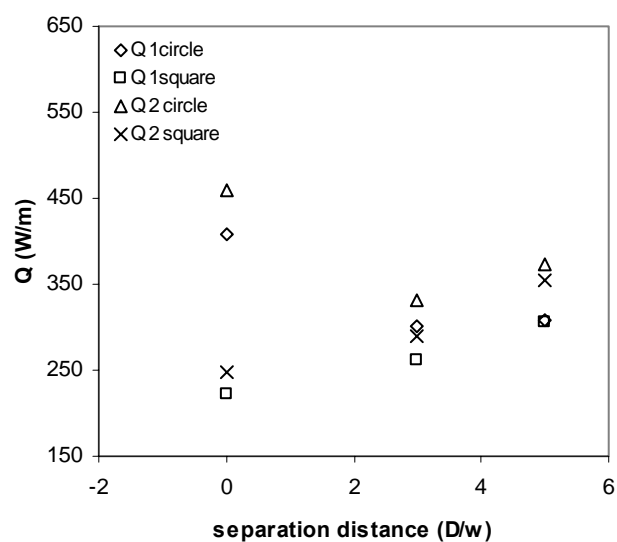
**Figure 4.29: Heat transfer coefficient for the second heat source at different separations (a)  $D/w = 0$ , (b)  $D/w = 3$ , (c)  $D/w = 5$**

From looking at the results from the previous parts, we wanted to see a comparison of the first and second heat sources on the same plot and the two better vortex promoters. The two promoters that will be used are the circle and the square. Looking at figure 4.30, we see how the heat transfer rate is changed at each plate separation distance for all 3 velocities. From the first graph, we can see that second heat source had higher values and that circle gave the better heat transfer rate out of the two promoters. The same can be said for the other two velocities, but as the velocities are increased, the heat transfer rate for the circle and the square start to become the same for the second heat source and the first heat source.

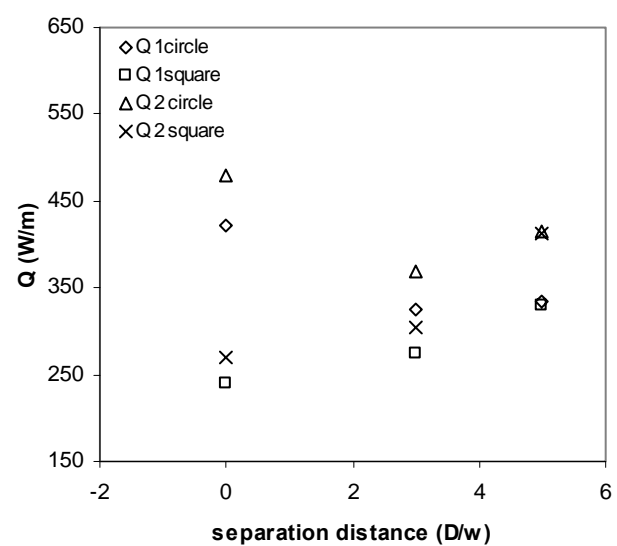


(a)





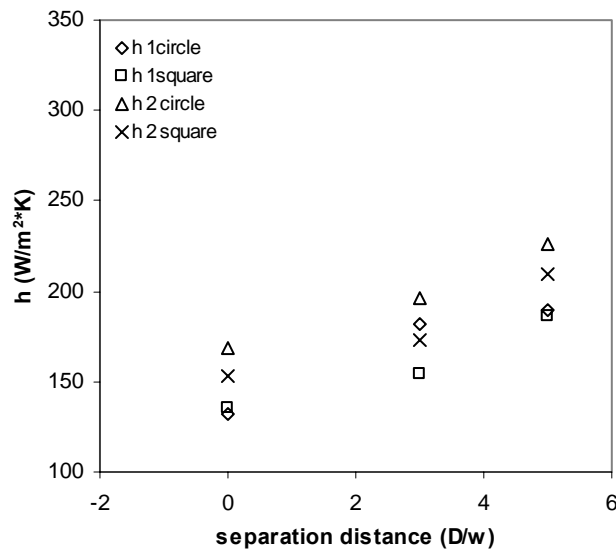
(b)



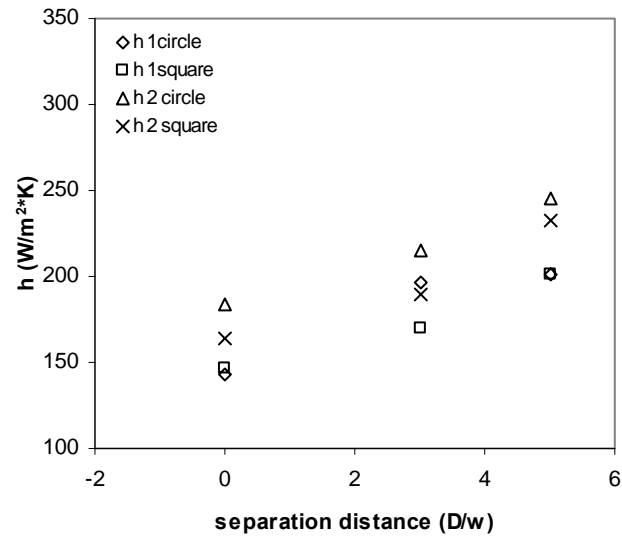
(c)

Figure 4.30:  $Q_1$  and  $Q_2$  for square and circle promoters (a) 12 m/s, (b) 14 m/s, (c) 16 m/s

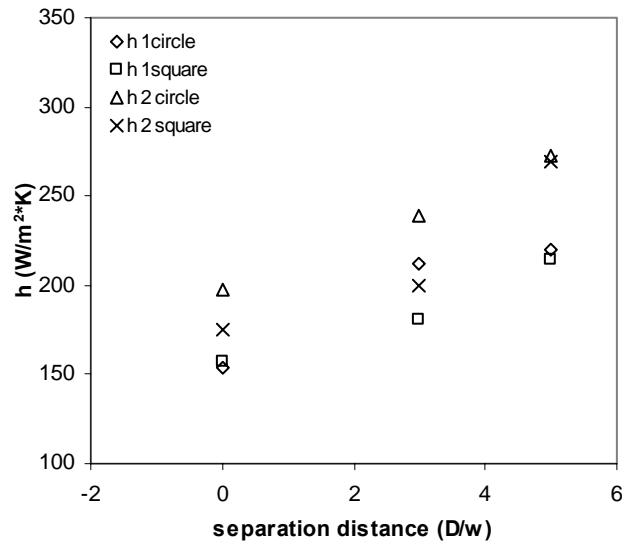
Now we will turn our attention to how the heat transfer coefficient is changed by the plate separation distance and velocities. Figure 4.31 shows the three graphs with the changing velocity and position. From these graphs we can see that there is some separation between the first and second heat sources. Then as the plate separation and velocity increases, the closer the two values for the second heat source becomes. The following could also be said for the first heat source. It seems that the values form a pattern and describe that as the farther away the plate moves and the increase in velocity, the closer the results for the circle and square promoter will be for the first and second heat sources. Next we will be showing some visualization pictures of how the flow looks when it is flowing over just the plate and when the vortex promoters are inserted.



(a)



(b)



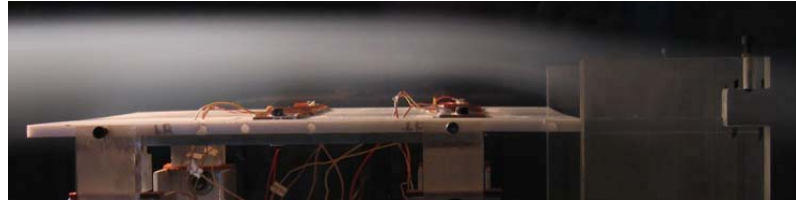
(c)

Figure 4.31:  $h_1$  and  $h_2$  for square and circle promoters (a) 12 m/s, (b) 14 m/s, (c) 16 m/s

The results have shown that if you just put a vortex promoter in the flow, it could cause more problems than if it was not there. When using the 15 mm promoter for the experiment, it caused the air to be pushed up and off the plate, thus reducing the heat transfer rate. When using the 25.4 mm promoters, it is best to keep the promoter farther away from the plate, so that the flow can become more chaotic before it hits the plate. The results have shown that when the plate was close to the vortex promoter, the heat transfer rate and coefficient were much smaller, than if no promoter was there. Then as the plate was moved farther back, the heat transfer rate and coefficient increased until they were higher than no promoter at  $D/w = 5$ . Vortex promoters are very useful if there is enough separation between itself and the plate, if not then they can cause more damage to the system because it robs the system of air flow over the electronic components.

#### **4.4 Flow Visualizations**

In this section, we will be showing some pictures that were taken while the wind tunnel was running. We used a smoke generator with fog fluid in order to see how the flow was behaving. The pictures will be started off by showing the plate only, then move on to the 15 mm promoter and then to the three 25.4 mm promoters. Shown in figure 4.32, we see the flow for the plate only. We can clearly see from the smoke, the boundary layer that is developed as the flow starts to go over the plate. The flow shown here is what we have come to expect for this situation.



**Figure 4.32: Visualization for plate flow**

In figure 4.33, the flow for the 15 mm promoter is shown. From looking at this picture we are able to see how this promoter makes the flow more chaotic. From looking at it, we can see that the flow is disturbed a little bit, but from the results, it causes more of a blocking effect instead of enhancing effect.

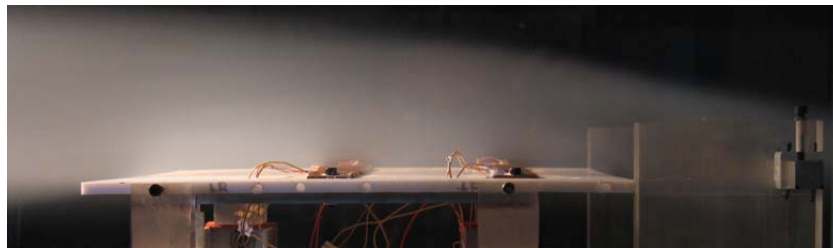


**Figure 4.33: Visualization for 15 mm promoter**

The next couple pictures that are going to be shown are the three 25.4 mm promoters. Shown in figure 4.34 is the picture of the hexagon promoter. From this picture we can see how the flow was acting around this promoter and how the flow was becoming disturbed. The flow seems to be quite disturbed and at this plate separation distance, the maximum heat transfer was reached for this promoter, however, it did not give the highest overall heat transfer rate.

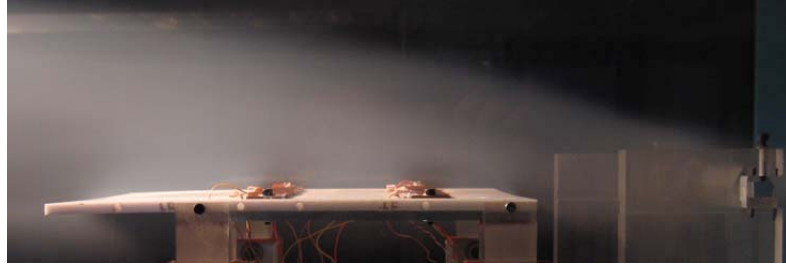


**Figure 4.34: Visualization for 25.4 mm hexagon promoter**

The next promoter that we will be discussing is the square promoter. In figure 4.35, we see how the square promoter is causing a disturbance in the flow. From the picture we can see that the disturbance from the square promoter is slightly larger wake than the hexagon promoter. This thus allowed the square promoter to have a slightly higher heat transfer rate. However the square promoter did not have the highest heat transfer rates. The next and final promoter that we will be discussing is the circle promoter.

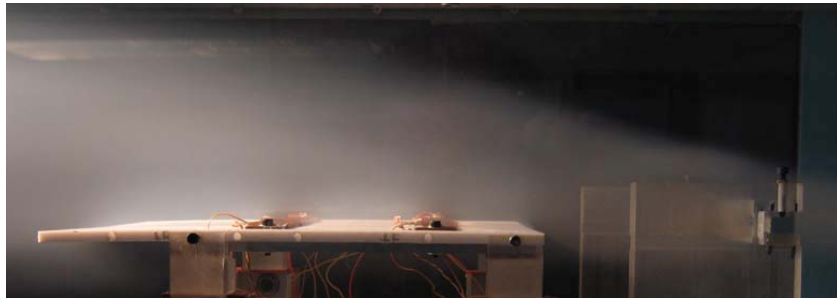


**Figure 4.35: Visualization for 25.4 mm square promoter**

The final promoter that we will be discussing is the circular promoter. Shown in figure 4.36, we see how the circular promoter is causing a disturbance in the flow. The wake behind the circular promoter seems to be not as big as the square promoter, but as look down the plate, at about half-way, the size of the wake seems to start to increase again. It almost looks like between the promoter and the middle of the plate, that region seems to

undergo the transition to turbulent and then about halfway down the plate it reaches full turbulent flow. From the results shown, the circular promoter has the highest heat transfer rate compared to the other two. This is because of the shape of the promoter. The other two promoters cause the flow to go up and over, but with the circle, it just flows around, thus allowing the flow to come back down directly onto the heat sources. In the next chapter we will present the conclusions that were present in this experimentation.

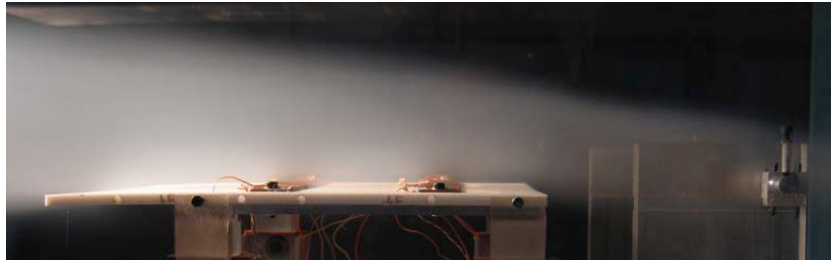


**Figure 4.36: Visualization for 25.4 mm circular promoter**

## Chapter 5

### Conclusion & Future Work

#### **5 Introduction**

In this chapter, we will be discussing the relevant conclusions that have been presented in the results section. First we will discuss the conclusions of the vortex promoter only, then move on to the plate only and finish with the combination of the vortex promoter and plate. After this, we will then be discussing the future work and what else there is to be accomplished.

#### **5.1 Conclusions**

In this section, we will be discussing the solutions that have presented themselves as the research was being conducted. The first set of conclusions that we will be discussing, are the ones based on the promoter only. For the promoter only, there were four main points that we found in the experiment.



The first point and probably the most important is that the RMS of the disturbance decreased the farther away from the promoter you are. This is important to note, because that means the promoter should be relatively close to the heaters. By doing this the heat transfer rate and coefficient will be maximized.

The second point is that out of the three vortex promoters, the hexagon and the square had a larger RMS disturbance than the circle promoter did. Even though the RMS was decreasing as the probe was moved farther away from the vortex promoter, the difference between the square and hexagon compared to the circle became larger. This could be due to the separation on the circle promoter that once full separation has occurred, the flow would not be able to become more chaotic.

The third point is that the Strouhal number, for each promoter, remained steady as the velocity increased. This happened because the frequency increased at the same rate as the velocity did. This allowed the value of the Strouhal number to remain steady throughout all the tests.

The fourth point for the promoter only is the frequency did not change with both the vertical position and horizontal position at a given velocity. By moving the hotwire horizontally across the promoter and also vertically in the center, the value of the frequency did not change. This allows us to assume that the frequency behind the promoter at a certain velocity will be the same for any place behind the promoter.

There was only one major point for the plate only that presented itself during the results and analysis and repeated throughout. That point is, that the farther away the second heat source is away from the first heat source, the better the heat transfer rate became. For a separation of  $d/w = 4$  from the first heat source, the second heat source

was able to operate without any effects from the first heat source. At that point, the heat from the first heat source had been moved to the ambient and away from the second heat source, thus allowing the cold air to be placed on top of the second heat source. This result however is not practical because at that point they act as two totally different entities, which have no effect on each other.

In this part, we will be discussing the major points that were discovered from the results section. The first point we have found is that the 15 mm promoter caused more of a blocking effect instead of enhancing the flow. This promoter caused the flow to go around itself, but did not help the heaters. It allowed the heaters to not heat up as much as they would if there was nothing there. This caused the promoter to have a limit of 10.3% lower heat transfer rate than if nothing was there. This proves that the 15 mm promoter caused more harm than helping to enhance the flow.

The second point we came across during the experiments was that for the large promoter caused the heat transfer rate for the first heat source to be small, but allowed the heat transfer rate for the second heat source to much larger. These effects were seen in the results especially for the plate separation distances. The highest heat transfer rates occurred for the circle promoter at a plate separation distance of  $D/w = 5$ . The circle promoter was generating around 16.2% more heat that was transfer into the air, as compared to nothing obstructing the flow. At this plate separation distance, all three promoters were giving results that were higher than when nothing was there, but not as much as the circle promoter was exhausting into the free stream. This shows that as the plate moves farther away from the vortex promoter, the better the heat transfer rate gets.

## 5.2 Future Work

This was experimental work in air cooling using protruding heat sources to see what effect the different size and shapes of vortex promoters could have on the flow. By using these promoters we were able to see the effects and the enhancements they have done for the heat transfer rate. Air cooling for electronic devices is approaching the upper limit in its effectiveness, but there are still a few things that can be done.

One point would be to change the orientation of the promoter. Allowing the promoter to be changed from horizontal to vertical positions or left at a certain angle in between. This could grant some unexpected results that would normally be left behind or not thought of.

A second point would be to use other geometries for the vortex promoter. This experiment only picked up 4 different size shapes. Future experiments could look into how more advanced shapes can enhance the heat transfer rate and coefficient.

The third point is causing the vortex promoter to vibrate. By causing vibrations in the promoter, new types of oscillations would be occurring because not only is it making the flow chaotic in one direction, but also in the direction of the vibration. This could cause the heat transfer rate and coefficient to be higher. The frequency of the vibration could either be adjusted or set at a point to see how the vibration frequency affects the flow.

The fourth point is to try having heat sources mounted on both the top and bottom of the plate. This would help us to see how the heat transfer rate could be increased. The fact that they are mounted close together might cause the heat transfer rate to decrease instead of increasing, depending on what the separation height is between the two plates.

## Chapter 6

### Appendix

#### **6 Introduction**

In this appendix, calibration data of the equipment is presented, along with some extra results. These extra results are included here because it would have disturbed the flow and process of things. First we will be presenting the calibration data that was used in the experiments. Then the next part is where the extra results will be presented.

##### **6.1 Calibration Data**

Figure 6.1 shows the calibration of the wind tunnel. It shows the blower speed, which is controlled in the Labview program and the instantaneous velocity sensed by the Pitot tube and the velocity measured by the Ascroft control panel. The graph shows a good relation between the blower speed and the instantaneous velocity and Ascroft velocity, except below 7 m/s. This, in part, is due to the large test section and the fact the fan is constantly turning on and off to keep it at a low speed.

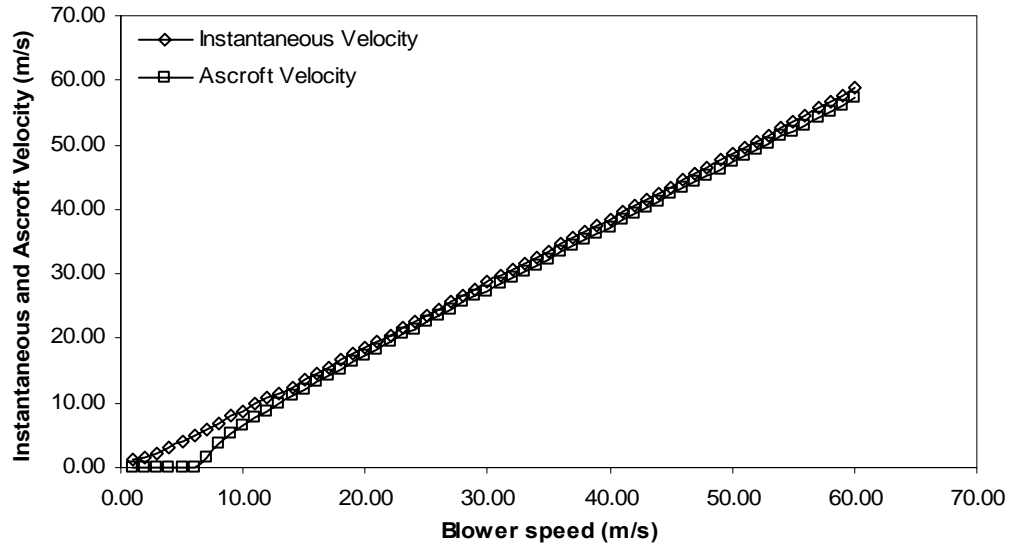


**Figure 6.1: Wind Tunnel Calibration between blower speed and Instantaneous and Control Velocity**

Figure 6.2 shows the calibration of the thermocouples. The thermocouples were made by using the Hot-Spot Welder and then calibrated at 5 different temperatures. The differences between the different thermocouples were found to be quite small, so only one calibration curve is displayed. The same data is applicable to all the thermocouples used in this experiment.

The hot-wire probe output is also calibrated as a function of air velocity as shown in figure 6.3 at two different temperatures. The two hot-wire probes that were used in all experiments are shown. From the two plots we can see that the change in temperature had little effect on the calibration curves.

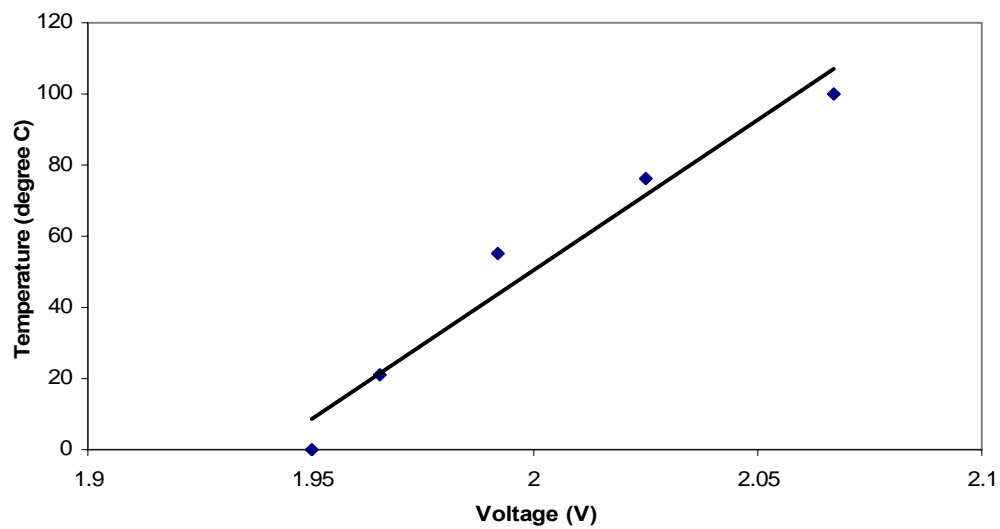


Figure 6.2: Thermocouple calibration

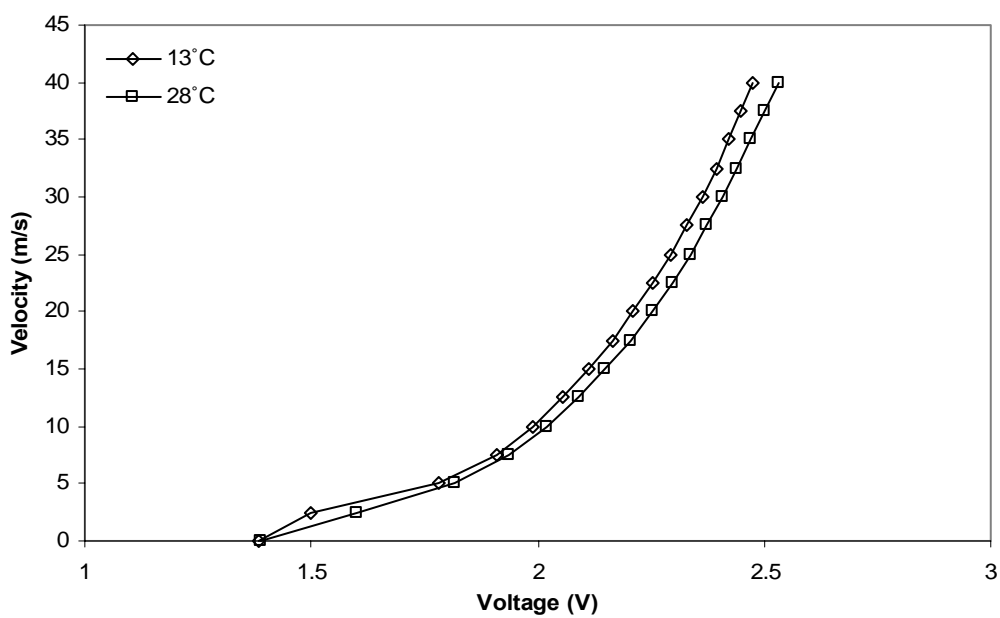
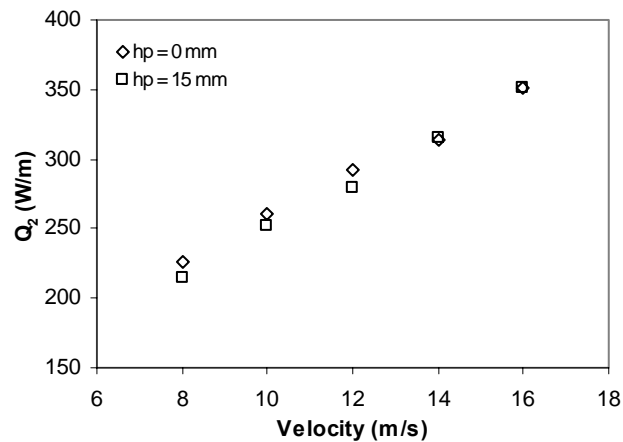


Figure 6.3: Hotwire calibration

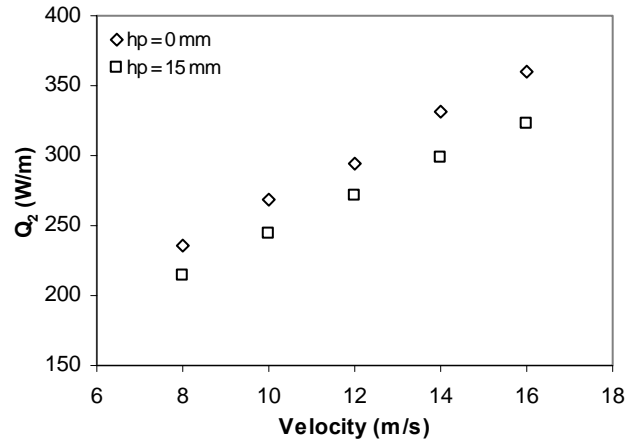
## 6.2 Additional Results

In this section, we will present the additional results that were not presented in chapter 4. The results presented here discuss the effect the 15 mm promoter had on separation widths of  $3w$  and  $4w$ . This part will be broken down into 3 different parts. The first part will be describing the effects  $Q_2$  felt at a separation width of  $3w$  and  $4w$ . Then in the second part, we will show the effects  $h_2$  felt at a separation width of  $3w$  and  $4w$ . Then finally we will describe the effects of  $Nu_2$  at a separation width of  $3w$  and  $4w$ .

In figure 6.4, the results of  $Q_2$  are shown. From looking at the plots, we can see that the 15 mm promoter was causing a blocking effect, because the heat transfer values were slightly smaller for a separation width of  $3w$ , but for the separation width of  $4w$ , the values were not close at all. When there was nothing there, the heat transfer rates were higher than if the promoter was there.



(a)

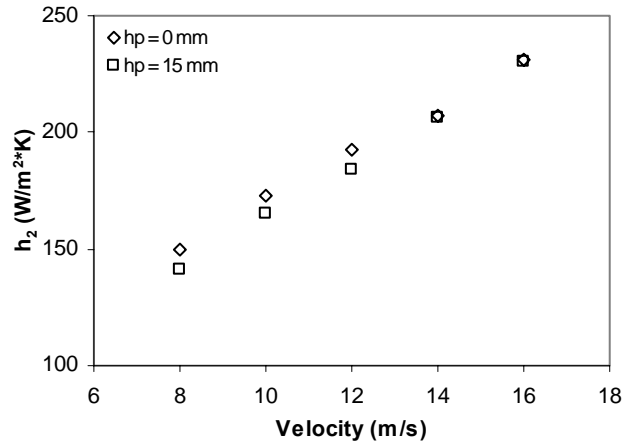


(b)

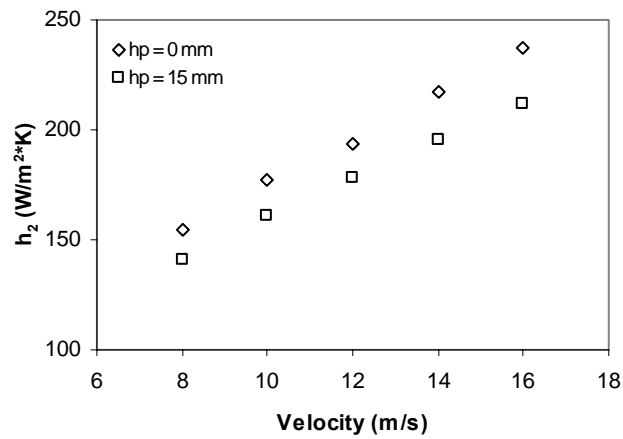
**Figure 6.4:  $Q_2$  for 15 mm promoter at separation widths (a)  $d/w = 3$ , (b)  $d/w = 4$**

In the second part, we will be describing the effects that the promoter had on the heat transfer coefficient,  $h_2$ . Shown in figure 6.5, we see how the promoter help to reduce the heat transfer coefficient as compared to when there was nothing in the flow. There is one exception to this though, for the separation width of  $3w$  at 14 and 16 m/s, the promoter had the same heat transfer coefficient as when there was nothing there. So for these two points, the heat transfer coefficient was close but was not higher than it. So the promoter still caused a slight blocking effect because it was not enhancing the flow at that point. It just allowed the flow to go back to how it was before. Then when the separation width was increased to  $4w$ , the promoter definitely caused the heat transfer coefficient to be hindered or reduced.





(a)



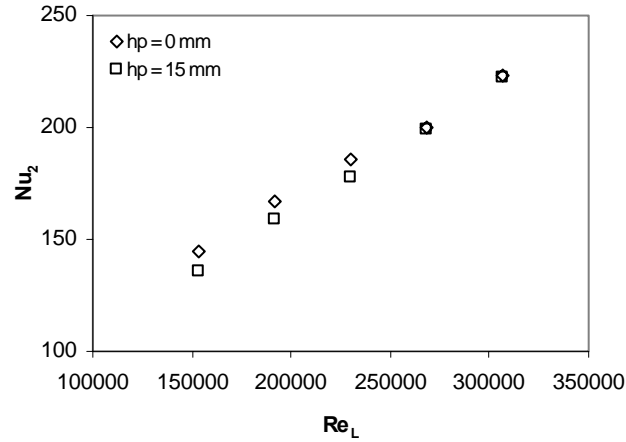
(b)

**Figure 6.5:  $h_2$  for 15 mm promoter at separation widths (a)  $d/w = 3$ , (b)  $d/w = 4$**

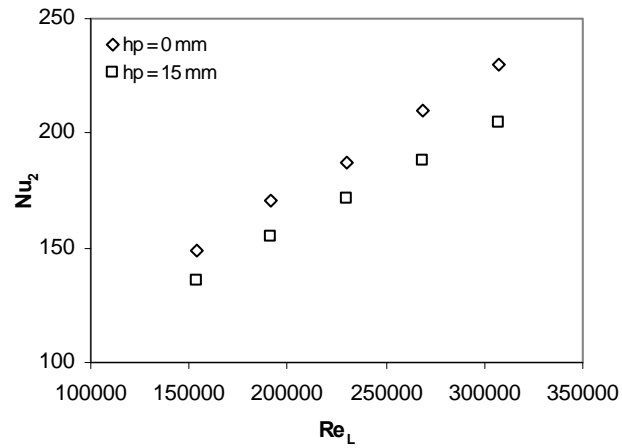
Then in the final part, we will be discussing the effects the promoter had on the Nusselt number for the second heat source. In figure 6.6, the effects of the Nusselt number are shown for the different separation widths of  $3w$  and  $4w$ . From these plots, we see that the Nusselt number is just slightly less than the heat transfer coefficient. This is what we would expect, because the Nusselt number is based on the heat transfer

coefficient. The graphs are basically the same as the heat transfer coefficient expect that the magnitudes of the results are slightly smaller than the heat transfer coefficient values.

The patterns however are still the same.



(a)



(b)

Figure 6.6:  $Nu_2$  for the 15 mm promoter at separation widths (a)  $d/w = 3$ , (b)  $d/w = 4$

## References

- [1] DeLorenzo, D., Opdahl, J., "Server Design Challenges for the High-Heat-Load Internet Data Center." *Electronics Cooling*. Vol. 11, issue 1, pg 12-18. 2005.
- [2] Chu, R.C., "Heat Transfer in Electronic Systems." *Proceedings of the 8<sup>th</sup> International Heat Transfer Conference*. Vol. 1 pg. 293-305. 1986.
- [3] Schmidt, R. "Liquid Cooling is Back." *Electronics Cooling*. Vol. 11, issue 3, pg. 34-38. 2005.
- [4] Sathe, S., Sammakia, B., "A Review of Recent Developments in Some Practical Aspects of Air-Cooled Electronic Packages." *Journal of Heat Transfer*. Vol. 120 pg. 830-839. 1998.
- [5] Incropera, F.P., "Convection Heat Transfer in Electronic Equipment Cooling." *Journal of Heat Transfer*. Vol. 110 pg. 1097-1111. 1988.
- [6] Icoz, T., Verma, N., Jaluria, Y., "Design of Air and Liquid Cooling Systems for Electronic Components Using Concurrent Simulation and Experiment." *Proceedings of the Heat Transfer/Fluids Engineering Summer Conference*. Vol. 4 pg. 565-574. 2004.
- [7] Behnia, M., Nakayama, W., "Numerical Simulation of Combined Natural Convection-Conduction Cooling of Multiple Protruding Chips on a Series of Parallel Substrates." *InterSociety Conference on Thermal Phenomena*. pg. 135-142. 1998.
- [8] Ortega, A., Lall, B., "Natural Convection Air Cooling of a Discrete Source on a Conducting Board in a Shallow Horizontal Enclosure." *12<sup>th</sup> Semiconductor Thermal Measurement and Management Symposium* pg. 201-213. 1996.
- [9] Rodgers, P., Eveloy, V., Lohan, J., Fager, C., Tiilikka, P., Rantala, J., "Experimental Validation of Numerical Heat Transfer Predictions for Single- and Multi-Component Printed Circuit Boards in Natural Convection Environments." *15<sup>th</sup> Semiconductor Thermal Measurement and Management Symposium*. pg 54-64. 1999.
- [10] Sarvar, F., Witting, P.A., Poole, N.J., "Examination of Natural Convection Plumes from Partially Heated PCB Plates and Estimation of the Heat Transfer Coefficients." *Journal of Electronic Materials*. Vol. 22, issue 5, pg. 573-577. 1993.

- [11] Bar-Cohen, A., "Bounding Relations for Natural Convection Heat Transfer from Vertical Printed Circuit Boards." Proceedings of the IEEE. Vol. 73, issue 9, pg. 1338-1395. 1985.
- [12] Rodgers, P., Lohan, J., Eveloy, V., Fager, C., Rantala, J., "Validating Numerical Predictions of Component Thermal Interaction on Electronic Printed Circuit Boards in Forced Convection Air Flows by Experimental Analysis." ASME, EEP. Vol. 26 pg. 999-1008. 1999.
- [13] Cole, R., Dalton, T., Punch, J., Davies, M., Grimes, R., "Forced Convection Board Level Thermal Design Methodology for Electronic Systems." Journal of Electronic Packaging. Vol. 123 pg. 120-126. 2001.
- [14] Nakamura, H., Igarashi, T., "Forced Convection Heat Transfer from a Low-Profile Block Simulating a Package of Electronic Equipment." Journal of Heat Transfer. Vol. 126 pg. 463-470. 2004.
- [15] Wang, Q., Jaluria, Y., "Three-Dimensional Conjugate Heat Transfer in a Horizontal Channel with Discrete Heating." Journal of Heat Transfer. Vol. 126 pg. 642-647. 2004.
- [16] Icoz, T., Jaluria, Y., "Design of Cooling Systems for Electronic Equipment Using Both Experimental and Numerical Inputs." Journal of Electronic Packaging. Vol. 126 pg. 465-471. 2004.
- [17] Roeller, P.T., Stevens, J., Webb, B.W., "Heat Transfer and Turbulent Flow Characteristics of Isolated Three-Dimensional Protrusions in Channels." Journal of Heat Transfer. Vol. 113 pg. 597-603. 1991.
- [18] Davalath, J., Bayazitoglu, Y., "Forced Convection Cooling Across Rectangular Blocks." Journal of Heat Transfer. Vol. 109 pg. 321-328. 1987.
- [19] Icoz, T., Jaluria, Y., "Optimization of Vortex Promoter Design using a Dynamic Data Driven Approach." Proceedings of the ASME Summer Heat Transfer Conference. Vol. 4 pg. 607-617. 2005.
- [20] Gupta, A., Jaluria, Y., "Forced Convective Liquid Cooling of Arrays of Protruding Heated Elements Mounted in a Rectangular Duct." Journal of Electronic Packaging. Vol. 120 pg. 243-252. 1998.
- [21] Incropera, F.P., *Liquid Cooling of Electronic Devices by Single-Phase Convection*. New York: John Wiley & Sons, Inc. 1999.
- [22] Wikipedia. 24 May 2006. Wikipedia Foundation, Inc. 25 May 2006. [http://en.wikipedia.org/wiki/Heat\\_Pipe](http://en.wikipedia.org/wiki/Heat_Pipe).

- [23] Aerolab Subsonic Wind Tunnel User Manual
- [24] Scanivalve Corporation Digital Sensor Array Module 3017 User Manual
- [25] National Instruments. July 2006. National Instruments Incorporated. 8 September 2006. <http://www.ni.com/>
- [26] Omega Engineering. July 2006. Omega Engineering Incorporated. 8 September 2006. <http://www.omega.com/>
- [27] Dantec Dynamics Streamline Constant Temperature Anemometer System Manual
- [28] Dantec Dynamics. 11 July 2006. Dantec Dynamics A/S. 9 September 2006. <http://www.dantecdynamics.com/CTA/System/Index.html>
- [29] Lo, S.-C., Hoffmann, K.A., Dietiker, J.-F., Numerical Investigation of High Reynolds Number Flows over Square and Circular Cylinders. *Journal of Thermophysics and Heat Transfer*. Vol. 19. No. 1. pg. 72-80. 2005
- [30] Davis, R.W., Moore, E.F., A Numerical Study of Vortex Shedding from Rectangles. *Journal of Fluid Mechanics*. Vol. 116. pg. 475-506. 1982.
- [31] Okajima, A., Ueno, H., Sakai, H., Numerical Simulation of Laminar and Turbulent Flows around Rectangular Cylinders. *International Journal for Numerical Methods in Fluids*. Vol. 15. pg 999-1012. 1992.
- [32] Saha, A.K., Muralidhar, K., Biswas, G., Investigation of Two- and Three-Dimensional Models of Transitional Flow Past a Square Cylinder. *Journal of Engineering Mechanics*. Vol. 129. No. 11. pg. 1320-1329. 2003.
- [33] Kelkar, K.M., Patankar, S.V., Numerical Prediction of Vortex Shedding Behind a Square Cylinder. *International Journal for Numerical Methods in Fluids*. Vol. 14. pg. 327-341. 1992.
- [34] Igarashi, T., Fluid Flow and Heat Transfer Around Rectangular Cylinders (The Case of a Width / Height Ratio of a Section of 0.33 ~ 1.5). *International Journal of Heat and Mass Transfer*. Vol. 30. No. 5. pg. 893-901. 1987.
- [35] Teertstra, P., Urbanski, J.P., Culham, J.R., Conjugate Heat Transfer Measurements for Air-Cooled Electronics – A New Experimental Method. *Annual IEEE Semiconductor Thermal Measurement and Management Symposium*. pg. 195-201. 2003.
- [36] Launder, B.E., Kato, M., Modelling Flow-Induced Oscillations in Turbulent Flow Around a Square Cylinder. *ASME-Unsteady Flows*. Vol. 157. pg. 189-199. 1993.

- [37] Nomura, T., Suzuki, Y., Uemura, M., Kobayashi, N., Aerodynamic Forces on a Square Cylinder in Oscillating Flow with Mean Velocity. *Journal of Wind Engineering and Industrial Aerodynamics*. Vol. 91. pg. 199-208. 2003.
- [38] Nakamura, Y., Ohya, Y., The Effects of Turbulence on the Mean Flow Past Two-Dimensional Rectangular Cylinders. *Journal of Fluid Mechanics*. Vol. 149. pg. 255-273. 1984.
- [39] Saha, A.K., Muralidhar, K., Biswas, G., Transition and Chaos in Two-Dimensional Flow Past a Square Cylinder. *Journal of Engineering Mechanics*. Vol. 126. No. 5. pg. 523-532. 2000.
- [40] Noda, H., Nakayama, A., Reproducibility of Flow Past Two-Dimensional Rectangular Cylinders in a Homogeneous Turbulent Flow by LES. *Journal of Wind Engineering and Industrial Aerodynamics*. Vol. 91. pg. 265-278. 2003.
- [41] Saha, A.K., Muralidhar, K., Biswas, G., Experimental Study of Flow Past a Square Cylinder at High Reynolds Numbers. *Experiments in Fluids*. Vol. 29. pg. 553-563. 2000.
- [42] Okajima, A., Numerical Simulation of Flow around Rectangular Cylinders. *Journal of Wind Engineering and Industrial Aerodynamics*. Vol. 33. pg. 171-180. 1990.
- [43] Huot, J.P., Rey, C., Arbey, H., Experimental Analysis of the Pressure Field Induced on a Square Cylinder by a Turbulent Flow. *Journal of Fluid Mechanics*. Vol. 162. pg. 283-298. 1986.
- [44] Okajima, A., Strouhal Numbers of Rectangular Cylinders. *Journal of Fluid Mechanics*. Vol. 123. pg. 379-398. 1982.
- [45] Figliola, R. S., Beasley, D.E., Theory and Design for Mechanical Measurements. 4<sup>th</sup> Edition. New York: John Wiley & Sons, Inc. 2006
- [46] N. Udovidchik, 2002. Correction Factor Report. Rutgers University, New Brunswick, NJ.
- [47] Fox, Robert W., McDonald, Alan T., Introduction to Fluid Mechanics. 5<sup>th</sup> Edition. New York: John Wiley & Sons, Inc. 1998